

UNIVERSITY OF CALIFORNIA  
RIVERSIDE

Measurement of Charged Particle Multiplicity with the Multiplicity  
and Vertex Detector at the PHENIX Experiment at RHIC

A Thesis submitted in partial satisfaction  
of the requirements for the degree of

Master of Science

in

Physics

by

Tahsina Ferdousi

November 2002

Thesis Committee:

Professor Richard Seto, Chairperson

Professor Kenneth Barish

Professor Allen Zych

The Thesis of Tahsina Ferdousi is approved:

Allen Zych

Kunira Dall

Richard H. Nichols

Committee Chairperson

University of California Riverside

Copyright by  
Tahsina Ferdousi  
2002

To my parents

## ACKNOWLEDGMENTS

I feel honored to acknowledge wholeheartedly with deepest sense of gratitude, the able supervision, dynamic guidance, invaluable suggestions from my esteemed adviser Professor Richard Seto. In fact I have incurred more debts in completing this research work than I can hope to acknowledge. I am grateful to him for giving me the opportunity to work closely with him. Working with him has been one of the most delightful experiences in my research work. Dating long time back, in August of 2000 when we started analysis people thought that we can not do anything with the data from MVD due to severe limitation of electronics. But only exception was my adviser Richard Seto, who never gave up and that was the inspiration for me to continue the MVD analysis. Now this analysis is a true PHENIX story which emerged from ashes. I owe him an enormous debt of gratitude.

I must thank all the members of our Heavy Ion Physics Research group at UCR. In particular I would like to thank Professor Ken Barish for his valuable suggestions during the course of analysis. I am thankful to Dr. Basanta Nandi who helped me time to time on various software related questions. I also thank Dr. Xin-Hua Li, Dr. Haiqiao Wang and Dr. Xie Wei for their interest in my research. I must also recognize my fellow graduate students M. Muniruzzaman and Dmitri Kotchetkov with whom I had lively discussions on many occasions.

I am also thankful to my teachers here at the physics department for their help and cooperation during my graduate study.

I also must thank the rest of the phenix collaboration whose tireless works made the analysis possible. I specially thank all of the MVD folks. Their valuable suggestions helps me to do online monitoring.

I am grateful to my husband Munir for his support since the beginning of my graduate career. Thank you Munir.

I would like to thank to my Parents and my only brother for their love and patience. Although they are in Bangladesh, but they were always a source of encouragements that they never let me feel that I am away from them.

## ABSTRACT OF THE THESIS

Measurement of Charged Particle Multiplicity with the Multiplicity and Vertex  
Detector at the PHENIX Experiment at RHIC

by

Tahsina Ferdousi

Master of Science, Graduate Program in Physics

University of California Riverside, November 2002

Professor Richard Seto, Chairperson

The charged particle multiplicity is measured with the Multiplicity and Vertex Detector at the PHENIX experiment at RHIC. The heavy ion collisions at RHIC energies are expected to produce a new phase of matter called the quark-gluon plasma. There are many proposed signatures for the formation of the quark-gluon plasma. The potential signatures are investigated as a function of the energy density  $\epsilon$  or a quantity closely related to the energy density, such as the rapidity density of the transverse energy  $dE_T/dy$  or the pseudorapidity density of the charged particle multiplicity  $dN/d\eta$ . The measurement of the charged particle multiplicity enables us to measure the energy density of formation. The energy density is measured to be 4.97 GeV/fm<sup>3</sup>.

The charged particle multiplicity measured in the MVD is compared with the measurements made in the PHENIX Pad Chambers and PHENIX Electromagnetic Calorimeters. The centrality dependence of the pseudorapidity density of the charged particles multiplicity is compared with the data from the PHOBOS experiment at RHIC. Also, the measurements were compared with the HIJING model and the High Density QCD saturation model. The saturation model is better suited to describe the data.

# Contents

<b>1</b>	<b>Introduction</b>	<b>1</b>
1.1	Quarks and Gluons: Basic Building Blocks of Normal Nuclear Matter	1
1.2	Quarks and Gluons: An Elaborative View . . . . .	3
1.3	The Color Force . . . . .	4
1.4	Quark Gluon Plasma . . . . .	6
1.5	Signature of Quark-Gluon Plasma: Theoretical Guidance . . . . .	9
1.5.1	Lattice Gauge Theory . . . . .	9
1.5.2	Parton Cascade Model . . . . .	10
1.5.3	Hadronic Transport Models . . . . .	10
1.6	Why Heavy Ion Collisions . . . . .	11
1.7	Experimental Signatures . . . . .	12
1.8	Experiments . . . . .	17
1.8.1	Experimental Conditions . . . . .	17
1.8.2	Present Relativistic Heavy Ion Accelerators . . . . .	17
1.8.3	Heavy Ion Colliders . . . . .	18
1.9	Summary . . . . .	19
1.10	Organization of the Thesis . . . . .	19
<b>2</b>	<b>Kinematics</b>	<b>21</b>
2.1	Relativistic Kinematics . . . . .	21
2.1.1	Conventions & Notations . . . . .	21

2.1.2	Rapidity Variable . . . . .	23
2.1.3	Pseudorapidity Variable . . . . .	24
<b>3</b>	<b>Overview of PHENIX</b>	<b>26</b>
3.1	Introduction . . . . .	26
3.2	The Relativistic Heavy Ion Collider . . . . .	27
3.3	PHENIX Experiment at RHIC . . . . .	30
3.4	A Brief Description of the Detector Components . . . . .	31
3.5	Inner Detectors . . . . .	34
3.5.1	Beam Beam Counter (BBC) . . . . .	34
3.5.2	Multiplicity & Vertex Detector (MVD) . . . . .	36
3.6	Zero Degree Calorimeter . . . . .	37
3.7	Central Arm Detectors . . . . .	38
3.7.1	Central Magnet . . . . .	40
3.7.2	Tracking and Momentum Measurements . . . . .	41
3.7.3	Particle Identification . . . . .	44
3.8	Muon Spectrometers . . . . .	47
3.9	Subsystems Used For This Analysis . . . . .	47
<b>4</b>	<b>MVD Overview</b>	<b>49</b>
4.1	Introduction . . . . .	49
4.2	Overview of Silicon Detector . . . . .	50
4.3	MVD Construction . . . . .	53
4.4	MVD Support Structure . . . . .	57
4.5	Electronics . . . . .	59
4.6	Charged Particle Multiplicity . . . . .	63
4.7	A Few Words on Year-1 Configuration . . . . .	65
4.8	MVD Online Monitoring . . . . .	65

4.8.1	What Do We Want to Achieve? . . . . .	66
4.8.2	MVD Online Monitoring Software . . . . .	67
4.8.3	Single Strip Monitoring . . . . .	71
4.8.4	MCM Mean and RMS ADC Monitoring . . . . .	71
4.9	Conclusion . . . . .	74
<b>5</b>	<b>Charged Particle Multiplicity Measurement in MVD</b>	<b>75</b>
5.1	Physics Goals of MVD . . . . .	75
5.2	Simulation . . . . .	76
5.2.1	Variables . . . . .	77
5.2.2	Charge Deposition in Si by a Track . . . . .	79
5.3	Real data : Run Condition and Vertex . . . . .	83
5.4	Centrality Selection . . . . .	87
5.5	Number of Participants . . . . .	91
5.6	Raw ADC Distribution . . . . .	92
5.7	AMU Cell Dependence of Pedestal . . . . .	93
5.7.1	AMU Operation . . . . .	94
5.8	ADC Fluctuation Correction Procedure . . . . .	97
5.9	Event-by-event Pedestal Jumping . . . . .	99
5.9.1	Event-by-event Correction . . . . .	101
5.10	Event-by-event Correction Procedure : Simulation . . . . .	103
5.11	Fitting of the Data . . . . .	106
5.11.1	Thick Detectors . . . . .	107
5.11.2	Thin Detectors . . . . .	108
5.11.3	Very Thin Detectors . . . . .	109
5.11.4	Is MVD a Thin or Very-Thin Detector? . . . . .	109
5.11.5	Energy Loss Distribution in MVD . . . . .	110
5.11.6	Fitting Example . . . . .	113

5.12	Strategy to Calculate $dN/d\eta$ . . . . .	114
5.13	Length Correction and Multiple Counting of Tracks Correction . . . . .	118
5.14	$dN/d\eta$ in MVD . . . . .	121
5.15	Acceptance Correction and Results . . . . .	122
5.16	Systematic Errors . . . . .	125
5.17	Results . . . . .	126
5.18	Conclusion . . . . .	135
<b>6</b>	<b>Model Comparison</b>	<b>136</b>
6.1	Introduction . . . . .	136
6.2	Energy Density . . . . .	136
6.3	Soft + Hard Process . . . . .	139
6.4	High Density QCD and Hadron Production . . . . .	141
6.5	Energy Density using the Saturation Model . . . . .	143
6.6	Centrality Dependence . . . . .	143
6.6.1	Converting Gluons into Hadrons . . . . .	146
6.7	Conclusion . . . . .	152
<b>A</b>	<b>Ntuple Production from PRDF</b>	<b>158</b>

# List of Figures

1.1	Structure of atoms and the size of its constituents with respect to the size of the atom . . . . .	2
1.2	In QED, virtual electron-positron pairs from the vacuum screen the bare charge of the electron. The larger the distance, the more pairs are present to screen the bare charge and the electromagnetic coupling decreases. Conversely, the coupling is larger when probed at short distances. . . . .	6
1.3	Stefan-Boltzmann law for nuclear matter . . . . .	7
1.4	Phase Diagram for Nuclear Matter . . . . .	8
1.5	Signature of Quark-Gluon Plasma. The potential signatures are shown as a function of the pseudorapidity density of the transverse energy $dE_T/d\eta$ . The new phase of matter is expected above the critical energy density $\epsilon_c$ . . . . .	16
2.1	Coordinate System . . . . .	22
3.1	Gold-Gold Collision at RHIC . . . . .	26
3.2	The RHIC Complex . . . . .	28
3.3	RHIC Beam Interaction Points. The Locations of the four experiments are shown. . . . .	29
3.4	Schematic of the PHENIX Experiment at RHIC . . . . .	31
3.5	PHENIX View from Beam line. . . . .	32

3.6	PHENIX Side View . . . . .	33
3.7	Front view of the beam-beam counter array. . . . .	36
3.8	BBC Zero Time and Z-vertex Measurement . . . . .	37
3.9	Beam line geometry around the interaction regions showing the beam splitting dipoles and the zdc detector placement. . . . .	38
3.10	PHENIX Central Magnet Field Lines . . . . .	40
3.11	Particle track in the Drift Chambers and the Hough transform parameters : azimuthal angle $\phi$ and the inclination angle $\alpha$ . . . . .	42
3.12	Particle Identification in PHENIX Time-of-flight. The data used is from year-1 at $\sqrt{s} = 130$ GeV. Clear bands of particles are seen, which is an evidence of the excellent PID capability . . . . .	46
4.1	Silicon Detector : Working Principle . . . . .	51
4.2	An Schematic view of the MVD . . . . .	54
4.3	A Photograph of the MVD after some of the silicon strips were installed	55
4.4	Schematic of the MVD barrel. The barrels are concentric, with radii 5cm and 7.5 cm respectively. Data from the blue strips were used in this analysis . . . . .	55
4.5	Schematic of the MVD End Caps. . . . .	56
4.6	Photograph of C-cage . . . . .	58
4.7	MVD Electronics Chain . . . . .	61
4.8	Block Diagram of the MVD electronics chain for 1 Strip Detector (256 Strips . . . . .	62
4.9	Block Diagram of the MVD electronics chain for 1 Strip . . . . .	62
4.10	MVD Year-1 Configuration . . . . .	64
4.11	Simplified PHENIX Data Collection Chain . . . . .	66

4.12	MVD Online Monitoring : MVD Online Monitoring GUI. Here the user selects whether to monitor the global status of the detector or to monitor a single MCM . . . . .	68
4.13	MVD Online Monitoring : File Selection Window. Here the user selects the file to read the data from. Here the user has option to select a file from a saved file or use the data in real time from DD-pool . . . . .	69
4.14	MVD Online Monitoring : Global Monitoring. Top plot is the channel number in X-axis vs the corresponding ADC value in Y-axis. The middle plot is the 1-D histogram of the ADC from all channels. The bottom plot is the number of channels that falls in a certain range of ADC. See text for explanation . . . . .	70
4.15	MVD Online Monitoring : Single Strip Monitoring. Shown 16 plots for the 1-D ADC distribution for 16 MCMs. . . . .	72
4.16	MVD Online Monitoring : Strip Mean & RMS Monitoring. Top plot is MCM number in X-axis vs the corresponding mean ADC. The bottom plot is MCM number in X-axis vs the corresponding RMS of the ADC distribution. See text for explanation . . . . .	73
5.1	Input Variables. These are variables associated with the thrown particles. Clockwise from the top left (a) Rapidity Distribution, (b) Pseudorapidity Distribution, (c) Transverse Momentum Distribution, (d) Transverse Mass Distribution . . . . .	78
5.2	Geometry to calculate charge deposition when a track goes through a single strip . . . . .	81
5.3	Geometry to calculate charge deposition when a track goes through multiple strips . . . . .	82
5.4	Charge Distribution in MVD from the Monte Carlo tracks . . . . .	83

5.5	PHENIX Run Condition : The total number of triggers recorded in PHENIX during the Au-Au run in the year of 2000[37]. . . . .	84
5.6	Trigger Selection from BBC Analog Sum and ZDC Energy Sum . . .	85
5.7	BBC and ZDC vertexes. The left plot is the BBC Z vertex, and the right one is ZDC Z vertex . . . . .	86
5.8	Correlation between BBC z-vertex and ZDC z-vertex . . . . .	86
5.9	Collision between the two beams. The top figure describes the head-on collision, the middle is for a mid-central collision and the bottom is for a peripheral collision . . . . .	87
5.10	BBC and ZDC quantities used for collision centrality determination. The left plot is the BBC charge sum, and the right one is ZDC energy	89
5.11	Centrality Selection from BBC Analog Sum and ZDC Energy Sum . .	90
5.12	Raw ADC Distribution for Strips . . . . .	93
5.13	Raw ADC Distribution for Strips vs Strip Number . . . . .	94
5.14	AMU vs ADC plot for Strip 330. In one event the data from one strip is handled by any one of the 64 AMU cells. So over a large number of events, all AMU cells contributes to the data handling from a particular strip. . . . .	95
5.15	Block Diagram of AMU-ADC Block. For the location of the AMU in the MVD electronics chain please refer to Chapter3, Section 3.5 . . .	95
5.16	Operation of AMU . . . . .	96
5.17	Normalization of Pedestals : (a) Raw, (b) After Normalization . . .	98
5.18	AMU vs ADC plot for Strip 330 after pedestal normalization . . . .	98
5.19	ADC Difference between strip 259 and 260. The top Plot is a plot of ADC Difference vs Event number, the bottom plot is 1-D plot of ADC Difference, fitted with a Gaussian . . . . .	100

5.20	ADC Difference between strip 0 and strips 1-31. The top Plot is a plot of ADC Difference vs Event number, the bottom plot is 1-D plot of ADC Difference, fitted with a Gaussian . . . . .	101
5.21	ADC of strips in Event number 416 and 417 for the high ADC clusters.	102
5.22	Raw Distribution . . . . .	104
5.23	Distribution After Event-by-Event Pedestal Identification . . . . .	105
5.24	Distribution After Event-by-Event Pedestal Subtraction . . . . .	105
5.25	Corrected ADC distribution after AMU event by event jumping correction. The AMU cell corrections are also applied before the event by event jumping correction was applied. . . . .	106
5.26	Fitting of Data. The corrected data is fitted with a Gaussian function for the pedestal and a Landau convoluted with a Gaussian for the MIPs.	113
5.27	Fitting of Data Showing the Different Region of Integration . . . . .	115
5.28	A part of the MVD: Strategy to Calculate $\eta$ of Strips . . . . .	117
5.29	A track passing through a number of Strips . . . . .	119
5.30	$dN/d\eta$ in the MVD Active Region. Here the min. bias distribution is plotted together with the distribution for the centrality classes 0%-5%,5%-10%,10%-15%,15%-20%,20%-25%,25%-30%,30%-35%. . . . .	122
5.31	Average $dN/d\eta$ vs $\eta$ for minimum-bias Events . . . . .	123
5.32	Input $\eta$ Distribution . . . . .	124
5.33	$\eta$ Distribution of the tracks accepted in MVD active Region . . . . .	124
5.34	Acceptance in MVD . . . . .	125
5.35	Comparison of Charged particle multiplicities in MVD and Pad Chamber in PHENIX. Also is shown the $dN/dE_T$ measured in the PHENIX Electromagnetic Calorimeter. . . . .	128

5.36 Comparison of Charged particle multiplicities per Participant vs The Number of Participants in MVD and Pad Chamber in PHENIX. Also is shown the $dN/dE_T$ measured in the PHENIX Electromagnetic Calorimeter. . . . .	129
5.37 Ratio of Charged particle multiplicities per Participant vs The Number of Participants in MVD and Pad Chamber in PHENIX. Also is shown the ratio to $dN/dE_T$ measured in the PHENIX Electromagnetic Calorimeter. . . . .	129
5.38 $dN/d\eta$ vs $\eta$ Distribution for top 5% Central events. Compared with the top 6% of PHOBOS data . . . . .	130
5.39 $dN/d\eta$ vs $\eta$ Distribution for 5% – 10% Central events. . . . .	130
5.40 $dN/d\eta$ vs $\eta$ Distribution for 10% – 15% Central events. . . . .	131
5.41 $dN/d\eta$ vs $\eta$ Distribution for 15% – 20% Central events. . . . .	131
5.42 $dN/d\eta$ vs $\eta$ Distribution for 20% – 25% Central events. . . . .	132
5.43 $dN/d\eta$ vs $\eta$ Distribution for 25% – 30% Central events. . . . .	132
5.44 $dN/d\eta$ vs $\eta$ Distribution for 30% – 35% Central events. . . . .	133
5.45 $dN/d\eta$ vs $\eta$ Distribution for 35% – 40% Central events. . . . .	133
5.46 $dN/d\eta$ vs $\eta$ Distribution for 40% – 45% Central events. . . . .	134
5.47 $dN/d\eta$ vs $\eta$ Distribution for 45% – 50% Central events. . . . .	134
6.1 The Mean $p_T$ Distribution for the $\sqrt{s} = 130$ GeV Data measured in the PHENIX experiment. The plots, clockwise from the top left, are for (a) 0%-5% central events,(a) 0%-10% central events, (a) 20%-30% central events,(a) 10%-20% central events . . . . .	137

6.2	Centrality dependence of charged particle multiplicity per participant for the Au-Au collision at $\sqrt{s}=130$ GeV. The red circles are the data points from MVD. Green triangles are the saturation model calculation[49]. Also shown in the blue squares the calculations from soft+hard model from Eqn.(6.10)[50]. . . . .	145
6.3	$dN/d\eta$ vs $\eta$ Distribution for top 5% Central events. Compared with the top 6% of PHOBOS data and Saturation Model of Kharzeev and Nardi[47] . . . . .	147
6.4	$dN/d\eta$ vs $\eta$ Distribution for 5% – 10% Central events. . . . .	147
6.5	$dN/d\eta$ vs $\eta$ Distribution for 10% – 15% Central events. . . . .	148
6.6	$dN/d\eta$ vs $\eta$ Distribution for 15% – 20% Central events. . . . .	148
6.7	$dN/d\eta$ vs $\eta$ Distribution for 20% – 25% Central events. . . . .	149
6.8	$dN/d\eta$ vs $\eta$ Distribution for 25% – 30% Central events. . . . .	149
6.9	$dN/d\eta$ vs $\eta$ Distribution for 30% – 35% Central events. . . . .	150
6.10	$dN/d\eta$ vs $\eta$ Distribution for 35% – 40% Central events. . . . .	150
6.11	$dN/d\eta$ vs $\eta$ Distribution for 40% – 45% Central events. . . . .	151
6.12	$dN/d\eta$ vs $\eta$ Distribution for 45% – 50% Central events. . . . .	151
A.1	PHENIX Data Production & Analysis Chain . . . . .	158
A.2	Flowchart for the Ntuple production for Analysis . . . . .	160

# Chapter 1

## Introduction

### 1.1 Quarks and Gluons: Basic Building Blocks of Normal Nuclear Matter

When we look at the material world with the eyes of a Nuclear Physicist we intend to know the basic building blocks of matter and how they behave. Lets try to break down a material and see how it is constituted. The first building block is the atom. Lets probe it, as did Rutherford about 100 years ago. We see it has a massive "nucleus" and circling around it are tiny electrons. Breaking the nucleus will give positive protons and neutral neutrons. Lets dig further. We see that protons and neutrons are not fundamental. They are composed of "quarks". Now how do the quarks interact? Lets look at the simple case atom and then we will find an analogy. The nucleus is positively charged and electrons are negative. The interaction between any electrically charged particles is called the coulomb interaction and the exchange photons during the interaction. As we will discuss more in detail later, quarks are "color" changed. So they have a "strong" interaction among themselves. Therefore, there must be a quanta associated with this interactions, which is called "gluon". Thus we have quarks and gluon's as fundamental building blocks of nuclear matter and a vast new area to explore.

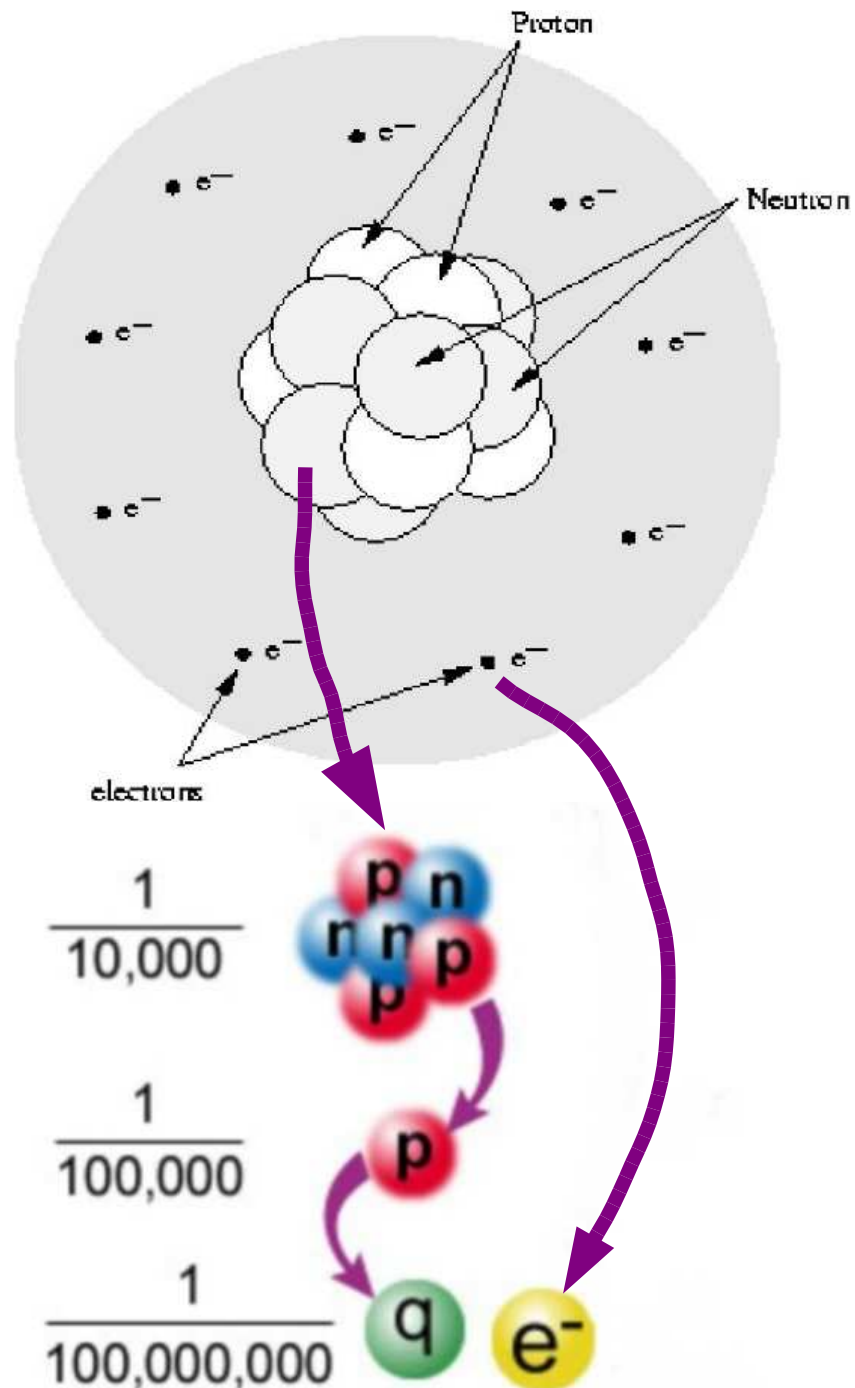


Figure 1.1: Structure of atoms and the size of its constituents with respect to the size of the atom

Quarks	$Q$	$I_z$	$C$	$S$	$T$	$B$	Mass (MeV)
$u$	$\frac{2}{3}$	$\frac{1}{2}$	0	0	0	0	$5.6 \pm 1.1$
$d$	$-\frac{1}{3}$	$-\frac{1}{2}$	0	0	0	0	$9.9 \pm 1.1$
$c$	$\frac{2}{3}$	0	1	0	0	0	$1350 \pm 50$
$s$	$-\frac{1}{3}$	0	0	-1	0	0	$199 \pm 33$
$t$	$\frac{2}{3}$	0	0	0	1	0	$>90000$
$b$	$-\frac{1}{3}$	0	0	0	0	-1	$\simeq 5000$

Table 1.1: Quark Properties

## 1.2 Quarks and Gluons: An Elaborative View

Quarks are the fundamental constituents of all nuclear matter. They experience all the known interactions: Strong, weak and electromagnetic, and gravitational. Quarks are spin 1/2 particles that appear point like. Quarks were proposed [1] by Gell-Mann and Zweig as a means for understanding SU(3) classification of hadrons. The observed patterns can be understood in terms of the hypothesis that hadrons are composite structures built from an elementary triplet of spin 1/2 quarks, corresponding to the fundamental representation of SU(3). The light mesons occur only in SU(3) Singlets and octets. Similarly, the light baryons are restricted to singlets, octets and decimates of SU(3). Quarks and their properties are summarized in Table 1.1. Here  $Q$  is the electric charge,  $I_z$  is the  $z$ -component of the Isospin,  $C$  is the charm quantum number,  $S$  is the strangeness,  $T$  is the topness, and  $B$  is the bottomness.

Each quark carries a *a baryon number* 1/3 and a *color*. There are three different colors a quark can carry. The interaction between the quarks depends on the colors of the interacting quarks, similar to the interaction between electric charges. For this reason, the color of a quark is sometimes called its *color charge*. By the exchange of a *gluon*, a quark with one color can interact with another quark of any other color.

It is generally held that the field theory for gluons and quarks belongs to special class of field theories known as *gauge field theories*. That is the interaction of the field theory can be represented as arising from the requirement that the Lagrangian is invariant under a local gauge transformation. This invariance is called a local gauge invariance, or simply *gauge invariance*. If the quanta of the gauge field have a rest mass, then the Lagrangian will not be invariant under a local gauge transformation. To maintain gauge invariance, the quanta of gauge field, the gluons, must be massless. In this respect, the gluons resemble photons, which are the quanta for the gauge field of electromagnetic interactions. They are spin-1 particles and are therefore bosons.

Let us now consider color force. It derives from the group  $SU(3)_{color}$ , so there are eight spin-1 massless gluons. Because  $SU(3)_{color}$  is non-Abelian, some of the gluons (in fact *six*) carry color charge and arbitrarily labeled red( $R$ ), green( $G$ ), and blue( $B$ ). A color combination of equal parts of  $R$ ,  $G$  and  $B$  is said to be white or color neutral; combination of equal parts of color and anticolor is color neutral too. Since particles are color neutral, quarks can combine only in the following way:

$$\begin{aligned} & R + B + G \\ & \overline{R} + \overline{B} + \overline{G} \\ & R + \overline{R} \\ & B + \overline{B} \\ & G + \overline{G} \end{aligned}$$

So, there are two quark particles ( $q$  and  $\overline{q}$ ), *i.e.* , Mesons and three quark particles *i.e.* , Baryons.

### 1.3 The Color Force

The gluons that mediate the color forces are massless, so we might expect it to have infinite range and otherwise behave like electromagnetic force, too: after all, the

photon is a massless vector boson, just like the gluons. But it turns out that the color force at long range does not drop off like Coulomb's law. On the contrary, there are indications that it is independent of distance, or at any rate changes very slowly with distance. This dramatic difference between color force and the electromagnetic force is entirely due to the vacuum polarization. The vacuum is the ground state. However, the *vacuum* is not really empty. In fact, according to the uncertainty principle particle-antiparticle pairs may be present in the vacuum for a certain amount of time, which is proportional to their energy. These electron-positron pairs can screen the electric charge as seen in Fig.(1.2). Therefore, the electromagnetic coupling constant increases as the distance decreases. The charge and the distance is related by the equation:

$$e^2(r) = \frac{e^2(r_0)}{1 + \frac{2e^2(r_0)}{3\pi} \ln \frac{r}{r_0}}, \quad (1.1)$$

where  $r$  is the distance from the charge which is localized at  $r_0$  (coordinate of the charge). The QED coupling constant is given by,

$$\alpha_{em}(r) \simeq \frac{3\pi}{2 \ln(r/r_0)}. \quad (1.2)$$

In QCD the situation is qualitatively different, and corresponds to *anti*-screening – the charge is small at short distances and grows at larger distances. This property of the theory, discovered by Gross, Wilczek, and Politzer [2], is called *asymptotic freedom*. Due to the fact that gluons carry color, the behavior of the effective charge  $\alpha_s = g^2/4\pi$  changes from the familiar from QED screening to anti–screening:

$$\alpha_s(r) \simeq \frac{3\pi}{(11N_c/2 - N_f) \ln(r_0/r)}; \quad (1.3)$$

where  $N_f$  is the number of quark flavors, and  $N_c = 3$  is the number of flavors. So the color force at short distance (or high momentum  $q^2$ ) drops rapidly. The vanishing of QCD coupling constant at short distances, (the *asymptotic freedom*) , has often been taken to imply that interactions among quarks and gluons are negligible in the limit of high temperature of high density.

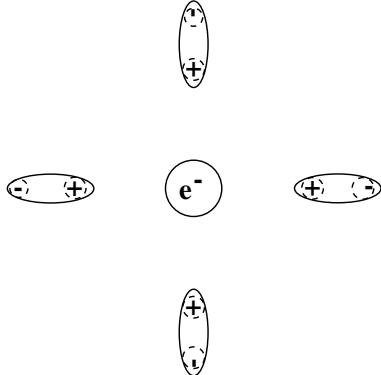


Figure 1.2: In QED, virtual electron-positron pairs from the vacuum screen the bare charge of the electron. The larger the distance, the more pairs are present to screen the bare charge and the electromagnetic coupling decreases. Conversely, the coupling is larger when probed at short distances.

## 1.4 Quark Gluon Plasma

The interaction between quarks becomes weaker at short distances. Now the question is under what conditions the nucleons, or more generally, the hadrons, lose their identity. The QCD lattice Monte-Carlo calculations[3] have given an answer to this question: at temperatures above 200 MeV nuclear matter should melt into a soup of quarks and gluons and the identity of hadrons should be completely lost.

According to QCD, quark-quark ( $qq$ ) or quark-antiquark ( $q\bar{q}$ ) interactions become stronger as the  $qq$  or  $q\bar{q}$  distance increases. This is the reason why quarks are confined within the hadronic scale of  $\sim 1 \text{ fm}$ . At high temperatures many  $q$ 's and  $\bar{q}$ 's are created so that at sufficiently high temperatures the inter-quark distance becomes much smaller than this hadronic scale, and there, the  $qq$  (or  $q\bar{q}$ ) interactions become negligibly small. Then each  $q$  (or  $\bar{q}$ ) behaves as if it is a free particle; this is the reason why this system is called the *quark-gluon plasma*. In a free gas of quarks we expect that the Stefan-Boltzmann law ( $\epsilon \propto T^4$ ) holds as shown in the Fig.(1.3), where  $\epsilon$  is the energy density. In fact many QCD lattice Monte-Carlo calculations show that Stefan-Boltzmann law holds at sufficiently high temperatures[3]. If the nucleons and

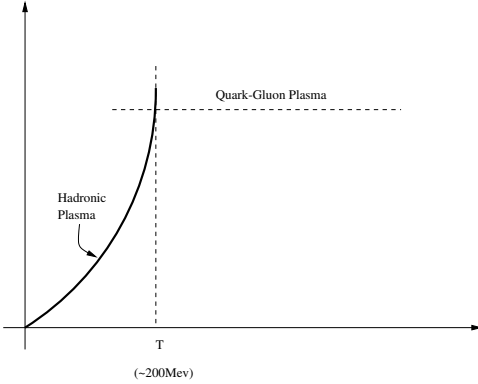


Figure 1.3: Stefan-Boltzmann law for nuclear matter

pions keep their identity, then the system is expected to have a maximum temperature  $T_C$ , which is called *Hagedorn limiting Temperature*[4]. We know that the temperature of liquid water never exceeds  $100^{\circ}\text{C}$ . At around  $100^{\circ}\text{C}$ , even as heat is supplied, most of the heat energy is used to form bubbles and not to increase kinetic energy of water molecules. In the hadronic gas, this bubble is analogous to the pion and, similar to the case of water, most of the heat energy is used to form pion bubbles at  $T \sim T_C$ . The boiling temperature ( $T_C$ ) in this case is therefore of the order of pion mass of  $\sim 140$  MeV.

Therefore, if the system is heated (increase), It would first follow the phase curve for a hadronic gas but at  $T \sim T_c$  it would then turn into the phase of free gas of quarks by deconfining hadrons into quarks and gluons. Namely, we expect a phase transition at  $T \sim T_c$ . The energy density required for this phase transition is estimated to be  $\epsilon \sim$  a few  $\text{GeV}/\text{fm}^3$ .

Similarly, when the nucleus is compressed, the neighboring nucleons start to overlap each other and, again, nucleons are expected to completely lose their identity at sufficiently high densities, to melt into quarks and gluons. Based on above considerations the famous phase diagram for expected new phases of nuclear matter was drawn, as shown in Fig.(1.4).

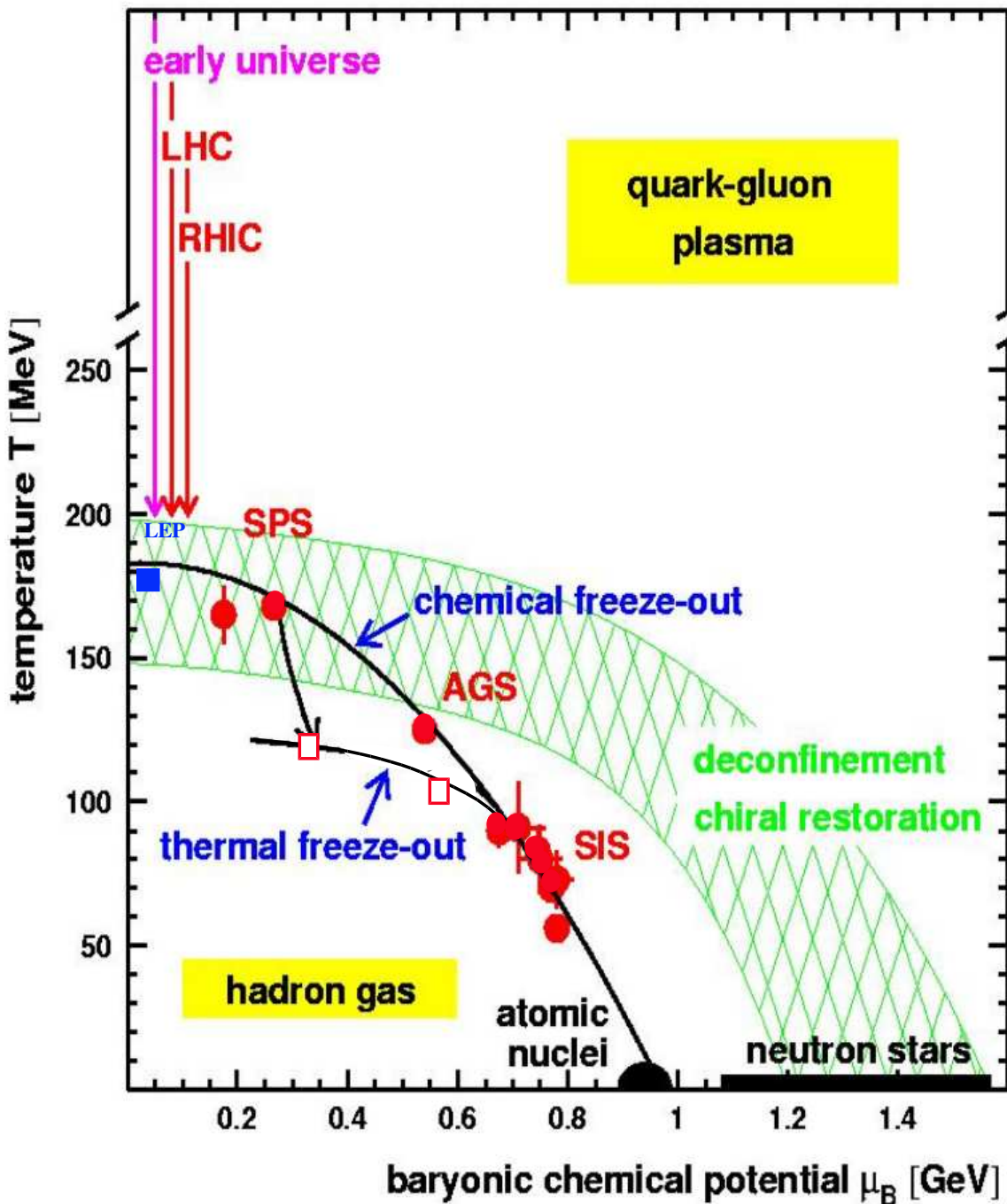


Figure 1.4: Phase Diagram for Nuclear Matter

## 1.5 Signature of Quark-Gluon Plasma: Theoretical Guidance

Experimental investigations of the quark-gluon plasma require the identification of appropriate experimental tools for observing its formation and studying its properties. One serious problem is that the size and lifetime of the plasma are expected to be small, at most a few fermi in diameter and perhaps 5 to 10 fm/c in duration. Furthermore, signals of the quark-gluon plasma compete with backgrounds emitted from the hot hadronic gas phase that follows the hadronization of the plasma, and are modified by final state interactions in the hadronic phase. In spite of this, a wealth of ideas has been proposed in the past decade as to how the identification and investigation of the short-lived quark-gluon plasma phase could be accomplished.

We here list some of the theoretical guidance on the possible signatures of the formation of quark-gluon plasma [9, 10]

### 1.5.1 Lattice Gauge Theory

The equations in Quantum Chromo Dynamics (QCD) are very difficult to solve or approximate using analytical techniques. The lattice gauge theory[5, 6] allows for a potentially exact, nonperturbative numerical calculation of observables in QCD. The standard numerical approach in lattice gauge theory is to discretize the continuum field theory onto a grid or *lattice* and use Monte Carlo simulations. The calculations in the lattice gauge theory need fast efficient parallel program running on many processors to compute observable quantities.

1. Simulations without dynamical quarks exhibit a first-order phase transition at  $T_c \simeq 260\text{MeV}$ . Below  $T_c$  free energy of isolated quarks is infinite, and above  $T_c$  it is finite. This is deconfinement.
2. At the same temperature range, quarks appear to be massless as opposed to the

hadronic matter when quarks confined in the hadrons do not appear as nearly massless constituents but are endowed with a dynamically generated mass of several hundred MeV. This is called the chiral symmetry restoration, hence deconfinement and chiral symmetry go hand-in-hand.

### 1.5.2 Parton Cascade Model

The models are based on the concept that the colliding nuclei can be decomposed into their parton substructure. The perturbative interactions among these partons can then be followed until thermalization. Parton model evolve partonic degrees of freedom. They are therefore mostly applied to study the initial compressional and high-density phase of ultra-relativistic heavy ion collisions.

1. The models predict a very rapid thermalization of the deposited energy. The models predict that thermalization occurs on a proper time scale of 0.3-0.5 fm/c at RHIC energies.
2. Partonic cascades can lead to a rather uneven energy deposition, because of cross-section fluctuations. “Hot spots”, caused by strongly inelastic parton scatterings could lead to observable, non-statistical fluctuations in the final hadron distribution.

### 1.5.3 Hadronic Transport Models

Hadronic Transport Models treat relativistic heavy-ion collisions as sequences of binary/N-body collisions of mesons, baryons, strings, and their constituents.

1. Hadronic transport models are critical for assessing the influence of ordinary or exotic hadronic phenomena on the observables proposed to search for QGP. They, therefore, provide a background basis to evaluate whether an observable shows evidence for non-hadron physics

From the above discussion for the theoretical guidance, we see that there are many probable signatures for the formation of the quark-gluon plasma . It is obviously difficult to find a robust theoretical description of relativistic heavy ion collisions involving the QCD phase transition to predict observables. The theory in this situation can thus serve mainly to motivate particular experimental studies. The strategy adopted by the experiments in the heavy-ion collisions to Detect QGP is to look at as many signatures as possible, *simultaneously* .

## 1.6 Why Heavy Ion Collisions

The physical environment in which the critical conditions of temperature and density  $\rho_c$  can be achieved are known to be: the early universe[7], the core of neutron stars[7], and heavy ion collisions[8]. It can immediately be understood that the best chance for actually studying the properties of QGP is in the laboratory by colliding the heavy ions[8]. In the heavy ion collisions one has an access to soft events with unusually large multiplicities where the energy is distributed as evenly as possible among a very large number of secondaries to probe hadronic matter at high density near thermodynamic equilibrium.

The QGP phase lies between the Early Universe and the neutron Star regimes on the phase diagram in Fig. 1.4; heavy ion collisions at various beam energies can probe the entire region in between these two extremes. Collisions between ultra-relativistic heavy-ion collisions thus offer the best chance to create and observe the QGP in the laboratory. For a given accelerator energy and thus center-of-momentum (cm) energy nuclei that are as heavy as possible produce the highest energy density. To enhance the possibility of observing the QGP, we want high energy density over a sufficiently large volume, with dimensions larger than the scattering length of the constituents, so that equilibrium thermodynamics may be applicable. Once created, the system must exist long enough to equilibrate so that a phase in the thermodynamic

sense can be established. These considerations led to the experimental programs at Brookhaven(AGS) and CERN (SPS). At each of these facilities it was expected to create a QGP in a baryon-rich environment. The quest for a QGP in a region with no net baryon density, led to the decision to build the Relativistic Heavy Ion collider(RHIC) at Brookhaven and the large Hadron collider(LHC) at CERN to be constructed.

## 1.7 Experimental Signatures

The heavy-ion experiments give an opportunity to study the proposed theoretical signatures of quark-gluon plasma formation. We here briefly discuss the most promising of the signatures[11, 12]. In order to connect between the many proposed quark-gluon plasma signatures they are roughly grouped in five categories, according to the physical properties of super dense hadronic matter to which they are sensitive. These are:

1. *Kinematical Probes*, thermodynamic variables measuring the equation of state;
2. *Electromagnetic Probes*, probes of the electromagnetic response function;
3. *Probes of Deconfinement*;
4. *Probes of Chiral Symmetry Restoration*;
5. *Hard QCD Probes*.

### Kinematical Probes

The signatures of quark-gluon plasma can be studied by determining the energy density  $\epsilon$ , pressure  $P$ , and entropy density  $s$  of super dense hadronic matter as a function of the temperature  $T$  and the baryochemical potential  $\mu_B$ . Measurable observables that are related to the variables  $T$ ,  $s$ , and  $\epsilon$ , are customarily identified

with the average transverse momentum  $\langle p_T \rangle$ , the hadron rapidity distribution  $dN/d\eta$ , and the transverse energy  $dE_T/d\eta$ , respectively [13]. In the present thesis we intend to measure the charged particle multiplicity  $dN/d\eta$  and the determination of the energy density  $\epsilon$ .

### Electromagnetic Probes

Photons and lepton pairs provide probes of the interior of the quark-gluon plasma during the earliest and hottest phase of the evolution of the fireball since they are not affected by final state interactions.

Lepton pairs from hadronic sources in the invariant mass range between 0.5 and 1 GeV are important signals of the dense hadronic matter formed in nuclear collisions [14, 15]. They provide exclusive information about possible medium modifications of hadronic properties, especially of the  $\rho$ -meson, at high density [16, 17]. Another strategy for using the leptonic  $\rho$ -meson decay as a probe of the hadronic phase of the fireball is based on the idea that the  $\rho$ -peak is expected to grow strongly relative to the  $\omega$  peak in the lepton pair mass spectrum, if the fireball lives substantially longer than  $2 \text{ fm}/c$ . Because of the short average lifetime of the  $\rho$ -meson, the  $\rho/\omega$  ratio can therefore serve as a fast “clock” for the fireball lifetime [18].

In measurements of direct photons, better control of experimental conditions is necessary in order to reduce the systematics to the level required for measuring signals only a few percent above background. Theoretically, it will be very important to understand the relationship between the large excess of low mass electron pairs (virtual photons) and a weak direct photon signal.

### Probes of Deconfinement

Studies of the relative suppression of  $J/\psi$  and  $\psi'$  at the SPS in central collisions of very heavy nuclei should provide crucial information on the relative roles of nuclear rescattering, color screening and deconfinement at the highest energy densities. Mea-

surement of  $J/\psi$  and  $\psi'$  in A+p interactions using reverse kinematics to measure the  $J/\psi$ -hadron rescattering cross sections will be important to understanding the role of rescattering in the break-up of the  $J/\psi$  and  $\psi'$ . This is an essential step toward isolating the suppression due to screening in a quark-gluon plasma. It will be important to vary the projectile and target masses to determine the A-dependence of the various processes for a complete understanding of the suppression.

At the higher incident energies of RHIC and the LHC, the energy densities will be more than a factor of ten greater than in present measurements at the SPS. Thus the differences in the  $J/\psi$ ,  $\psi'$ ,  $\Upsilon$  and  $\Upsilon'$  suppression and the screening due to quark-gluon plasma formation should be accentuated.

### Probes of Chiral Symmetry Restoration

The two most often proposed signatures for a (partial) restoration of Chiral symmetry in dense hadronic matter are enhancements in strangeness and antibaryon production. The basic argument in both cases is the reduction in the threshold for production of strange hadrons (from about 700 MeV to 300 MeV) and baryon-antibaryon pairs (from about 2 GeV to almost zero). The enhanced strange quark production in a chirally restored, deconfined quark-gluon plasma[19] leads to chemical equilibrium abundances for all strange hadrons, which would be difficult to understand on the basis of hadronic reactions alone[20].

It has also been pointed out that strange particles, and especially antibaryons, would be produced more abundantly, if their masses would be modified even in the hadronic phase due to medium effects [21]. An enhancement of strange particle production in nuclear collisions has been observed by many experiments[22]. Vector mesons such as  $\phi$ ,  $\rho$  and  $\omega$  are considered as probes for the chiral symmetry restoration. For example, the mass and width of  $\phi$ -meson are expected to be changed as a consequence of the expected chiral symmetry restoration in heavy-ion collisions. Also

the branching ratio of  $\phi \rightarrow K^+K^-$  and  $\phi \rightarrow e^+e^-$  is expected to be changed.

## Hard QCD Probes

Collisions at RHIC and the LHC will exhibit effects of hard scattering of partons. Such QCD hard scattering processes will result in the production of high  $p_T$  particles and jets, which will be measured in experiments at RHIC and the LHC to test the propagation of high  $p_T$  partons in highly excited matter and a quark-gluon plasma.

In Fig.(1.5) we list some of the most promising signatures. The potential signatures are investigated as a function of the energy density  $\epsilon$  or a quantity closely related to the energy density, such as the rapidity density of the transverse energy  $dE_T/dy$  or the pseudorapidity density of the charged particle multiplicity  $dN/d\eta$  as in the Bjorken formula[23]:

$$\epsilon \simeq \frac{1}{\pi R^2 \tau_0} \frac{dE_T}{dy} \simeq \frac{\langle p_t \rangle}{\pi R^2 \tau_0} \frac{3}{2} \frac{dN}{d\eta} \quad (1.4)$$

where  $\tau_0$  is the formation time, is usually taken as 1fm/c, and  $\pi R^2$  is the effective area of collision. With  $R \sim A^{1/3} \sim 6$  fm for gold nucleus. The relations of the rapidity and pseudorapidity will be described in the next chapter. In Fig.(1.5), the potential signatures are shown as a function of the pseudorapidity density of the transverse energy  $dE_T/d\eta$ . The new phase of matter is expected above the critical energy density  $\epsilon_c$ . For instance, the suppression of  $J/\psi$  and  $\psi'$  production relative to that of the  $\Upsilon$  above  $\epsilon_c$  may be a potential signature for the formation of quark-gluon plasma . The in-medium modification of meson properties due to the restoration of chiral symmetry is predicted to cause changes in the mass and width of the vector meson. For example, the branching ratio of  $\phi$  mesons decaying via  $K^+K^-$  or  $e^+e^-$  channels may change. For more information on the signatures of the quark-gluon plasma , please see Reference[12].

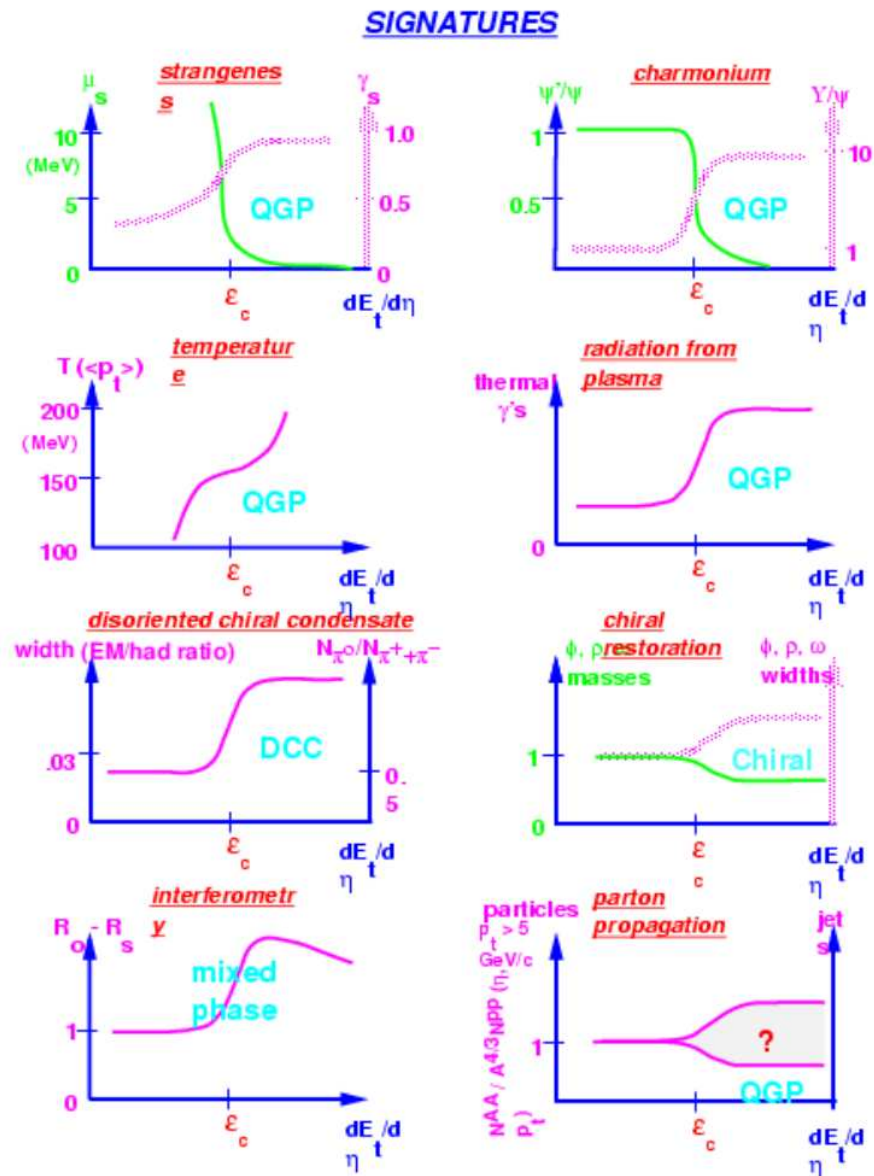


Figure 1.5: Signature of Quark-Gluon Plasma. The potential signatures are shown as a function of the pseudorapidity density of the transverse energy  $dE_t/d\eta$ . The new phase of matter is expected above the critical energy density  $\epsilon_c$ .

## 1.8 Experiments

### 1.8.1 Experimental Conditions

The techniques used in experiments studying relativistic nucleus-nucleus collisions are similar to those used in high energy physics experiments. The primary difference is that the particle multiplicities and the backgrounds for various processes differ between the nuclear and particle physics environments. For central collisions, with impact parameters near zero, the particle multiplicities scale approximately as the mass of the colliding system and therefore, with nuclear masses around 200, can be a factor of 200 times higher in collisions of heavy nuclei compared to collisions between protons at the same energy. The multiplicities scale weakly as a function of energy with  $dn/dy(ycm) \sim \ln(\sqrt{s})$ . Likewise, the combinatorial backgrounds underlying processes such as Drell-Yan production, particle and resonance decays, and photon production increase more than linearly with (and usually as the square of) increasing primary particle multiplicities, complicating reconstruction of these signals.

### 1.8.2 Present Relativistic Heavy Ion Accelerators

There were two research facilities for relativistic heavy ion experiments, focusing on dense hadronic matter and signatures of quark- gluon plasma formation recently finished taking data. These are the Brookhaven Alternating Gradient Synchrotron (AGS) and the CERN Super Proton Synchrotron (SPS), both were in operation with heavy ions since 1986. Experiments utilize nuclear beams ranging from protons to gold with momentum up to  $29(Z/A)$  GeV/c from the AGS and from protons to lead with momentum up to  $400(Z/A)$  GeV/c from the SPS, where  $Z$  is the element number and  $A$  is the atomic mass number of the nuclear beam. These correspond to center-of-mass energies per nucleon pair of 4.84 GeV for Au+Au at the AGS and 17.2 GeV for Pb+Pb at the SPS. Simply scaling the particle multiplicities measured

in pp interactions by  $A$ , the charged particle multiplicity density at midrapidity for these systems is approximately 150 per unit rapidity at the AGS and 270 per unit rapidity at the SPS.

### 1.8.3 Heavy Ion Colliders

In the summer of 2000, a new era started in the field of heavy-ion Physics when the Relativistic Heavy Ion Collider (RHIC) at the Brookhaven National Laboratory collided two gold beams at the center-of-mass energies of 56 GeV, which in a few weeks went to 130 GeV per nucleon. RHIC collided Au-Au beams at  $\sqrt{s} = 200$  GeV per nucleon in the run in 2001. Also it collided p-p at  $\sqrt{s} = 200$  in the same time span. RHIC is capable of accelerating and colliding ions from protons to heavy nuclei, *e.g.* Au-Au, p-p, d-A and so on. The design luminosity for Au+Au is  $2 \times 10^{26} \text{ cm}^{-2} \text{ s}^{-1}$ . Near head-on collisions of Au+Au at RHIC produce from 500 to 1500 charged particles per unit pseudorapidity at mid rapidity in a single collision. There are two large detector systems, namely PHENIX and STAR and two small detectors namely PHOBOS and BRAHMS are currently are currently analyzing the products of these interactions for formation of a quark-gluon plasma and a possible chiral phase transition.

Heavy ion physics research will also be an integral part of the program for the Large Hadron Collider (LHC), to be constructed at CERN, the European Center for Nuclear Physics, in Geneva, Switzerland. For Pb nuclei, the c.m. energies at the LHC will be 5.4 TeV per nucleon pair with luminosities of  $10^{27} \text{ cm}^{-2} \text{ s}^{-1}$ . Predictions for the charged particle densities at the LHC for near head-on collisions of Pb+Pb range from 2000 to 8000 per unit pseudorapidity. The large uncertainty in these numbers arises primarily from the present lack of information on the distributions of soft gluons in nuclei.

## 1.9 Summary

The quark-gluon plasma has yet to be uniquely observed or identified. There are no well-defined theoretical predictions for the QGP formation. So, heavy ion experiments look for the various QGP formation signatures simultaneously as a function of energy density. These signatures are being pursued vigorously in experiments at the present day relativistic heavy ion accelerators experiments at RHIC, and just concluded the AGS and SPS, and in the construction of relativistic heavy ion experiment LHC. Fig.(1.5) provides an overview of the various signatures that the PHENIX experiment at RHIC will try to explore. Similar program are followed in other heavy-ion experiments.

It is the goal of the field of heavy ion physics to explore the various regions of the phase diagram of nuclear matter (Figure1.4) and to map out its properties at these various temperatures and pressures. It is of special interest to relativistic heavy ion physics to investigate regions of higher temperatures and densities for formation of a quark-gluon plasma and a chiral phase transition. The Relativistic Heavy Ion Collider experiments are currently searching for the signatures of these phase transitions, and measuring observables that reflect variables of the state of the system, in order to determine the characteristics of nuclear matter at high densities.

## 1.10 Organization of the Thesis

The measurement of the Charged Particle Multiplicity with the PHENIX Multiplicity and Vertex Detector in Au-Au collisions at  $\sqrt{s} = 130$  GeV are presented. In the analysis the data collected in the PHENIX experiment from the first RHIC Au-Au run is used.

In Chapter 2 we present the relativistic kinematic variables relevant for the present analysis. Emphasis was given on the rapidity and pseudorapidity variables. The

machine and the detector are presented in chapter 3. We present a brief description on the Relativistic Heavy Ion Collider facility at Brookhaven National Laboratory. Then we discuss about the various detectors in PHENIX experiment at RHIC and their basic working principles.

In Chapter 4 we discuss about the PHENIX Multiplicity and Vertex Detector. At the beginning of the chapter we introduced the general working principle of silicon detectors. We then give detail account for the detector we used for our analysis. Also a brief description on the online monitoring employed during run is presented.

In Chapter 5 we present the details of the analysis procedures. We steps involving the data selection, centrality selection and track selections were discussed in details. The corrections applied in order to extract the result are presented. We then present the result and and comparison of the measurements with other measurements in RHIC.

In Chapter 6 we make a model comparison of the result. The HIJING model of Gyulassy and Wang and the High Density QCD Saturation model of Kharzeev and Nardi were compared with the data. The centrality dependence of the multiplicity density as a function of the participant nucleon in the collision was compared with the Saturation model of Kharzeev and Nardi.

# Chapter 2

## Kinematics

### 2.1 Relativistic Kinematics

In Relativistic Heavy-ion collisions and in many other high-energy reaction processes, it is convenient to use kinematic variables that have simple properties under a change of frame of reference. It is worthwhile to discuss the kinematic variables used in Relativistic Heavy-Ion collisions in detail in order to establish the proper language for relativistic reactions.

#### 2.1.1 Conventions & Notations

The beam axis is defined as the  $z$ -axis. Components along this axis are called the *longitudinal* components. The  $x$ -axis is perpendicular to  $z$ -axis and tangent to the earth's surface.  $y$ -axis is perpendicular to both the  $z$  and  $x$  axes. Any component lying in the  $x - y$ -plane is called the *transverse* components.

$\theta$  is the polar angle measured from the  $z$ -axis.  $\phi$  is the azimuthal angle, measured clockwise from the  $x$ -axis. A diagram for the coordinates is shown in Fig.(2.1). Let us consider a particle characterize by its rest mass  $m$  and momentum  $p$ . The Particle is observed from the system of reference  $S$  and from another system  $S'$  that moves relative to  $S$  with velocity  $v/c = \beta_G$  in the direction of  $z$ -axis as shown in Fig.(2.1).

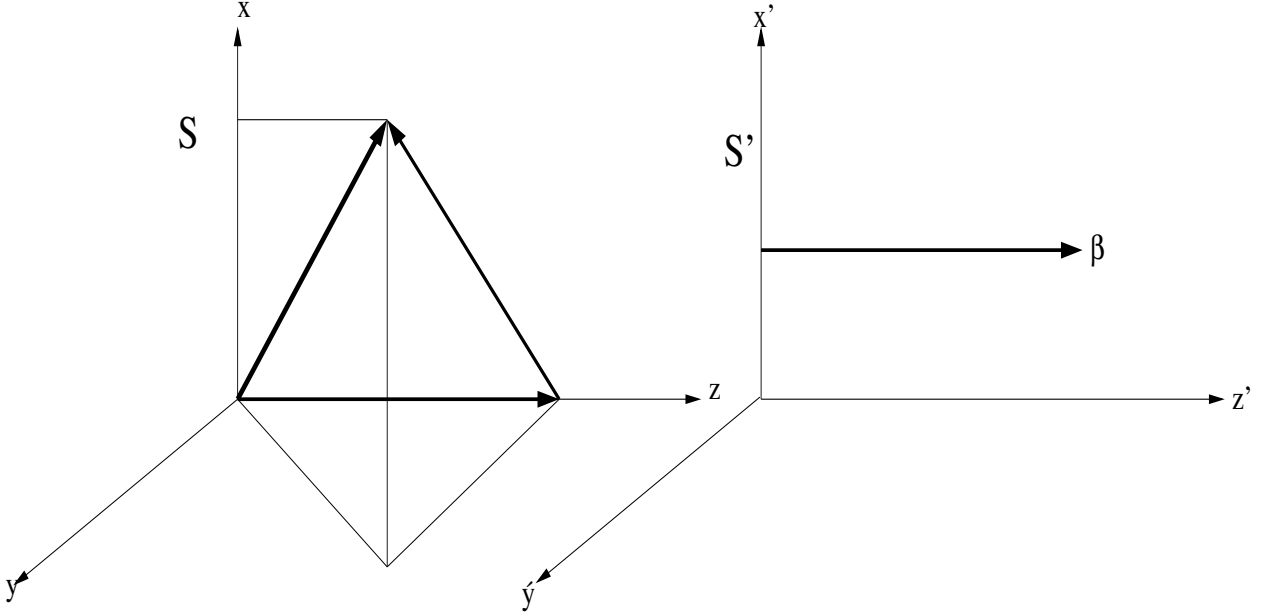


Figure 2.1: Coordinate System

Let us define the momentum along the  $z$ -axis of the particle via the polar angle  $\theta$  as:

$$p_{\parallel} = p \cos \theta \equiv p_z \quad (2.1)$$

and the transverse momentum

$$p_t = \sqrt{p_x^2 + p_y^2} = p \sin \theta \quad (2.2)$$

We then have

$$p = \sqrt{p_{\parallel}^2 + p_t^2} = m\gamma\beta \quad (2.3)$$

and the energy

$$E = \sqrt{p^2 + m^2} = m\gamma \quad (2.4)$$

$p_t$  is Lorentz invariant, but  $E$  and  $p_{\parallel}$  transform as

$$\begin{pmatrix} E' \\ p'_{\parallel} \end{pmatrix} = \begin{pmatrix} \gamma_G & -\beta_G \gamma_G \\ -\beta_G \gamma_G & \gamma_G \end{pmatrix} \begin{pmatrix} E \\ p_{\parallel} \end{pmatrix} \quad (2.5)$$

with

$$\gamma = (1 - \beta^2)^{-1/2} = E/m \quad (2.6)$$

Another quantity we need to introduce is the transverse mass:

$$m_t = \sqrt{p_t^2 + m^2} \quad (2.7)$$

### 2.1.2 Rapidity Variable

One of the most popular variable used commonly to describe the kinematic condition of a particle is the rapidity variable  $y$ . The rapidity of a particle is defined in terms of its energy-momentum components  $p$  and  $p_z$  by

$$y = \frac{1}{2} \ln \left( \frac{E + p_z}{E - p_z} \right) = \frac{1}{2} \ln \left( \frac{1 + \beta \cos \theta}{1 - \beta \cos \theta} \right) \quad (2.8)$$

For a particle moving along the  $z$ -axis with  $\theta = 0$ , the rapidity is

$$y_z = \frac{1}{2} \ln \left( \frac{1 + \beta}{1 - \beta} \right) \quad (2.9)$$

Rapidity is a dimensionless quantity. In the nonrelativistic limit, the rapidity of a particle traveling in the longitudinal direction is equal to the velocity of the particle in units of the speed of light. The rapidity variable depends on the frame of reference, but the dependence is very simple. The rapidity of the particle in one frame of reference is related to the rapidity in another Lorentz frame of reference by an additive constant. The system  $S'$  moves with rapidity

$$y_G = \frac{1}{2} \ln \left( \frac{1 + \beta_G}{1 - \beta_G} \right) \quad (2.10)$$

Thus, using Eq.(2.5) and Eq.(2.8) we find

$$\begin{aligned} y' &= \frac{1}{2} \ln \left( \frac{E' + p'_z}{E' - p'_z} \right) = \frac{1}{2} \ln \left( \frac{\gamma E - \beta \gamma p_z - \beta \gamma E + \gamma p_z}{\gamma E - \beta \gamma p_z + \beta \gamma E - \gamma p_z} \right) \\ &= \frac{1}{2} \ln \left( \frac{(E' + p'_z)(1 - \beta)}{(E' - p'_z)(1 + \beta)} \right) \\ &= \frac{1}{2} \ln \left( \frac{E + p_z}{E - p_z} \right) + \frac{1}{2} \ln \left( \frac{1 + \beta}{1 - \beta} \right) = y + y_G \end{aligned} \quad (2.11)$$

From the definition Eq.(2.8) we have

$$e^y = \sqrt{\frac{E + p_z}{E - p_z}} \quad (2.12)$$

therefore;

$$E = m_t \cosh y \quad (2.13)$$

$$p_z = m_t \sinh y \quad (2.14)$$

where

$$m_t^2 = m^2 + p_t^2 \quad (2.15)$$

these relations are useful relations linking the components of the momentum with the rapidity variable.

### 2.1.3 Pseudorapidity Variable

To characterize the rapidity of a particle, it is necessary to measure two quantities of the particle such as its energy and its longitudinal momentum. In many experiments, it is only possible to measure the angle of the particle relative to the beam axis. In that case it is convenient to utilize this information by using the *pseudorapidity* variable  $\eta$  to characterize the detected particle. The Pseudorapidity variable of a particle  $c$  is defined as

$$\eta = -\ln \tan \theta/2, \quad (2.16)$$

where  $\theta$  is the angle of between the particle momentum  $p$  and the beam axis.

Thus we see that

$$p = p_t \cosh \eta \quad (2.17)$$

$$p_z = p_t \sinh \eta \quad (2.18)$$

Using these results we can express rapidity variable  $y$  in terms of the pseudorapidity variable  $\eta$  as

$$y = \frac{1}{2} \ln \left[ \frac{\sqrt{p_t^2 \cosh^2 \eta + m^2} + p_t \sinh \eta}{\sqrt{p_t^2 \cosh^2 \eta + m^2} - p_t \sinh \eta} \right] \quad (2.19)$$

or conversely,

$$\eta = \frac{1}{2} \ln \left[ \frac{\sqrt{m_t^2 \cosh^2 y - m^2} + m_t \sinh y}{\sqrt{m_t^2 \cosh^2 y - m^2} - m_t \sinh y} \right] \quad (2.20)$$

If the particle has a distribution  $dN/dydp_t$  in terms of the rapidity variable  $y$ , then the distribution in the pseudorapidity variable  $\eta$  is

$$\frac{dN}{d\eta dp_t} = \sqrt{1 - \frac{m^2}{m_t^2 \cosh^2 y}} \frac{dN}{dy dp_t} \quad (2.21)$$

In many experiments, only the pseudorapidity variable  $\eta$  of the detected particles are measured to give  $dN/d\eta$ , which is an integral of  $dN/d\eta dp_t$  with respect to the transverse momentum. From Eq.(2.21) we can infer that

- in the region of  $y$  much greater than zero,  $dN/d\eta$  and  $dN/dy$  are approximately the same.
- at  $y$  close to zero, there is a small depression of the  $dN/d\eta$  distribution relative to the  $dN/dy$  distribution.

As mentioned earlier, the pseudorapidity is a useful quantity for experiments. It is a dimensionless quantity and the experiments need to measure only one quantity, the angle  $\theta$ , as opposed to the two quantities energy and longitudinal momentum for rapidity. The pseudorapidity  $\eta$  is approximately equal to the rapidity  $y$  for  $p \gg m$  and  $\theta \gg 1/\gamma$ , where  $\gamma = E/m$ .

# Chapter 3

## Overview of PHENIX

### 3.1 Introduction

RHIC collides two beams of gold ions head-on when they're traveling at nearly the speed of light. The beams will be traveling in opposite directions around RHIC's 2.4-mile, two-lane "racetrack." At six intersections, the lanes will cross, leading to a "demolition derby". In the above cartoon we can see the way the collisions occur in RHIC. In the first picture we see that the two ions (traveling from the left and right sides of the picture toward the center) approach one another. The ions are flat, instead of their usual spherical shape, because they're going so fast( $0.9995c$ ). In the second and the third picture the two ions collide, smashing into one another and then passing through each other. Some of the energy they had before the collision is transformed into intense heat and new particles. If conditions are right, the collision

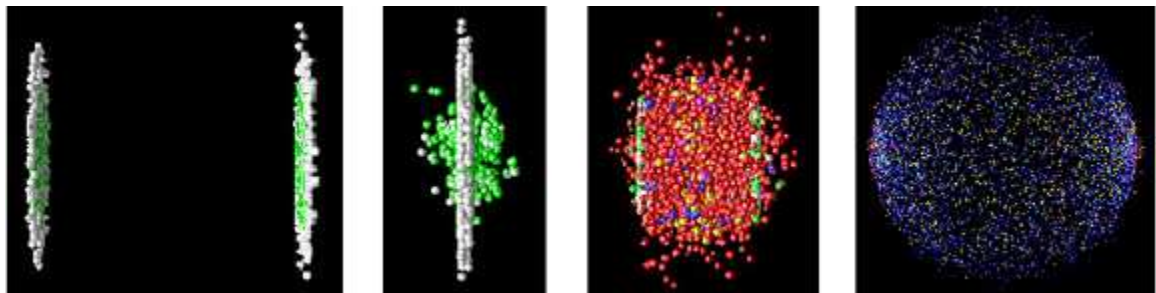


Figure 3.1: Gold-Gold Collision at RHIC

”melts” the protons and neutrons and, for a brief instant, liberates the quarks and gluons. In the fourth picture, just after the collision, thousands more particles form as the area cools off. Each of these particles is a clue to what happened inside the collision zone – and PHENIX and three other experiments will sift through those clues for interesting information.

## 3.2 The Relativistic Heavy Ion Collider

The Relativistic Heavy Ion Collider is designed to accelerate gold nuclei in two opposite rings to energies up to 200 GeV per nucleon pair in the center of mass. In the first year of the commissioning of RHIC it could attain up to  $\sqrt{s} = 130$  GeV per nucleon. RHIC also has the capability to collide other heavy ion species as well as polarized protons. As of today, RHIC has successfully collided Au-Au at  $\sqrt{s} = 200$  GeV per nucleon and also p-p during the second run in the year of 2001-2002. The Data for these collisions are being analyzed now. But this thesis uses the data collected in the first RHIC run at  $\sqrt{s} = 130$  GeV per nucleon.

The process of accelerating a gold ion involves several accelerators that make up the RHIC complex. Fig. 3.2 shows the RHIC complex.

The ion beam starts its journey in the Tandem Van de Graaff. It consists of two electrostatic accelerators, each 24 meters of length and capable of producing voltages up to 15 million volts. These electrostatic accelerators can provide up to 40 different kinds of ions, including gold.

The ion beams begin their journey here at the accelerators and go to the Heavy Ion Transfer Line (HITL). Once the ions reach the HITL, they are carried through a vacuum using a magnetic field, traveling at 5% of the speed of light. Then the ions are provided with more energy at the Booster accelerator with electromagnetic waves. In the Booster accelerator they reach a speed of 37% that of light. From there, the ions make their way to the AGS where they reach 99.7% of the speed of light. The

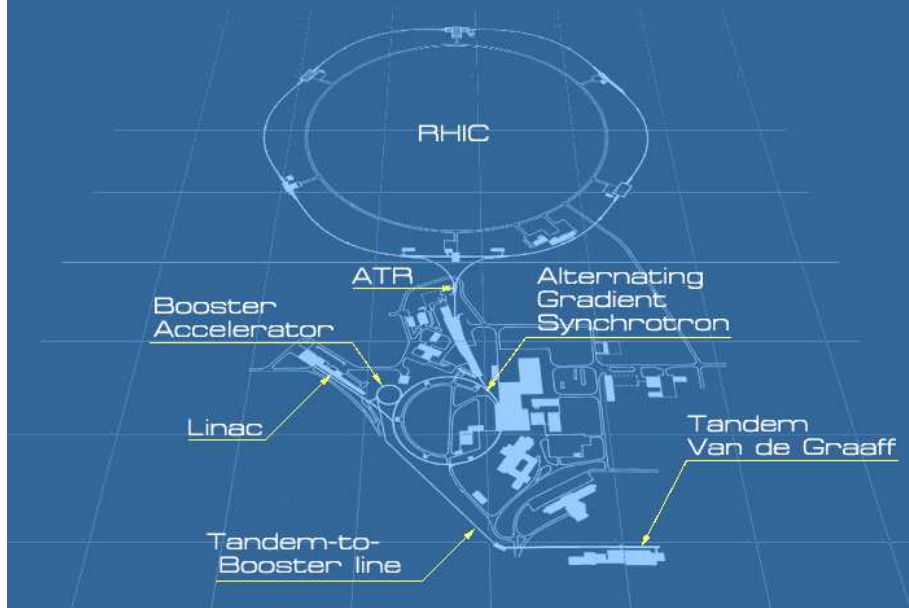


Figure 3.2: The RHIC Complex

AGS consists of 240 magnets. The field gradient of these magnets is alternated, hence the name. Once they are traveling at this ultra-relativistic speed, they are transferred to RHIC via the AGS-To-RHIC (ATR) transfer line. Once they reach the end of the ATR transfer line, the ions are divided into 2 bunches, traveling either clockwise or counterclockwise in the so-called *blue* and *yellow* lines.

RHIC ring has a circumference of 3.8 kilometers in circumference. The design luminosity of RHIC is  $2 \times 10^{26} \text{ cm}^{-2} \text{ s}^{-1}$ . However in the run of 2000, only about 10% of the design luminosity could be achieved. The luminosity, which is the number of ions passing per unit area per unit time, can be calculated for the two colliding beams containing  $n_1$  and  $n_2$  ions per bunches as:

$$L = f \frac{n_1 n_2}{4\pi\sigma_x\sigma_y} \quad (3.1)$$

where  $f$  is the beam frequency, and  $\sigma_x$  and  $\sigma_y$  are the widths of the beams perpendicular to the beam axis. the number of ions per bunch is about  $10^9$  for Au-Au and  $10^{11}$  for p-p. The event rate  $R$  in a collider is related to the luminosity  $L$  and the

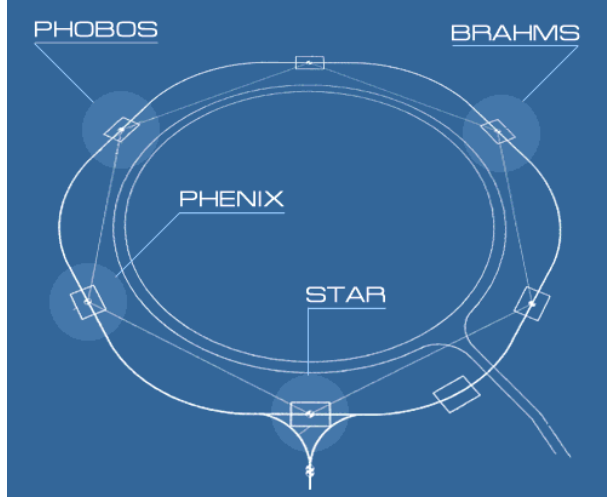


Figure 3.3: RHIC Beam Interaction Points. The Locations of the four experiments are shown.

interaction cross-section by:

$$R = L\sigma_{int} \quad (3.2)$$

There are six interaction points where RHIC can collide beams. If RHIC's ring is thought of as a clock face, the four current experiments are at 6 o'clock (STAR), 8 o'clock (PHENIX), 10 o'clock (PHOBOS) and 2 o'clock (BRAHMS)(Fig. 3.3). There are two additional intersection points at 12 and 4 o'clock where future experiments may be placed.

One of RHIC's two smaller detectors is the Broad Range Hadron Magnetic Spectrometer, or BRAHMS. It measures particles emerging from a specific set of angles during each collision. The momentum, energy and other characteristics of the particles are measured very precisely. It is capability of measuring inclusive momentum spectra of identified charged hadrons over a wide range in rapidity and transverse momentum.

PHOBOS, the other of the two small experiments, looks for rare but interesting events among a large number of collisions. For each collision, PHOBOS gives a global picture of the consequences of the collision and detailed information about a small

subset of the nuclear fragments ejected from the fireball.

STAR, or Solenoidal Tracker At RHIC, is one of the two large experiments. It specializes in tracking the thousands of particles produced by each ion collision at RHIC. STAR physics program concentrates on searching for the signatures of quark-gluon plasma. It is also used to investigate the behavior of matter at high energy densities by making measurements over a large area.

PHENIX, the Pioneering High Energy Nuclear Interaction Experiment, is the other large experiment. PHENIX is a multi purpose detector in the sense that it can measure hadrons, electrons muons and photons. It has an excellent particle identification capability. Our analysis is using  $y$ =the PHENIX detector. In the subsequent sections we describe the PHENIX detector and its various detector components in details.

### 3.3 PHENIX Experiment at RHIC

The primary goals of the heavy-ion program of the PHENIX collaboration are the detection of the quark-gluon plasma and the subsequent characterization of its physical properties. To address these aims, PHENIX will pursue a wide range of high-energy heavy-ion physics topics. The breadth of the physics program represents the expectation that it will require the synthesis of a number of measurements to investigate the physics of the quark-gluon plasma. The broad physics agenda of the collaboration is also reflected in the design of the PHENIX detector itself, which is capable of measuring hadrons, leptons and photons with excellent momentum and energy resolution. PHENIX has chosen to instrument a selective acceptance with multiple detector technologies to provide very discriminating particle identification abilities. Additionally, PHENIX will take advantage of RHIC's capability to collide beams of polarized protons with a vigorous spin physics program.

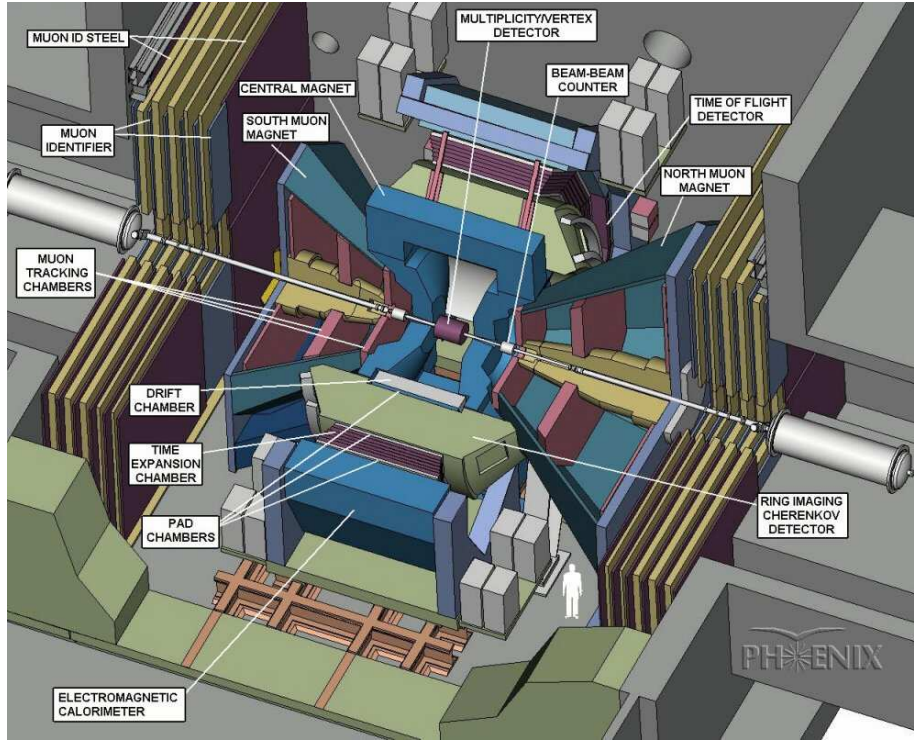


Figure 3.4: Schematic of the PHENIX Experiment at RHIC

### 3.4 A Brief Description of the Detector Components

PHENIX detector consists of a large acceptance charged particle detector and four spectrometer arms - a pair of spectrometers measuring electrons, photons and hadrons at mid rapidity and a pair of muon spectrometers at forward rapidity. PHENIX consists of eleven different detector subsystems. Fig. 3.4 shows the schematic drawing of PHENIX detector. Two gold beams coming from the left and right will be made to collide at the center of the detector. At the center there is the central charged particle detector. At the top and the bottom of the figure there are the two *central arms*, called east arm and west arm, a spectrometers systems for electrons, photons and hadrons. There are two *muon arms* at the north and south side. Fig. 3.5 shows the PHENIX from beam line and Fig. 3.6 shows the PHENIX detector from side.

## PHENIX Detector - First Year Physics Run

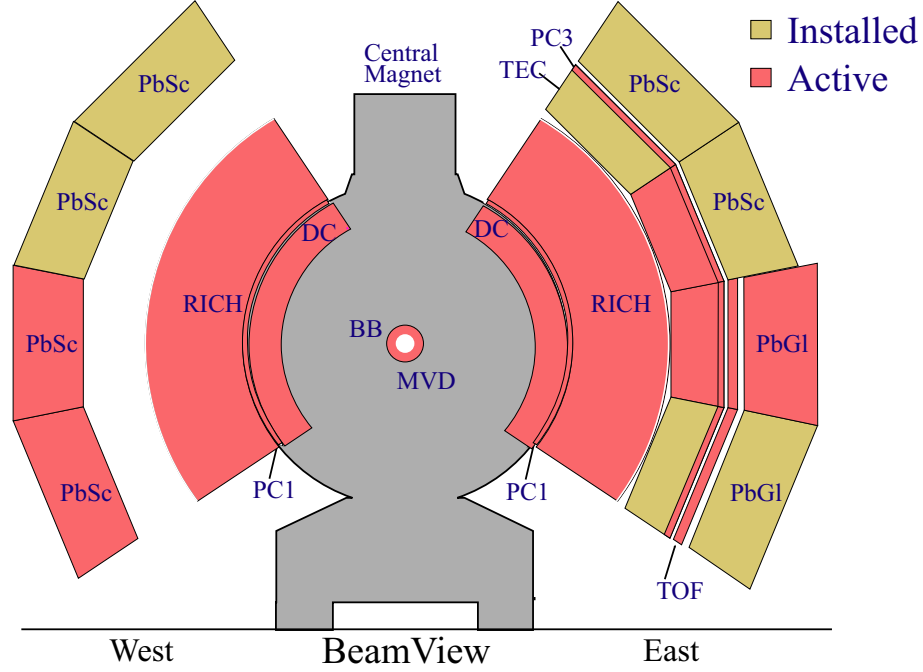


Figure 3.5: PHENIX View from Beam line.

The design philosophy of PHENIX is to identify and trigger on exclusive leptons, photons and high  $p_T$  hadrons with excellent momentum and energy resolution. The detector system can be classified into three categories:

- **Inner Detectors**

- **Silicon Multiplicity and Vertex Detector (MVD)** of strip and pad arranged around the interaction region
- **Beam Beam Counter (BBC)** on the either side of vertex

- **Central Arm Detectors**

- **Central Magnet**. The North and South poles of the Central Magnet are positioned on the collision axis at 0.45m and -0.45m respectively.

## PHENIX Detector - First Year Physics Run

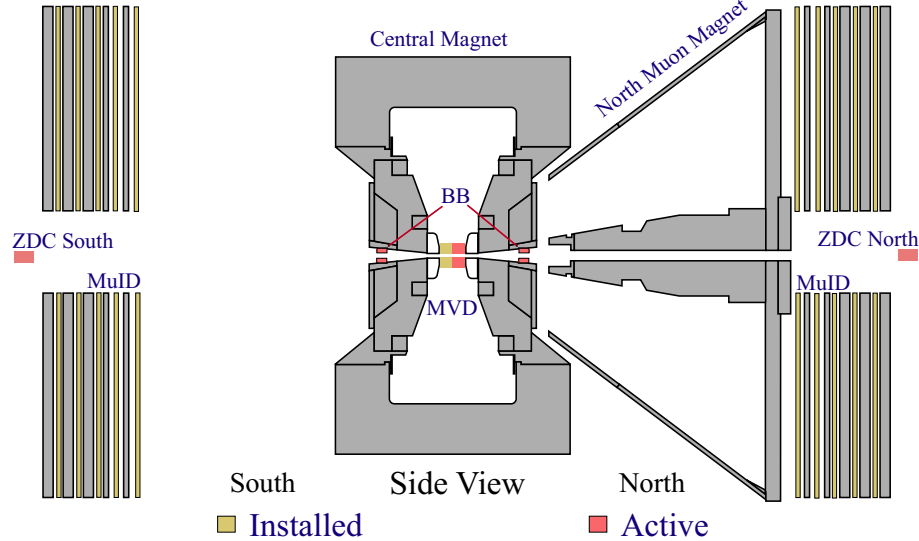


Figure 3.6: PHENIX Side View

- An intermediate tracker made of **Drift Chamber DC**) and **Pad Chambers (PC1)**
- A ring imaging **Cerenkov Detector(RICH)**
- Outer Tracker composed of a pad chambers **PC3** and **Time Expansion Chamber (TEC)** in the east arm and two pad chambers **PC2** and **PC3** in the west arm.
- A **Time of Flight (TOF)** scintillators in the east arm.
- An **Electromagnetic Calorimeter (EMCal)** . One half of the east arm is equipped with Lead Glass type (**PbGl**) and the rest half of east arm and west arm is equipped with lead scintillators (**PbSc**)

### • Muon Arms

- Three tracking stations (**muTr** )
- A muon Identifier (**muID** )

Element	$\theta$ (deg.)	$\eta$	$\phi$ (deg.)	$\Delta\Omega$ (sr)
Inner Detectors	2–178	–4.0–4.0	0–360	$\sim 4\pi$
Central Arms	70–110	–0.35–0.35	$\pm(22.5–112.5)$	1.07
Muon Arm	10–35	1.15–2.44	0–360	1.17

Table 3.1: Angular and Pseudorapidity Coverage of PHENIX

The geometrical coverage of the detectors can be summarized in the Table 3.1:

The detectors are thus also classified, according to their usage, as:

- Vertex Finding : BBC, MVD
- Tracking : DCH, PC1, PC2, PC2, TEC
- Particle Identification : TOF, RICH, EMCAL

In the following section we will describe the detector systems in brief.

## 3.5 Inner Detectors

The inner detector system in PHENIX comprises of a set of silicon strips and pad detectors and a pair of beam counters. The detectors sit very close to the collision point. Their primary purpose are to characterize events, provide centrality trigger, measure collision vertex points along the beam and time of flight start. MVD also has the capability of measuring charged particle distribution. In the Table 3.2[24] we can summarize the capabilities of the Inner detector system:

### 3.5.1 Beam Beam Counter (BBC)

The Beam-Beam Counter provides information for triggering on beam-beam collisions and obtains a rough collision vertex position along the beam axis. It also helps find correlation between tracks in various detectors and the time origin of the collisions.

Subsystem/ Coverage	TOF Start	Vertex	Multipl.	Central Trigger	$dN/d\eta$	Fluctuations
Beam-beam $ \eta  = 3.1 - 4$	$\sigma < 100$ ps each tube	$\sigma \approx 1-2$ cm For LVL-1 Trigger				
Si Strips $ \eta  \leq 2.5$		$\sigma < 2$ mm	yes	For LVL-1 Trigger	yes	$dN/d\eta$
Si Pads $ \eta  = 1.8 - 2.65$			yes	For LVL-1 Trigger	yes	$dN/d\eta$ $dN/d\phi$

Table 3.2: Capabilities of Inner Detectors

The Beam-Beam Counter elements were designed to have an intrinsic timing resolution of 50ps after slewing correction for a single MIP. Since a collision at RHIC is capable of producing a large number of tracks, the counter elements are designed to have enough dynamic range to accept multiple hits, which, may be up to 10 in gold-gold collisions. Also, the Beam-Beam Counter is close to the magnets, and therefore the elements are designed not to be perturbed by the magnetic field.

The Beam-Beam Counter consists of two arrays of counter elements, one each placed upstream and downstream of the beam crossing point.

The elements are closely packed into a ring around the beam pipe. The minimum inner bore radius and the maximum outer radius are designed to be 50 mm and 150 mm, respectively.

The Beam-Beam Counter provides the z-vertex position and Time zero. The cartoon in Fig. 3.8 describes roughly how the collision start time and vertex measurement is done with BBC. The interaction position along the beam axis will be calculated from individual time measurements of fast leading particles hitting BB on the both sides of the interaction point. With an intrinsic timing resolution of 70 ps, BB determines the interaction position with a precision of approximately 2 cm. In addition to the prompt particles, there are also slower particles entering the BB

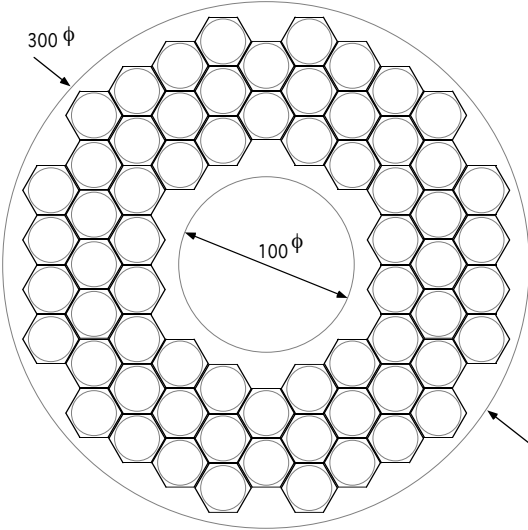


Figure 3.7: Front view of the beam-beam counter array.

elements. These are not useful for the precise interaction time as their velocities and flight paths are not known, and they represent a background. Another background source is the thermal noise in the BB elements. To reject background signals which fire discriminators randomly or in a period immediately after the arrival of the prompt particles, we derive the interaction time only from particles arriving within 10–20 ps of the beam crossing time.

The interaction position along the beam axis is calculated from individual time measurements of fast leading particles hitting BBC on the both sides of the interaction point. With an intrinsic timing resolution of 70 ps, BBC determines the interaction position with a precision of approximately 2 cm.

### 3.5.2 Multiplicity & Vertex Detector (MVD)

The multiplicity and vertex detector (MVD), which is placed just outside the beam pipe, provides centrality trigger and more accurate vertex information. The MVD is comprised of two parts: two end caps and two concentric central barrel covered with silicon pads and strips. Vertex finding can be done with good efficiency using the

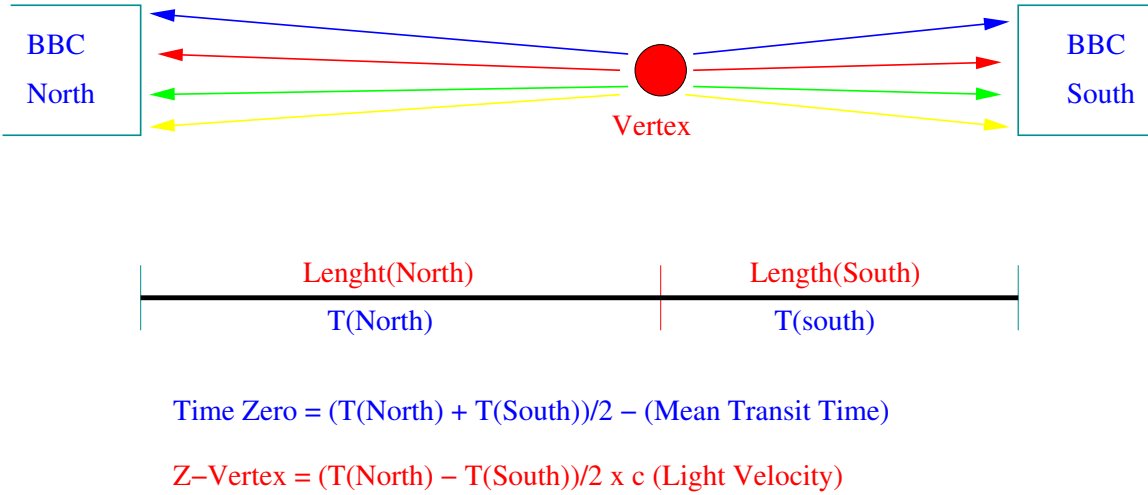


Figure 3.8: BBC Zero Time and Z-vertex Measurement

hits from the central barrels for z-position up to  $\pm 40$  cm with a position resolution  $\pm 2\text{mm}$ . The disk shaped end caps, located at z-positions of  $\pm 35$  cm and are composed of silicon pads. Analog sums of the signal from the end caps and also from the central barrel, allow formation of multiplicity triggers from different ranges of pseudorapidity.

We do not intend to describe MVD in detail here because the following chapter is dedicated for detailed description on MVD.

### 3.6 Zero Degree Calorimeter

The Zero Degree Calorimeter (ZDC) is a detector standard to all four experiments at RHIC. The ZDC measures the beam energy neutrons emitted in the breakup of the nuclear remnant that misses the interaction zone. The calorimeters are also the principle device to monitor the beam luminosity during the run and serves as an event trigger for all four RHIC experiments.

In Heavy Ion collisions, the collision impact parameter is, in principle, a measurable and useful quantity. In the search for new states of matter under conditions of extreme density and temperature it will be useful to characterize collisions using

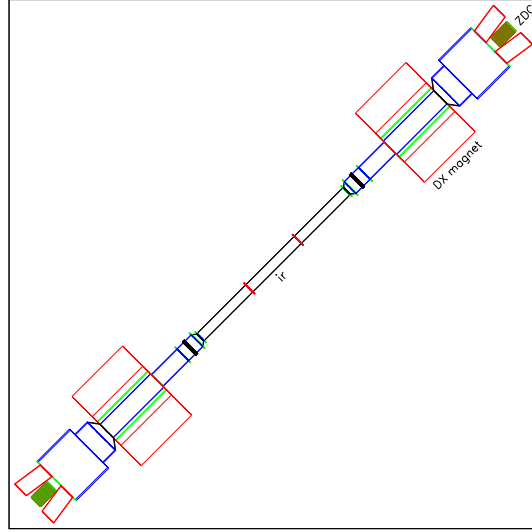


Figure 3.9: Beam line geometry around the interaction regions showing the beam splitting dipoles and the zdc detector placement.

global measurements that don't bias the signal of interest. In order to compare results from different experiments measurements of global event properties are made using common instrumentation. And this common instrument is the ZDC.

In PHENIX, the two ZDCs are located at 8 m up and downstream from the collision vertex. Each of them covers a polar angle of  $\theta < 4$  mrad. Fig. 3.9 shows the beam geometry and the detector location.

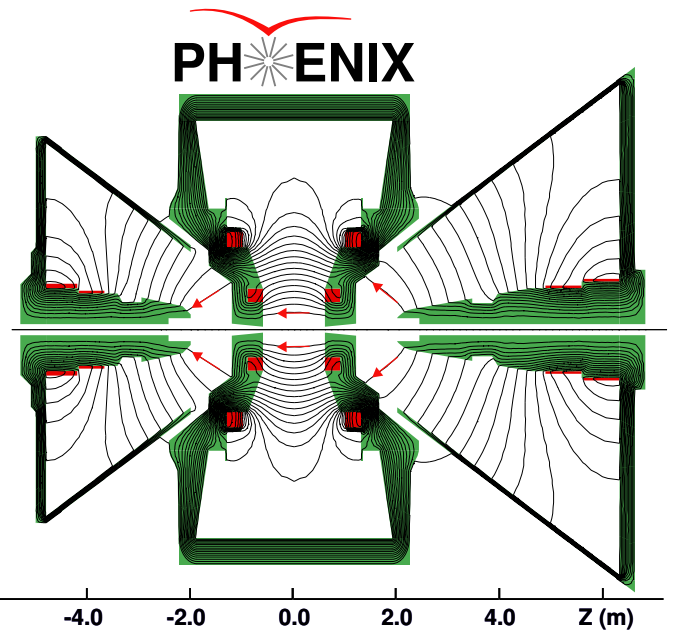
The vertex position measurement procedure is similar to that described for BBC (see Fig. 3.8).

### 3.7 Central Arm Detectors

The central arm detectors have the capability of particle tracking and particle identification, charged particle momentum measurement and electron and photon energy measurement. The central arm spans  $\pm 0.35$  units in pseudorapidity and covers about 90 degrees in azimuth on east and west of the interaction point. The Table 3.3 summarizes the central arm detector[24]

Element	Radial Space(mm)	Channel Count	Function
DC	2000–2475	10,240	Tracking and pattern recognition primarily in $r$ - $\phi$ , momentum measurement.
PC1	2475–2525	15,000	Pattern recognition and tracking, primarily in $z$ .
RICH	2575–4000	6400	Electron identification up to $p \approx 3$ GeV/c.
PC2	4050–4100	16,000	Pattern recognition and tracking, primarily in $z$ .
TEC	4100–4800	29,000	Pattern recognition, tracking in $r$ - $\phi$ , and electron identification by $dE/dx$ up to $p \approx 2$ GeV/c.
PC3	4800–4850	16,000	Pattern recognition and tracking, primarily in $z$ .
TOF	4900–5050	1000	Hadron identification, $\pi$ / $K$ up to 2.4 GeV/c.
EMCal	5100–6000	28,000	$e/\gamma$ measurements by energy, shape, and timing. Electron identification below 350 MeV/c by time-of-flight and above 1 GeV/c by $E$ - $p$ matching. K/e separation up to 1 GeV/c by time-of-flight for $dE/dx$ .

Table 3.3: Central Arm Detectors



Magnetic field lines for the two Central Magnet coils in combined (++) mode

Figure 3.10: PHENIX Central Magnet Field Lines

### 3.7.1 Central Magnet

In the central arm of PHENIX a magnet is employed to focus the tracks into the PHENIX central arm acceptance. This Central Magnet is an axial field magnet energized by two pairs of concentric coils, which can be run separately, together, or in opposition. In Fig. 3.10 is shown the field lines when both coils are turned on. The magnet is 9 meters tall and has a rapidity coverage of  $\pm 0.35$  units. The magnet provides a field integral ( $\int \vec{B} \cdot d\vec{l}$ ) of 0.78 Tesla-meters at 90 degrees in polar angle from the beam axis. Due to this, PHENIX could achieve an excellent particle resolution. The measured single particle momentum resolution at the Drift Chambers is 0.5% between 200 MeV/c and 1 GeV/c. In order to minimize the distortion of the particle tracks, the magnet is designed to achieve an integral field of 100 gauss-meters from a radius of 2.4 meters to 4.0 meters. The fields near the EMCal phototubes, which sit farthest from the beam pipe, the field is less than 10 gauss. The pole faces of

the Central Magnet serves as the primary absorber of hadrons for the Muon arm spectrometers.

### 3.7.2 Tracking and Momentum Measurements

As mentioned earlier, a near head-on collisions of Au-Au at RHIC is expected to produce more than 500 charged particles per unit pseudorapidity at mid rapidity in a single collision. The PHENIX tracking system, therefore, operates in a high track density environment. The task of the tracking system is to locate all interested charged tracks in the PHENIX acceptance, measure the momentum of the tracks and help identify which of the tracks are electrons.

The PHENIX tracking system consists of a Low mass, multiwire focusing drift chambers (DC), Three pad chambers (PC) in the west arm and two pad chambers in the east arm and a four-layer time expansion chamber (TEC) in the east arm. The Drift Chambers provide high resolution  $p_T$  measurements. Pad Chambers are used for a three-dimensional position measurement to aid in pattern recognition and to determine  $p_z/p_T$ . The Time Expansion Chamber assists in the pattern recognition and provides  $e/\pi$  separation from energy loss ( $dE/dx$ ) information.

#### Drift Chambers

The drift chambers are the first tracking detectors that charged particles encounter as they traverse through the central arms. As the charged tracks pass through the gas, they ionizes the gas. The drift chambers provide the spatial information of the charged tracks by measuring the drift time of those electrons.

The drift chamber is located between  $r = 2.02$  m and  $r = 2.46$  m in the PHENIX central arm. It covers  $\pm 0.35$  units in pseudorapidity. The chambers are 1.8 meters in length along the beam axis. The drift chambers are made of independent and identical  $\phi$  sections called *supermodules* which in turn are composed of drift cells. The

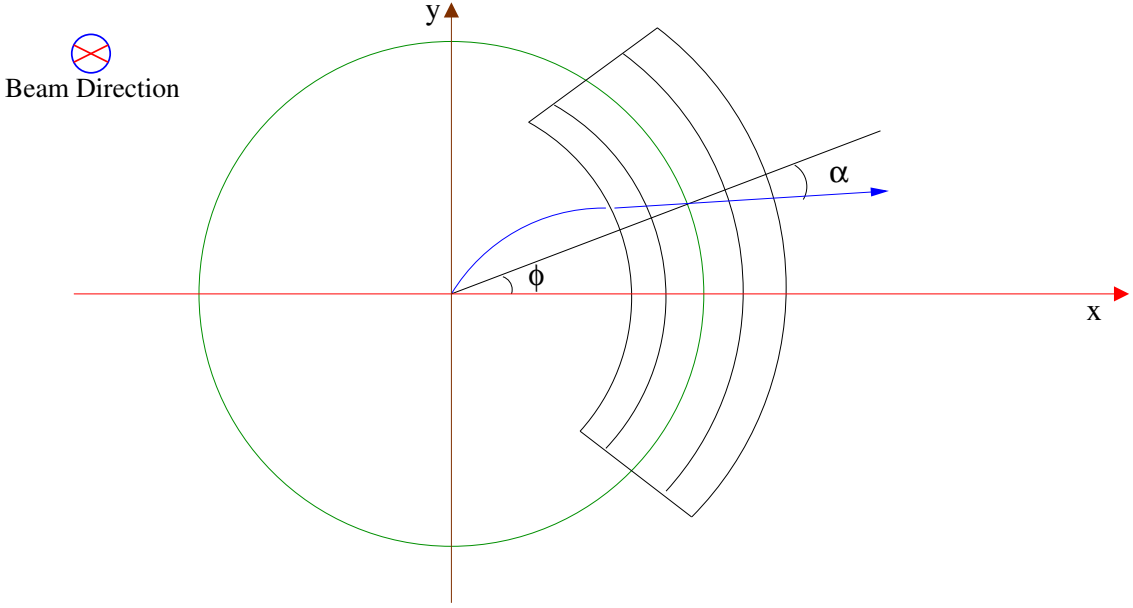


Figure 3.11: Particle track in the Drift Chambers and the Hough transform parameters : azimuthal angle  $\phi$  and the inclination angle  $\alpha$ .

chambers are arranged into 160 drift cells . A drift cell contains 6 types of wires namely: X1,U1,V1,X2,U2,V2 and covers  $1^\circ$  in azimuth and 6 mm in radial.

Track reconstruction within the drift chamber is performed using a combinatorial Hough transform (CHT) technique. In this technique, the drift chamber hits are mapped into a space defined by the azimuthal angle  $\phi$  at the intersection of the track with a reference radius  $R$ , and the track's angular deflection from a straight line,  $\alpha$  as schematically shown in Figure 3.11. If a track hits  $n$  points in the drift chambers, the signal height is  $n(n - 1)$ . A three dimensional plot is made for this Hough amplitude and the  $\phi$  and  $\alpha$  pairs. The peak of the plot corresponds to the track. The position of the peak in the Hough space is the direction of the track. In the drift chambers the single wire spatial resolution better than 0.15 mm, single wire two track separation better than 1.5 mm, spatial resolution in  $z$  direction better than 2 mm and the single wire efficiency better than 99%. The drift chamber is designed to provide a high-resolution transverse momentum measurement of  $\sigma_p/p = 0.5\%$  at 0.5 GeV/c. The

Year-1 drift chamber resolution is  $\sigma_p/p = 1.0\% \pm 3.5\%p$  [25, 26].

## Pad Chambers

The primary functions of the pad chambers (PC) are to perform measurements of non-projective three dimensional spatial points to be used for both momentum determination and pattern recognition. The main functions of the PHENIX pad chambers are:

1. To provide track information to reduce track-matching ambiguities.
2. To provide azimuthal tracking information.
3. To help separate neutral EMCAL showers from charged tracks.
4. To help veto converted photons.

There are three pad chambers (PC1, PC2, PC3) in the PHENIX detector system. PC1 is placed immediately behind the DC and in front of the RICH in both arms. The PC2 in the west arm is behind the RICH, and PC3 in both arms are just in front of the EMCAL.

Pad Chambers are composed of three layers of pixel detectors. A single "PIXEL" is small copper rectangle that is connected to 8 other small copper rectangles. All 9 pixels are read out by a single discriminator. The object which is composed of 9 connected PIXELs is called a "PAD". Whenever a charged track passes through the pad chamber, there should be three neighboring PADs which all receive an induced signal large enough to trigger their three separate discriminators. The 9-fold ambiguity of which PIXEL is hit is resolved (usually) by looking at which set of three PADs have hits. The structure of three neighboring PIXELs that gets uniquely identified as the location of the track is called a "CELL". In Year-1, three Pad Chambers were instrumented in PHENIX : PC1 and PC3 in the east arm and a PC1 in the west arm. For detailed information on the pad chambers see reference[27].

### Time Expansion Chamber

The time expansion chamber (TEC) is mounted on the east arm in PHENIX. It performs both particle identification and tracking functions. It measures charged particle ionization energy losses ( $dE/dx$ ). This allows separating of electrons from pion over a momentum range 0.25 -3 GeV. The TEC is planning to upgrade to a Transition Radiation Detector (TRD). Once upgraded, it can separate  $e/\pi$  over a momentum range 0.25- 50 GeV via transition X- radiation detection. TEC tracks all charged particles and produces direction vectors that match tracking information from the Drift and Pad Chambers to complete track determination in the PHENIX. It has a single point track resolution of  $250 \mu m$  and two track separation of 2 mm. It also Measuring the transverse momentum of charged tracks.

The wires in the time expansion chambers are arranged in 6 planes and 4 sectors. In the year-1 only 4 planes were instrumented electronically. It covers  $90^\circ$  of the PHENIX azimuthal angle  $\phi$  and 0.35 units of pseudorapidity  $\eta$  (approximately  $40^\circ$  of the polar angle  $\theta$ ). the detectors location from the collision vertex is approximately  $R = 410- 457$  cm. It consists of 64,080 wires and 20,480 readout channels.

The tracking is done using the same principle as in the drift chambers using the Hough transformations (Fig. 3.11). The transverse momentum is related to the inclination angle  $\alpha$  by the relation[28]

$$p_T = \frac{1}{21.5\alpha} \quad (3.3)$$

### 3.7.3 Particle Identification

PHENIX physics program intends to study hadrons, electrons and photons. PHENIX central arm is equipped with various detectors those are capable for these jobs. The Ring Imaging Cherenkov Counters (RICH) are used for electron identification, in conjunction with the Electromagnetic Calorimeter. The High resolution Time of

Flight (TOF) has excellent particle identification capability. Also the EMCal is also used for particle identification.

### Time of Flight

Studies of hadrons provide important information about the collision environment, which is necessary to understand any of the QGP signal. The knowledge of species abundance, net baryon number, and the development of collisions in space and time are crucial to interpret any of the physics observables. Hadronic signatures have been proposed for the observation of the QGP formation and for the chiral symmetry restoration. Together with leptonic signatures, these signatures provide additional proof for the QGP formation.

The time-of-flight (TOF) system is used for hadron identification. Also it is used in conjunction with the RICH to identify electrons. The time of flight detector is located 5.0 m away from the vertex covering  $40^\circ$  in  $\theta$  and  $30^\circ$  in  $\phi$ . The geometrical coverage of the TOF system is 280 cm in the  $r\phi$  direction and 390 cm along the  $z$  direction.

In the PHENIX central arm two sectors in the TOF detector are mounted. There are 10 panels in the detector, 8 on the top sector and the bottom sector has 2 panels. The panels have a total of 960 plastic scintillation counters and 1920 channels of Photo multiplier tubes (PMTs), collectively called slats. Each slat has PMTs at end, a light guide, and support. Each slat is oriented along the  $r\phi$  direction, and provides time and longitudinal position information for particles that hit the slat.

The design timing resolution of TOF is 85 ps. In year-1, a resolution of about 120 ps was achieved. A particle identification plot from TOF is shown in Fig. 3.12

### Ring Imaging Cherenkov Counters

The Ring Imaging Cherenkov (RICH) detector is used for the identification of electrons. The detector is located outside of the PHENIX central magnet, having inner

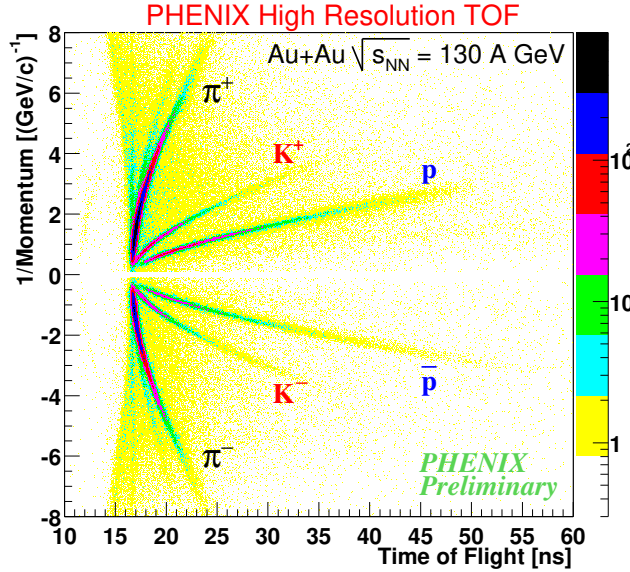


Figure 3.12: Particle Identification in PHENIX Time-of-flight. The data used is from year-1 at  $\sqrt{s} = 130$  GeV. Clear bands of particles are seen, which is an evidence of the excellent PID capability

and outer radii of  $r = 2.6$  m and  $r = 4.0$  m as measured from the collision point. The entire region is filled with a Cherenkov radiator gas of index of refraction  $n$  ( $\text{C}_2\text{H}_6$ ,  $n \sim 1.0008$  or  $\text{CH}_4$ ,  $n \sim 1.00044$ ). RICH measure the Cherenkov radiation emitted by charged particles move through gas at a speed larger than  $c/n$ , where  $c$  is the speed of light. The radiation is emitted along a cone, where the opening angle of the cone with respect to the apex is  $\theta_c = \cos^{-1}(1/n\beta)$ , where  $\beta = v/c$ . The momentum beyond which a charged pion will radiate is about  $3.5$  GeV/c in ethane, and about  $4.7$  GeV/c in methane. The Cherenkov photons generated by electrons, positrons, and high momentum hadrons are reflected by spherical mirrors placed within the radiator volume, and the photons are focused onto photon detectors placed just behind the PHENIX central magnet.

## Electromagnetic Calorimeter

The Electromagnetic Calorimeter (EMCal) in PHENIX is used primarily to electron and photon identification and to measure their position and energy. Comparison of the momentum of charged particles, measured in the drift chambers or in the time expansion chambers, with the energy response of the calorimeter provides a tool for electron identification. The timing resolution is about 600 ps. This precision of measurement of arrival time of a track on the EMCal enables additional particle identification for both neutral and charged particles by combining calorimeter time with amplitude information. In year-1 a  $K/\pi$  separation up to 1.4 GeV/c in the transverse momentum was achieved.

The EMCal has a total of 8 sectors, 4 in each arm. There are two types of Electromagnetic Calorimeters in PHENIX: lead scintillators (6 sectors of PbSc) and lead glass (2 sectors of PbGl). In year-1 two sectors of PbSc in the west arm and one sector of PbGl in the east arm were mounted.

## 3.8 Muon Spectrometers

The PHENIX muon arm supplements the PHENIX central arm acceptance for lepton pairs at rapidity away from  $y = 0$ . The main purpose of the muon detector is to detect muon pairs originating from vector meson decay or virtual photon production. The muon particle detector is comprised of interleaved layers of iron and Iarocci tubes. The particle identification is done based on the energy loss of the muon via radiation after it traverses each layer of iron. The muon arm was not instrumented in year-1.

## 3.9 Subsystems Used For This Analysis

The analysis on charged particle multiplicity requires a measurement of the number of tracks in the MVD. The Pseudorapidity measurement requires the vertex position

information. The MVD in year-1 did not have the capability of the vertex position measurement. Therefore the vertex information was obtained from the BBC. Also a centrality dependence of multiplicity was studied. The standard PHENIX procedure for the centrality utilizes the energy information from the Zero Degree Calorimeter (ZDC) and the analog charge sum in the BBC.

# Chapter 4

## MVD Overview

### 4.1 Introduction

When two beams of RHIC collide inside PHENIX, the first detector to look into the collision will be the Multiplicity and Vertex Detector (MVD). MVD is an extremely close detector subsystem composed of thousands of detector channels. A near head-on collisions of Au-Au at RHIC is expected to produce from 500 to 1500 charged particles per unit pseudorapidity at mid rapidity in a single collision. MVD is well equipped with about 35000 electronics channels to record these events. As the name implies, the task of MVD is to count thousands of charged particles produced in the collision, determine the event vertex and provide LVL-1 trigger. In PHENIX various signatures of Quark-Gluon Plasma will be studied. They all will be “simultaneously” studied as a function of the energy density ( $\epsilon$ ). The determination of the energy density of the system formed after the heavy-ion collision is the core of the PHENIX physics program. And MVD is the detector that measures the charged particle multiplicity ( $dN/d\eta$ ), which, then, can be related to the energy density.

The MVD has the largest rapidity coverage of any of the subsystem in PHENIX at  $-2.5 \leq \eta \leq 2.5$ . The detector has full azimuthal coverage with good granularity and is capable of reconstructing the collision vertex to better than 2mm[24].

## 4.2 Overview of Silicon Detector

MVD employs silicon detectors for particle tracking and trace reconstruction. Silicon detectors are widely used primarily because of the large band gap and the requirement of low average energy for electron-hole pair creation[29].

When a particle hits a semiconductor, it loses its energy in the material. In the process it generates a number of electron-hole pair in the semiconductor material that is equal to the energy lost divided by the average energy required to produce a single pair. A particle that possesses a minimum ionizing energy to produce an electron-hole pair in the semiconductor is called *minimum ionizing particle* or MIP. The generated carriers can be collected and then give rise to a pulse whose amplitude is directly proportional to the energy deposited by the particle. For this purpose a sensitive region depleted from the free carriers and an electric field able to separate the created carriers and guide them toward the electrodes must exist in the semiconductor. Let us look at the Fig.(4.1) to understand how a silicon detector works.

In order for the detector to work, the detector needs to be fully depleted,*i.e.* we need to give enough reverse bias voltage so that no free carriers are available. Why do we need that? In fully depleted conditions, if a particle goes through the detector, it will make electron-hole pairs. They are attracted to the opposite terminals, get collected and we get a signal.

The thickness  $W$  of the depletion region as a function of the applied voltage  $V$  in the semiconductor containing concentrations of ionizing dopant  $N_a$ (acceptors) and  $N_d$ (donors) is equal to:

$$W = \sqrt{\frac{2\epsilon_0\epsilon_r(V + V_0)}{e|N_d - N_a|}}, \quad (4.1)$$

where  $\epsilon_r$  and  $\epsilon_0$  are dielectric constants of the material and the vacuum, respectively, and  $e$  is the electron charge. The diffusion potential  $V_0$  depends on the diode properties and is no more than a fraction of the band gap. It is about 0.5-0.7 volts for

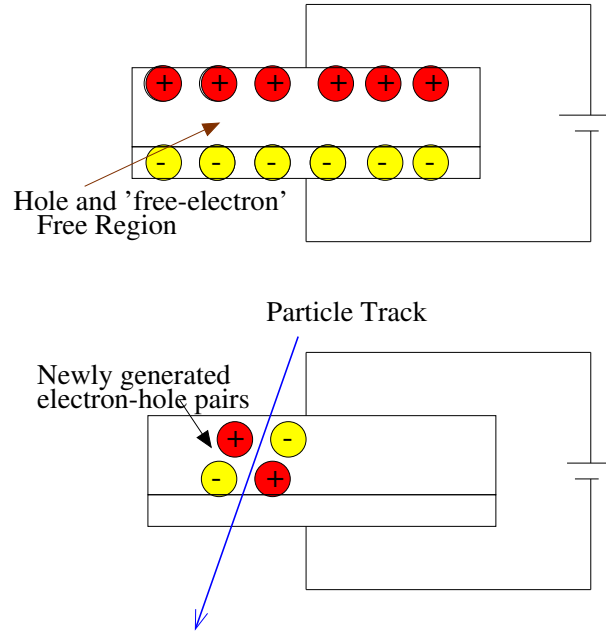


Figure 4.1: Silicon Detector : Working Principle

silicon. Full depletion of a detector of thickness  $d$  is obtained for the depletion voltage  $V_d$  :

$$V_d = \frac{e|N_d - N_a|d^2}{2\epsilon_0\epsilon_r}. \quad (4.2)$$

The evolution of the electric field  $E(x)$  from the position  $x$  of the stoichiometric junction in a planar p-n diode is given by

$$E(x) = \frac{V}{d} - \frac{e}{\epsilon_0\epsilon_r}|N_d - N_a| \left( x - \frac{d}{2} \right) \quad (4.3)$$

Eq.(4.1) can be alternately written as:

$$W = \sqrt{2\rho\mu\epsilon(V + V_0)}, \quad (4.4)$$

where

$$\epsilon = 11.9\epsilon_0 \simeq 1\text{pF/cm}$$

$$\rho = \text{resistivity} \sim 1 - 10\text{k}\Omega\text{.cm}$$

$$\mu = \text{charge carrier mobility}$$

$$\begin{aligned}
&= 1350 \text{cm}^2 \text{V}^{-1} \text{s}^{-1} \text{ for electrons (n - type material)} \\
&= 450 \text{cm}^2 \text{V}^{-1} \text{s}^{-1} \text{ for holes (p - type material)}
\end{aligned}$$

or

$$W = 0.5 |\mu m / \sqrt{\Omega - cm \cdot V}| \times \sqrt{\rho(V + V_0)} \text{ (n - type material)} \quad (4.5)$$

$$W = 0.3 |\mu m / \sqrt{\Omega - cm \cdot V}| \times \sqrt{\rho(V + V_0)} \text{ (p - type material)} \quad (4.6)$$

The corresponding capacitance per unit area is

$$C = \frac{\epsilon}{W} \simeq \frac{1}{W} [\text{pF/cm}] \quad (4.7)$$

The particle energy required to create an electron-hole pair is about 3.6 eV. For minimum ionizing particles, the most probable charge deposition in a  $300\mu\text{m}$  silicon detector is about 3.3 fC (22000 electrons)

When an electric charge produced in the depletion region by the ionizing particle moves toward the electrodes, it induces on this electrode a current pulse  $I(t)$  and a charge pulse  $Q(t)$  which depend on the depletion region thickness and on the location on the primary interaction. In a perfect detector with uniform electric field full collection occurs within a time delay directly related to the carriers velocity and range. Therefore, for a fast detector response, a high electric field has to be applied to high mobility ( $\mu$ ) carriers so that electron and hole velocities  $v (= \mu E(x))$  reach the thermal velocity saturation value (close to  $10^7$  cm/s). Good detector operation cannot be obtained unless full collections of carriers have been completed. Hence, not only a high mobility is needed, but also in addition the carrier's lifetime must be long enough so that a negligible fraction of them has a chance to be lost before reaching the electrodes.

### 4.3 MVD Construction

The purposes of the Multiplicity and Vertex Detector, which is composed of silicon strips, is designed to measure the number of charged particles per unit pseudo-rapidity ( $dN/d\eta$ ) and their multiplicity in addition to finding the vertex. In order to cover the central rapidity region, the  $dN/d\eta$  measurement should cover  $\eta$  from -3 to +3. The total charged particle multiplicity must be available for the first level trigger. When the multiplicity is low, an accurate measurement requires a detector which covers a large fraction of the total solid angle. For central Au+Au collisions at RHIC the expected number of charged particles in the range  $-3 < \eta < 3$  is around 5000[30]. If the occupancy is to be kept to 10% or less, this implies that the detector will need at least 50K channels in each layer. Also the vertex detector must find the vertex. This should be done approximately (to within  $\simeq 1\text{cm}$ ) at the trigger level, with a more accurate determination ( $\simeq 1\text{mm}$ ) offline. Any vertex finding algorithm requires several charged particles in the detector, which is not a serious constraint for Au+Au collisions. However, in order to consistently find the vertex position for p+Au and p+p collisions, where the charged particle multiplicities can be much lower, a large fraction of the total solid angle must be covered.

MVD has silicon strip detectors arranged in two concentric barrels around the beam pipe in the center of PHENIX, and end caps consisting of a single layer of silicon pad detectors. Both pad and strip detectors are single sided and are read out with identical front-end electronics mounted on hybrid circuits. The total silicon channel count is 34816(256 channels per silicon detector). In Fig. 4.2 is shown an overview of the schematic of MVD. It shows the positions of barrels, pads and end caps. In Fig. 4.3 is shown the actual photograph of the MVD after some of the silicon strip detectors are installed.

The central barrels have radii of 5 and 7.5 cm and lengths of 64 cm. The schematic of the barrel is shown in Fig. 4.4. The single-event coverage about mid rapidity is

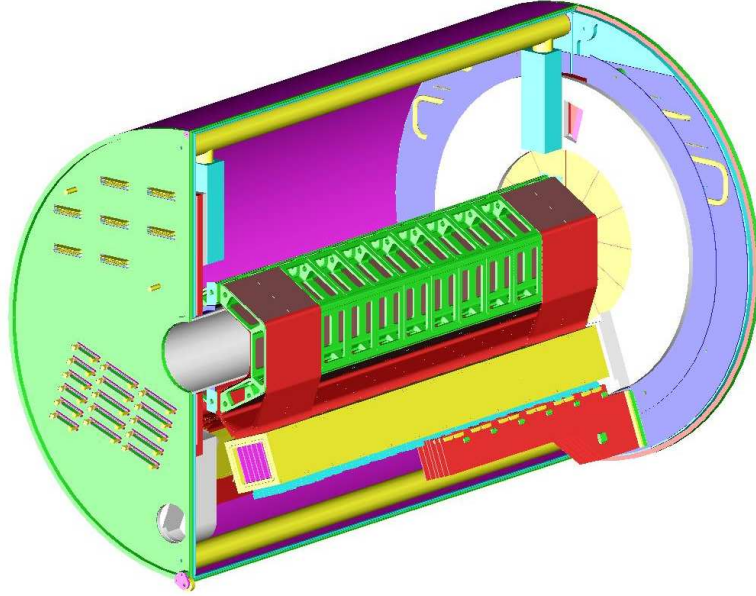


Figure 4.2: An Schematic view of the MVD

five units in  $\eta$  for the inner barrel layer and four unit for the outer barrel layer. So the  $\eta$  coverage for event -averaged quantities is extended due to the variation of the vertex position along the direction of colliding beams. The inner and outer barrels are composed of silicon strip detector wafers, with an area of  $5 \times 7 \text{ cm}^2$  and  $5 \times 7.5 \text{ cm}^2$ , respectively (the silicon strip detector wafers are sometimes called *panels*). The strip have a pitch of  $200 \text{ }\mu\text{m}$  and are mounted on a common support structure made of Rohacell foam. Both the barrels have 6 rows, each covering about  $60^{\text{deg}}$  in azimuth. The inner barrel is fully populated with 12 panels in each row. The two rows of the outer barrel is fully populated, and the rest of the 4 rows have 4 panels each (see Fig. 4.4). Each panel has 256 channels. Therefore the inner barrel has 18432 channels and the outer barrel has 10240 channels.

There are two disk shaped end caps at the two ends. The end caps are positioned in  $z$  at  $-35$  and  $+35 \text{ cm}$  and covers  $r = 5 \text{ cm}$  and  $r = 12 \text{ cm}$ . The schematic of the pad

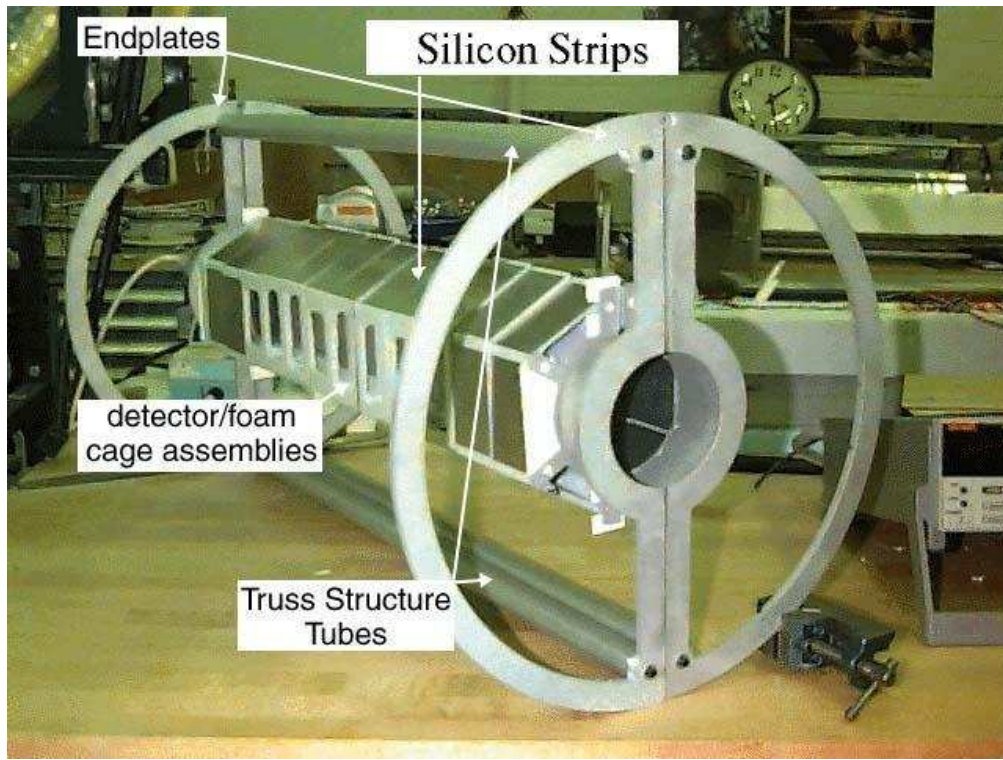


Figure 4.3: A Photograph of the MVD after some of the silicon strips were installed

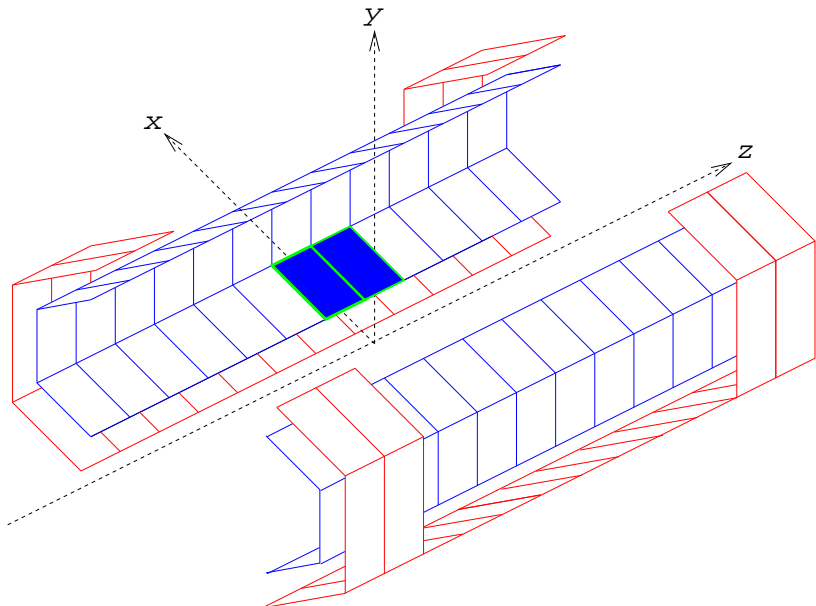


Figure 4.4: Schematic of the MVD barrel. The barrels are concentric, with radii 5cm and 7.5 cm respectively. Data from the blue strips were used in this analysis

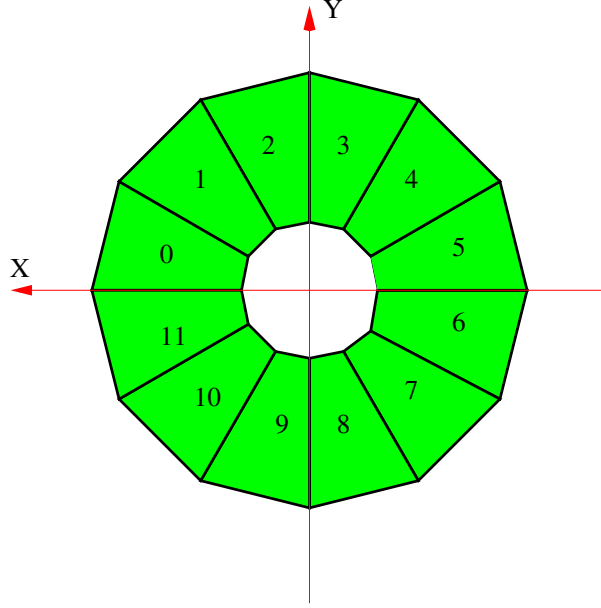


Figure 4.5: Schematic of the MVD End Caps.

is shown in Fig. 4.5. They comprise pads ranging in size from approximately  $2 \times 2$  to  $5 \times 5 \text{ mm}^2$ . There are 12 pads on each end. Each pad have 252 channels. Therefore the two end caps comprise of 6084 electronic channels

The pseudorapidity coverage is  $\pm 2.7$  for a single event occurring at  $z=0$ . The  $\eta$  segmentation is more than adequate for fluctuation studies, and pulse height analysis allows the unfolding of multiple hits in one pad. The azimuthal segmentation, along with the full azimuthal coverage, makes it possible to look for fluctuations in two dimensions. The highest channel occupancies for central events are 0.35-0.46 for  $dN_{ch}/d\eta = 1000$ . The vertex position can be located using hits in the barrel for  $z$  position between -40 and +40 cm, which cover  $2\sigma$  length of the interaction region. The multiplicity trigger is formed using the sum of silicon channels (both pads and strips) above a threshold corresponding to approximately 0.25-0.33 of a minimum ionizing particle. This threshold will be tuned to optimize the trigger performance.

The front-end electronics are optimized for minimum size, power dissipation and cost, while the design allows for unfolding of multiple particle hits in each silicon

Dimensions	75cm, 30cm radius
Active regions	inner barrel: $ z  < 32$ cm, $r = 5$ cm
	outer barrel: $ z  < 32$ cm, $r = 7.5$ cm
	end caps: $r = 5-12$ cm at $z = +35$ cm
Acceptance	full azimuthal coverage
	pseudorapidity coverage: $< 2.5$
Channels:	inner barrel: 18432
	outer barrel: 10240
	pads : 6048
	total: 34816
Weight:	11kg, 28lbs
Radiation length:	<1% in central arms acceptance

Table 4.1: KEY MVD parameters.

pixel. The dynamic range is 8 MIPs, and the signal to noise better than 10:1 for a single MIP. the shaping time of the preamplifier is 50-60  $ns$ , limited by the bunch crossing time to avoid pileup in p+p collisions and allow use of the silicon in the LVL-1 trigger. Although the multiplicity in a single Au+Au collision is very high, the expected luminosity at RHIC is such that special considerations of radiation hardness for either the detectors or the front-end electronics is not required.

## 4.4 MVD Support Structure

The support structure for the MVD must use a minimum of material thickness to prevent background from photon conversions, but it must also be rigid to support and protect the silicon inside. The MVD will reside inside an enclosure, which opens in a 'clam shell' fashion to allow installation around the beam pipe. The total allowed mass budget of the MVD is very restrictive. This is especially true in the central barrel region of the detector that shadows the acceptance of the PHENIX electron arms. In order to minimize the mass MVD used low density Rohacell foam wherever

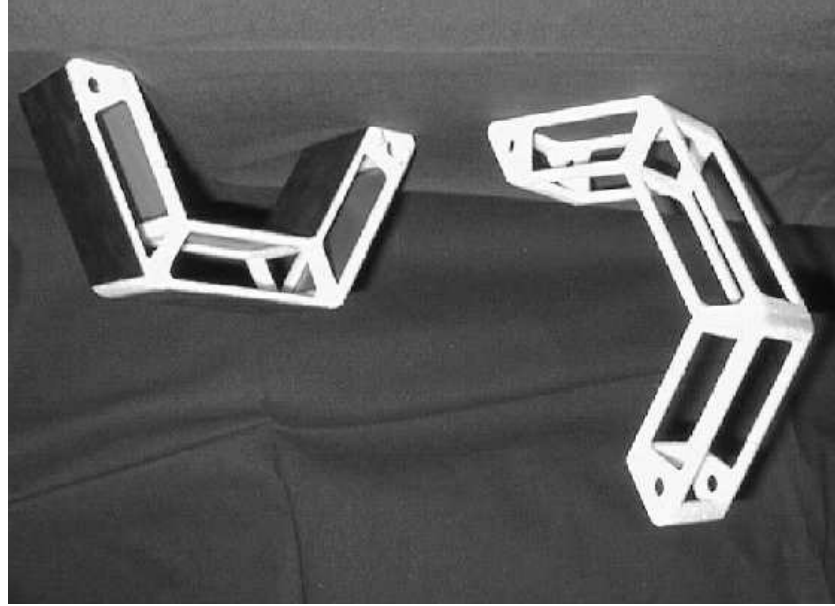


Figure 4.6: Photograph of C-cage

possible. The radiation length of this foam is 545 cm.

The unit mechanical support of the barrel is called a C-cage . The cage is machined from a laminated block of Rohacell-71 foam. strip detectors are glued to three outer and three inner faces of the cage. The cages are assembled contiguously along the z-axis, registered to each other with plastic tubing, held in place under spring -loaded compression. In Fig. 4.6 is presented a photograph of a so-called C-cage, machined out of Rohacell. 12 of these, stacked end-to-end, will make up one half of the MVD structure that carries the Silicon.

It is well known that Rohacell is hydroscopic, and therefore it is essential to understand the relationship between humidity and the potential distortions and stresses induced into the mechanical support. C-cage shape relatively stable, especially with silicon panels glued to the faces. It was examined the behavior of the cages over the range of relative humidity from 30-80%, where the higher value corresponds to loss of environmental control in the detector, and the lower value to nominal ambient conditions. It was discovered that stress depends on the glue thickness and type. If the

glue joint is made thin enough, the stresses levels could exceed the tensile strength of the Rohacell.

finite element analysis was also run to determine the maximum deflection of the assembled half-barrel due the loading of the silicon and gravity. The maximum occurs as expected, midway along the length of the barrel and is predicted to be  $16\ \mu\text{m}$ . It was already measured and found that measurements to be consistent with the prediction. The deflection is well within MVD's mechanical tolerance.

## 4.5 Electronics

The Multiplicity-Vertex Detector of the PHENIX detector at RHIC consists of approximately 35000 channels of both silicon strips and silicon pads. The per-channel signal processing chain consists of a preamplifier-gain stage, a current-mode summed multiplicity discriminator, a 64-deep analog memory (simultaneous read-write), an analog correlator, and a 10-bit ADC[31, 32]. The system controller or Heap Manager, supplies all timing control, data buffering, and data formatting for a single 256-channel multi-chip module (MCM). Each chip set is partitioned into 32-channel sets.

MVD is one of the most challenging of the PHENIX detector subsystems. The requirements of low-power consumption, small physical area, a channel counts of approximately 35,000, and flexible data handling have resulted in a challenging set of problems. The requirements of the system are to have signal-to-noise not less than 20:1 for a 1-MIP signal which results in noise less than 2500 electrons RMS. The added requirement of being able to discriminate on a 0.5-MIP even for the per-channel multiplicity discriminator is much more difficult.

The multiplicity trigger is formed using the sum of silicon channels (both pads and strips) above a threshold corresponding to approximately 0.25-0.33 of a minimum ionizing particle (MIP). For off-line analysis of the charged particle multiplicity and

fluctuations over 5 units of rapidity, the pulse height from each channel will be used to separate multiple from single hits. In a single event, the MVD is sensitive to multiplicity fluctuations at the 10% level; this is limited by backgrounds and charged particle statistics rather than MVD performance.

A block diagram of the electronics is shown in Fig. 4.7. This includes the preamplifier, discriminator, current-sum output, analog memory-correlator, and ADC. The overall controller, or Heap Manager.

As a consequence of the collision of gold beams, charged particles are produced. When such a track passes through the silicon strip detector, if it possesses sufficient energy to produce an electron-hole pair in the silicon, it produces a signal. The signal is then passed to the preAmplifier for amplification. But as all other electronics circuits, there are some noises, which are also amplified. The next component in the chain is the analog memory units, which keeps these signals, as well as noises, in memory. It later passes the analog information to the analog-to-digital converter for digitization. After the ADC output the data packets are handled by the Heap Manager, which, depending on the trigger criterion, sends the data packet to Data Collection Modules (DCM), where it is written on the disk.

As it is mentioned earlier that a panel in the silicon strip detector is composed of 256 strips. The electronics are mounted on a Multi Chip Module (MCM). Each MCM is connected to a 256-channel strip detector contains 8 preamplifier-discriminator chips and 8 analog memory-ADC chips. Each of these chips contains 32 channels of its respective functions. Fig. 4.8 shows the breakdown view of the electronics chain for one strip detector. the 256 strips are handled by 8 PreAMPs, that is, each PreAmp handles 32 strips. A PreAmp is in turn connected to one AMU-ADC block, which have 32 channels.

We further breakdown the electronics chain to look at one strip in Fig. 4.9. One strip is connected to one PreAmp channel, which is connected to one AMU channel,

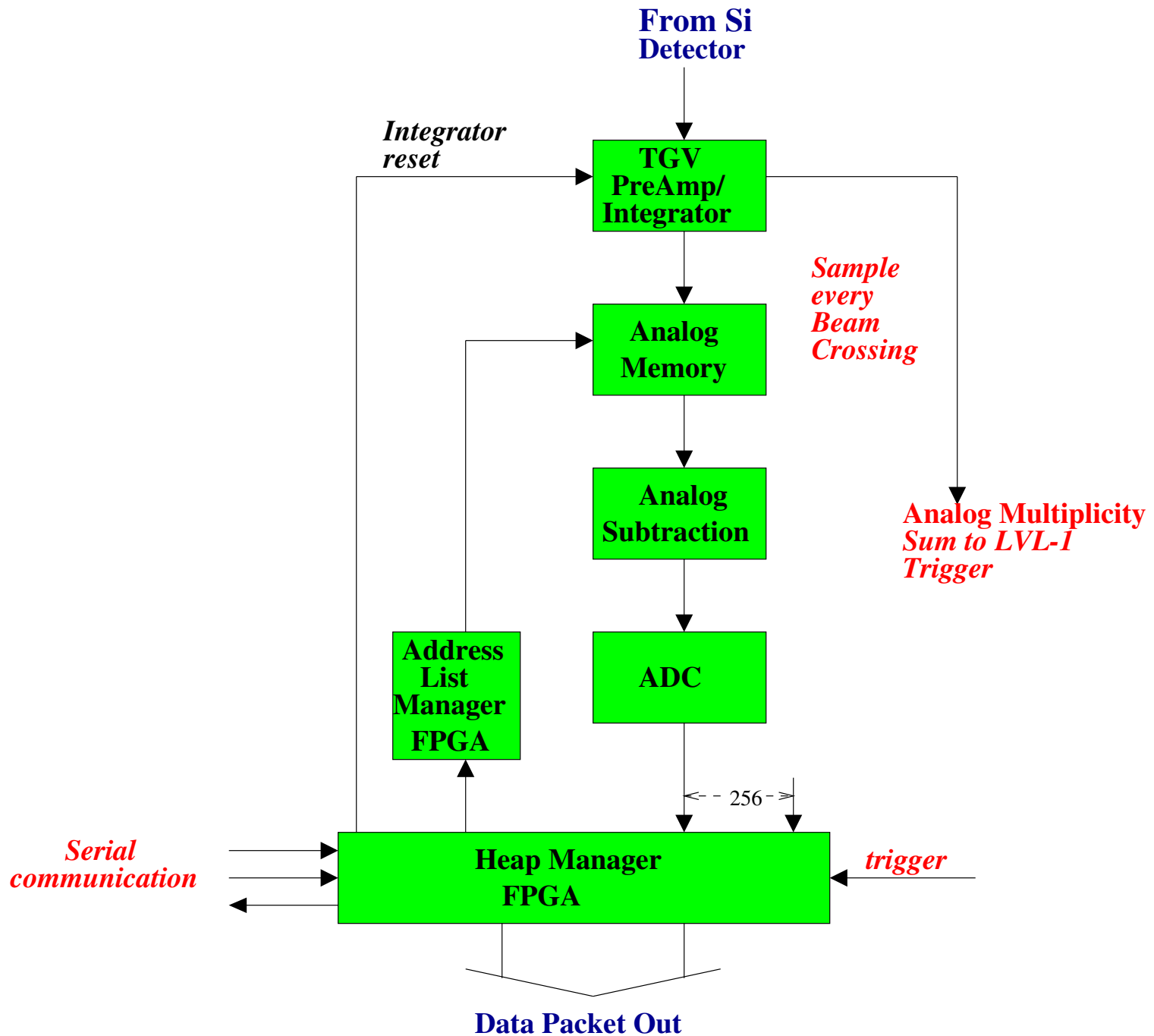


Figure 4.7: MVD Electronics Chain

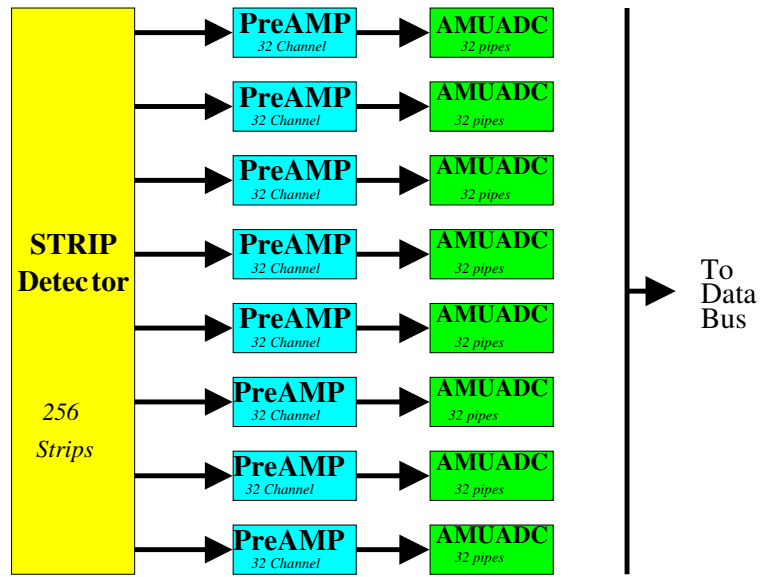


Figure 4.8: Block Diagram of the MVD electronics chain for 1 Strip Detector (256 Strips)

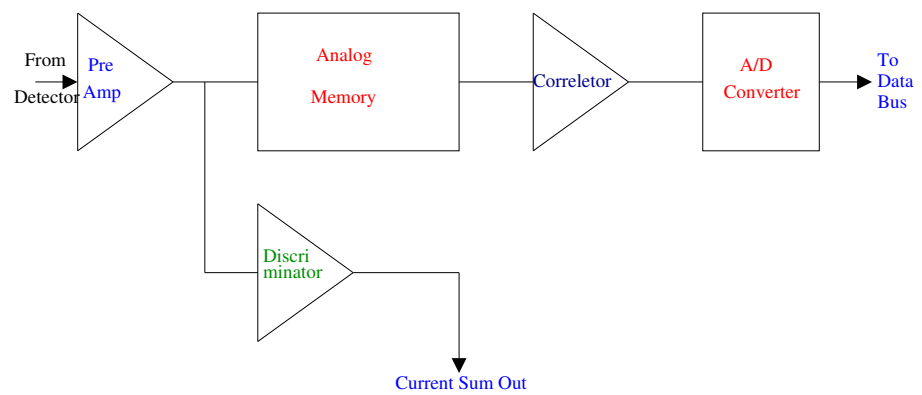


Figure 4.9: Block Diagram of the MVD electronics chain for 1 Strip

which is called an analog memory pipe. Each pipe has 64 cells. So one strip is handled by any one of the 64 cells.

## 4.6 Charged Particle Multiplicity

In PHENIX, the Multiplicity and Vertex Detector is employed to measure the charged particle multiplicity. We describe the physics goals of MVD in Chapter 5.1. Its design makes it capable of measuring thousands of charged particle in collision. It has about 34816 channels, 18432 in the inner barrel, 10240 in the outer barrel and 6048 in the end pads. MVD has an excellent acceptance cover ring about 5 units of pseudorapidity. the exact  $\eta$  range depends on the position of the interaction, and full range in azimuth.

The design employs very high segmentation in the  $\eta$  dimension for the strip detectors, which allows for an accurate determination of the vertex position(simulated longitudinal vertex position resolution for central Au+Au events is a few hundred microns); the segmentation is high in both the  $\eta$  and  $\phi$  dimensions for the pad detectors, which should allow a sensitive search for localized fluctuations in  $dN_{ch}/d\eta d\phi$ .

To calculate  $dN_{ch}/d\eta$  the vertex to be determined first to allow calculation of the pseudo-rapidity ( $\eta = -\ln [\tan \frac{\theta}{2}]$ ).  $dN_{ch}/d\eta$  measurements are generally averages for many events. Statistical fluctuations in the average over many events are therefore less important than the event-by-event fluctuations in the total multiplicity.

The steps followed to calculate  $dN_{ch}/d\eta$  are:

- Vertex : Vertex position must be found.
- $\Delta\eta$  : The range of  $\eta$  occupied by each silicon strip is calculated.
- $N_{\text{hits}}$  : The number of hits in each silicon strip is found. Because the strips parallel to the beam give more reliable information for hits, only those are used to calculate the number of hits.

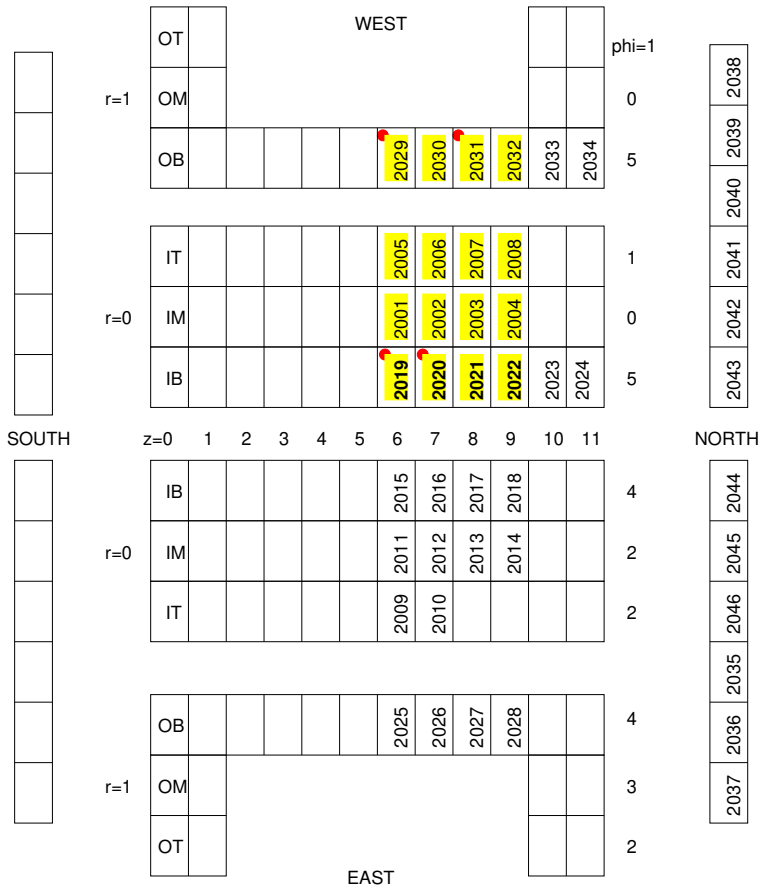


Figure 4.10: MVD Year-1 Configuration

- Multiple Counting Correction : Due to the angular position of the strips from vertex, tracks will pass through more than one strip. Make angular correction in order to avoid multiple counting of a track.
- “measured”  $dN_{ch}/d\eta$  : is the average of  $N_{\text{hits}}/\Delta\eta$  over many events (a Profile histogram)/
- Make acceptance correction for the MVD active region.

## 4.7 A Few Words on Year-1 Configuration

The Multiplicity & Vertex Detector was installed in the PHENIX detector in the summer of 2000. PHENIX was successful to take data in the run. The MVD was not fully populated with electronics in the year-1 run. Only 46 MCMs out of 136 MCMs were installed (Fig. 4.10). But due to some electronics read-out difficulty, MVD was not able to participate in the data taking, except for the final two days of run when MVD went into the main partition with all other subsystems in PHENIX and successfully recorded data. Unfortunately, only two of the MCMs were able to record useful data (MCM#2019 and 2020).

With the above configuration, it is not possible to determine the collision vertex. But the vertex position could be found from the Beam-Beam Counter, although the resolution is 100 times worse than that of MVD. Even with the only two MCMs, MVD still has the largest pseudorapidity coverage in the PHENIX detector system, which is about 1.48 units for collision vertex at zero. So With the Year-1 configuration, useful Physics results can be extracted.

## 4.8 MVD Online Monitoring

When beams collide in RHIC, there are hundreds of events produced. We will select and archive only a fraction of those events those are useful for our physics purposes. Since we can not store all the events generated in the collision, we must have a clever way to choose the useful events and at the same time we must monitor the quality of data and the behavior of the detector. For this purpose, we need online monitoring.

So schematically the process looks like as in Fig. 4.11. From source detector detects particles, from detector it goes to computer, from computer some portion goes to tape and others go to DD pool. Data Distributor (DD) is a UNIX based event buffer manager. The DD package allows distributing events to processes in real

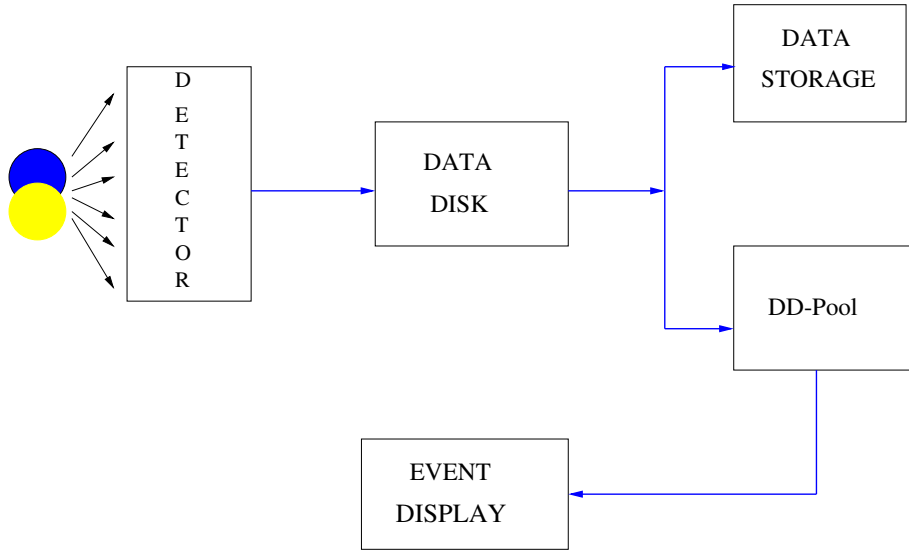


Figure 4.11: Simplified PHENIX Data Collection Chain

time in a multiprocessor environment for data reduction, event building, online event analysis and monitoring. There are three simple user programs: one for a process acting as a producer of data (i.e. he injects data into the DD system), another one acting as a consumer (i.e. he retrieves data from the DD pool) and a simple monitor process (i.e. a process that is neither a producer nor a consumer but a process that attaches to the DD system and has access to various information about the DD pool). At this motoring stage we can get Event Display. For online monitoring we want to work with our histograms, display them at will clear them, fit them, store them, while they are being filled in the background by our monitoring task.

#### 4.8.1 What Do We Want to Achieve?

The main purpose of online monitoring is to look at all the channels of the detector and find out whether the channels are working as they should be. In other words, we want to see if all the channels are 'healthy'. We look the responses of channels, usually in terms of the ADC values, and find out how many channels are dead or is there any channel that is 'hot'.

A channel going dead is most frequent problem. Also sometimes some channels may behave unexpectedly. The online monitoring tool should be wise enough to spot the problem and notify in a reasonably fast way. In PHENIX, ROOT is the environment adopted for analysis and it is a good idea to use ROOT for online monitoring. For online monitoring we should be careful that we want things 'online', that is look at the histograms while data is being processed simultaneously so that we do not miss events and miss the detector problem. That is why a multi-threaded ROOT has been used to develop online monitoring for MVD.

So, both the 'main thread', that is the command prompt or GUI(Graphical user interface) and the background thread can manipulate the same objects. The background thread can fill histograms and at the Graphical User Interface(GUI), we can work with histograms, display them, fit them, clear them.

Now as we have a faster way to work with histograms, how to find the dead and hot channels? We look at the ADC output of channels. We have hundreds of channels and at the particular event there is a likelihood that not all the channels get hit. So we should make a loop over, say 100 events, and look at the average ADC value of channels over the loop. If any of the channels show 0 ADC value over the loop, we can safely conclude that the channel is dead. To find hot channels, we set a threshold for the ADC value. If a particular channel shows an ADC value above the threshold, we say that channel 'hot'.

#### 4.8.2 MVD Online Monitoring Software

With the clear understanding of the MVD channels and their expected behavior, we are in a position to develop the software for MVD online monitoring. The MVD online monitor is developed in a multi-threaded ROOT environment and its main purpose is to look at the global behavior of all channels. It looks for dead channels and hot channels and notify when it finds one such channel.



Figure 4.12: MVD Online Monitoring : MVD Online Monitoring GUI. Here the user selects whether to monitor the global status of the detector or to monitor a single MCM

The MVD online monitor is developed in ROOT environment and its main purpose is to look at the global behavior of all channels. It looks for dead channels and hot channels and notify when it finds one such channel. The prompt is a GUI. The GUI source codes are based on Xclass95, a Windows-95 looking toolkit. Let us look at how does it work. The main tasks of the monitoring software are :

1. Look at the Global status of MCMs, i.e., how many MCMs are working.
2. Look at the ADC value Distribution, which could tell if there are any noisy channels.
3. Choosing some ADC value bin of specified range, whereby know about the dead channels.
4. Look at the status of MCMs, one at a time
5. Look at the Mean and RMS ADC distribution of MCMs and thereby make conclusion whether the MCM is working ok or not.

When the program is run, it gives the GUI as in Fig. 4.12. It asks for an input file. Click on the "Eventfile" and it will give you option to choose a file or read a file from DD-pool (Fig. 4.13).

Once the file being specified and the button is clicked, the next thing to do is to click on the area of the MVD one wants to monitor. For example, if one wants to

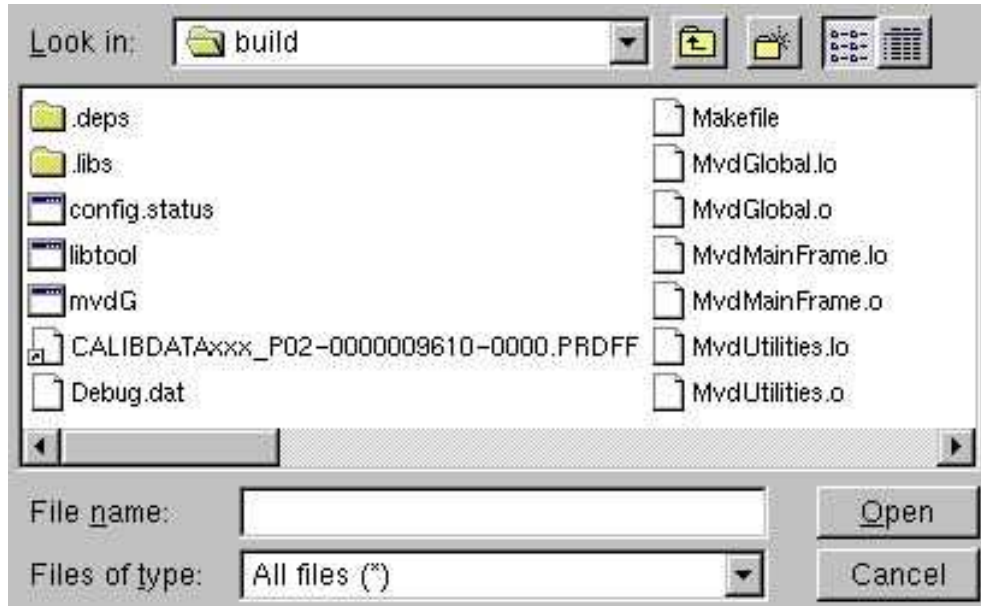


Figure 4.13: MVD Online Monitoring : File Selection Window. Here the user selects the file to read the data from. Here the user has option to select a file from a saved file or use the data in real time from DD-pool

monitor the North Inner Barrel for  $\phi=0-2$ , click on the corresponding button. A new window will be popped out. The only thing to do now is to click on the "Enable Histos". It starts processing and shows the status of all channels. It goes over a loop of a specified number of events and updates on the screen after every loop, while the process is being run in the background.

Now let's look at each histograms in Fig.4.14 . The first histogram from the top shows the status of the MCMs. In the X-axis we plot channel number and in Y-axis we plot the ADC value corresponding to each channel. Looking at the above histogram we can readily see that many MCMs are not working. As we know each MCM corresponds to 256 channels, we can see that only 4 MCMs are working. So it is very useful to know the status of the MVD. In the middle histogram in Fig.4.14 ADC value from all channels are plotted. This is very useful to look at the noisy channels. In the third histogram, a summary plot for ADC values are made. We

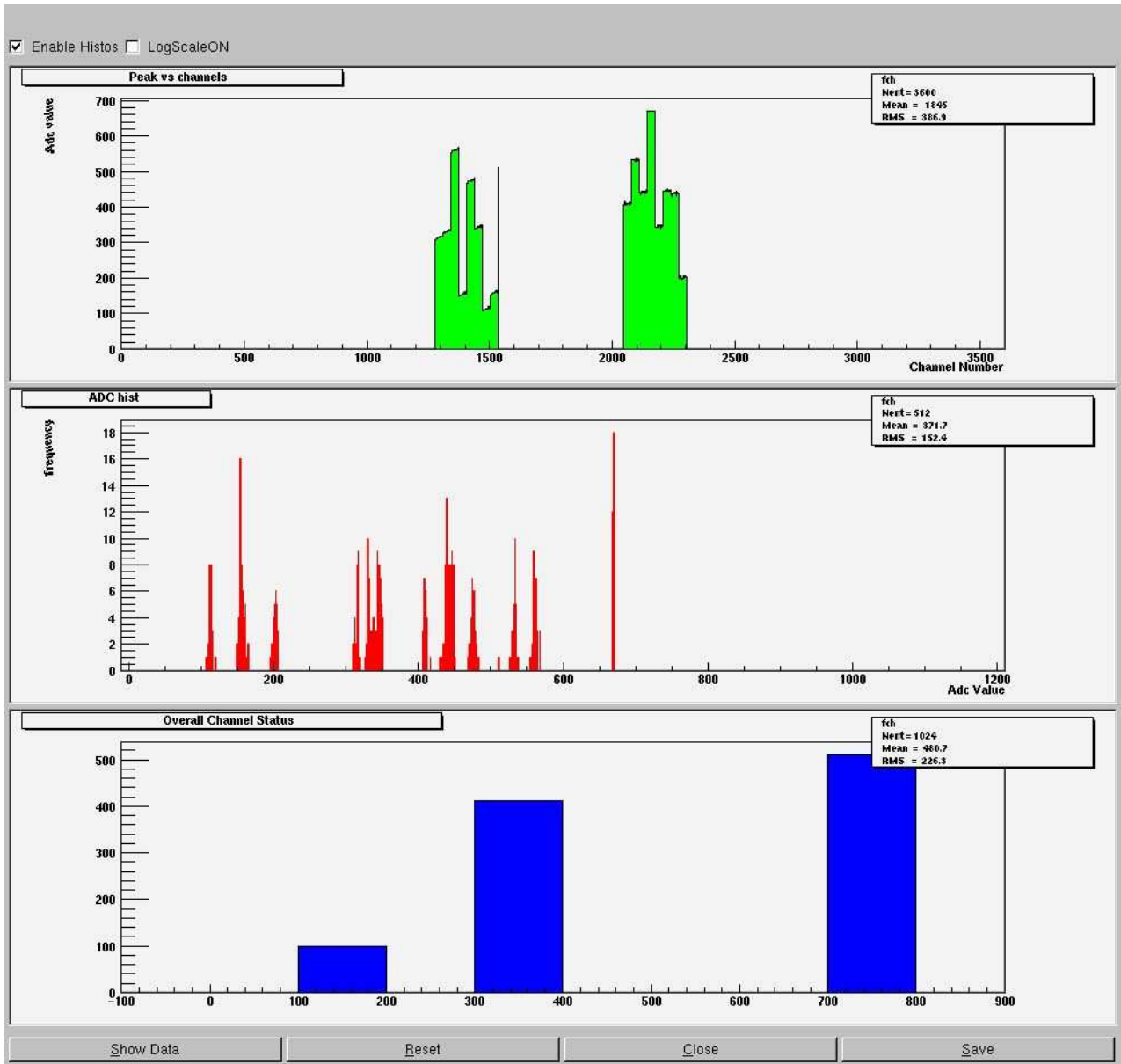


Figure 4.14: MVD Online Monitoring : Global Monitoring. Top plot is the channel number in X-axis vs the corresponding ADC value in Y-axis. The middle plot is the 1-D histogram of the ADC from all channels. The bottom plot is the number of channels that falls in a certain range of ADC. See text for explanation

choose 4 ranges of ADC

- Range 1 : Channels with ADC between 1-200 : → these are the channels that have very low ADC (the first bar in the bottom plot in Fig.4.14).
- Range 2 : Channels with ADC between 200 -800 : → There are the channels that have ADCs in the expected range. These are “good channels” (the second bar in the bottom plot in Fig.4.14).
- Range 3 : Channels with ADC between 800 and more : → very high ADCs (hot channels). In the present plot, we did not have any such channels.
- Range 4 : Channels with ADC 0 : → DEAD channels. These are the channels that do not show any activity over a large number of events (the third bar in the bottom plot in Fig.4.14).

### 4.8.3 Single Strip Monitoring

We can look at 16 MCMs at a time. Fig 4.15 is the 1-Dimensional histogram of ADC value of MCMs. The histograms are arranged according to the MCM number. So we can see the status of single MCMs. In the above example we can find that the MCMs 1,2,8,13,14,15,16 show no ADC. Other MCMs show activity. But 5th MCM have a very wide ADC distribution, the channels are not behaving as expected, and the MCM needs to be checked or the data from the MCM to be discarded. The same is true for the 7th MCM. So It is very good diagnostic tool to look at each MCM.

### 4.8.4 MCM Mean and RMS ADC Monitoring

Fig. 4.16 shows the mean and RMS of ADC values. In X-axis, we plot the MCM number, and in the Y-axis we plot Mean(RMS) ADC for each MCM. This plot should tell us everything about the MCM status. We know that a good MCM should have a mean around 400. So if the Mean is too low or the mean is two high, it is not a

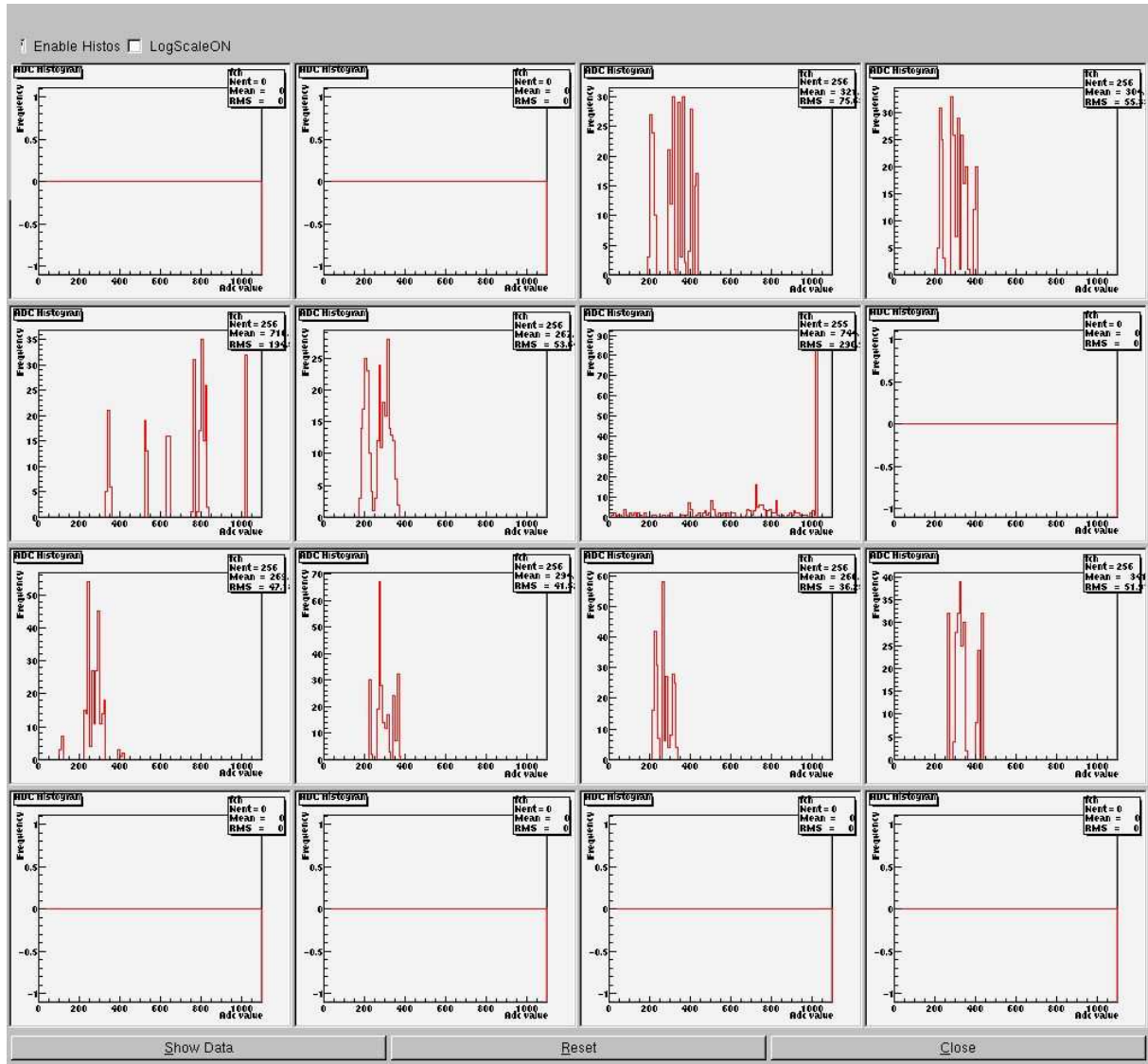


Figure 4.15: MVD Online Monitoring : Single Strip Monitoring. Shown 16 plots for the 1-D ADC distribution for 16 MCMs.

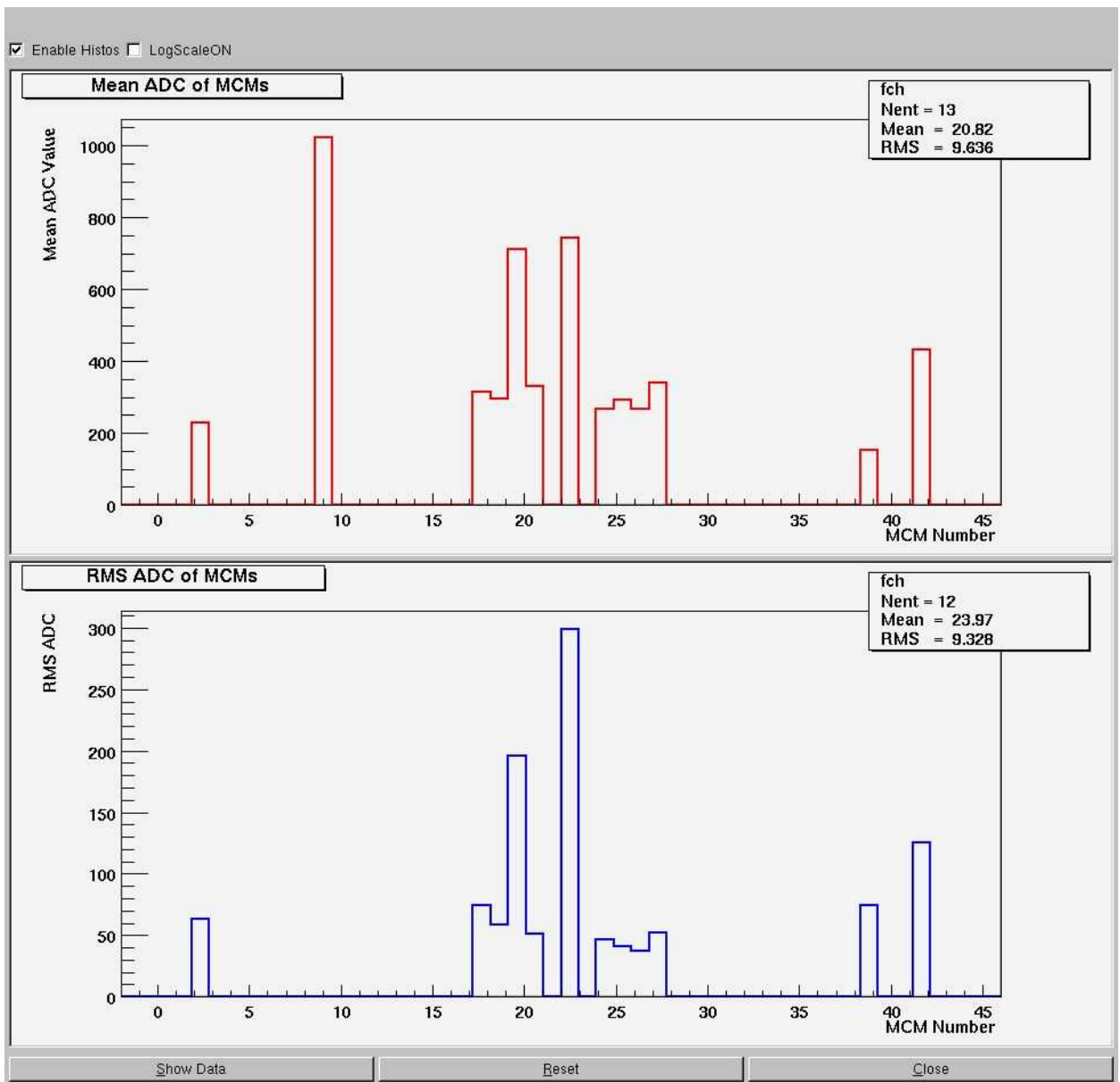


Figure 4.16: MVD Online Monitoring : Strip Mean & RMS Monitoring. Top plot is MCM number in X-axis vs the corresponding mean ADC. The bottom plot is MCM number in X-axis vs the corresponding RMS of the ADC distribution. See text for explanation

good MCM. We can put a line on the plot for the upper threshold for the mean and also a lower threshold so the shift crew can just look at the plot and find out how many MCMs are behaving badly and thereby notify the MVD experts for necessary measures. The same should apply for the RMS plot.

## 4.9 Conclusion

The Multiplicity and Vertex Detector in PHENIX is composed of Silicon Strip and Pad Detectors. MVD can measure collision vertex with an accuracy of a few millimeters. It has a pseudorapidity coverage of  $\pm 2.5$  units and complete azimuthal coverage. It is thus capable of measuring the charged particle multiplicity with great accuracy. The charged particle multiplicity measured by MVD can be used to make an estimate of the Bjorken energy. This information might lead to a possibility of a phase transition in the heavy ion collisions. Unfortunately only about 2% of the electronics were working in Year-1. But even with this small fraction of MVD active coverage, it has still the largest pseudorapidity coverage in the PHENIX detector. Therefore even with the limited coverage and electronics we still expect that some useful Physics results can be extracted. We will find later that indeed MVD provided some useful Physics results with the data taken in the summer of 2000.

# Chapter 5

## Charged Particle Multiplicity Measurement in MVD

### 5.1 Physics Goals of MVD

PHENIX will measure several quantities that are considered “Global observables”, i.e. quantities which describe the overall dynamics of the collision, including charged particle multiplicity ( $dN_{ch}/d\eta$ ), transverse energy ( $dE_t/d\eta$ ), mean transverse momentum ( $\langle p_t \rangle$ ) of produced hadrons, and the number of spectator neutrons ( $\langle N_{spect} \rangle$ ). These quantities are inherently of great interest, providing valuable information regarding the dynamics of nucleus-nucleus collisions at RHIC energies. Investigating the mean behavior of  $dN_{ch}/d\eta$  and  $dE_t/d\eta$  as a function of  $N_{spect}$  should lead to a better understanding of energy deposition and subsequent particle production in the interaction region .

PHENIX will study QGP via simultaneous measurement of many signatures as a function of energy density achieved in the collisions. The determination of the energy density of the system formed in the RHIC collisions is the core of the PHENIX physics program. Energy density  $\epsilon$  can be inferred from actual measured quantities using the Bjorken formalism[23] :

$$\epsilon \approx \frac{1}{\pi R_T^2 \tau_0} \frac{dE_t}{Dy} \approx \frac{1}{\pi R_T^2 \tau_0} \sqrt{< p_t^2 > + m_\pi^2} \frac{dN_\pi}{Dy} \quad (5.1)$$

where  $\tau_0$  is typical hadronic scale (1 - 2 fm/c) and  $R_T$  is the size of the system at time  $t=\tau_0$ . MVD can measure the multiplicity that can then be related to calculate the energy density.

The Multiplicity & Vertex Detector was installed in the PHENIX detector in the summer of 2000. PHENIX was successful to take data in the run. The MVD was not fully populated with electronics in the year-1 run. Only 46 MCMs out of 136 MCMs were installed . But due to some electronics read-out difficulty, MVD was not able to participate in the data taking, except for the final two days of run when MVD went into the main partition with all other subsystems in PHENIX and successfully recorded data. Unfortunately, only two of the MCMs were able to record useful data (MCM#2019 and 2020). MVD could participate in only two runs, run#12397-0000 through run#12397-0078 and run#12399-0000 through run#12399-0002, a total 81 PRDF files. During those runs magnet was on and  $\sqrt{s}=130\text{GeV}$ .

## 5.2 Simulation

Before proceeding to analyze data from the real collision in PHENIX, we simulate real life experiment in a Monte-Carlo codes. When two gold beams accelerated at the RHIC collide and interact inside PHENIX, thousands of particles will be produced. We call each single interaction as an *event* . So an *event* means

- Position coordinate of the interaction point, *i.e.*, vertex
- Particle specie *e.g.*  $\pi^+$ ,  $\pi^-$ ,  $K^+$  etc
- Particle momentum (energy and mass)

We try to simulate real life interaction in PHENIX in Monte-Carlo. We generate particles in an event by event basis. For simplicity we first assume that the vertex is fixed. Later we will accommodate moving vertexes. So, the characteristics of the Monte-Carlo particles are:

- Fixed vertex ( $z = 0$ )
- Generate 200 events
- In each event throw pions in the rapidity range of  $-3 < y < 3$ .
- Throw random number of 6000 particles in each event.
- Particles are flat in rapidity ( $y$ ) and exponential in the transverse mass ( $m_T$ ).

Once the particles are generated they are made to pass through the active region of MVD, which is between  $z = 0$ cm and  $z = 10.5$ cm. This active MVD region consists of two silicon strip detectors, each of them have 256 strips. So the space covered by each strip is roughly 0.02 cm. We thus have total 512 strips. We look at the particle tracks in each strip, measure how much charge is deposited on each strip and find the multiplicity.

### 5.2.1 Variables

The generated particles are pions random in rapidity  $y$  and azimuth  $\phi$  and exponential in the transverse mass  $m_T$ . The other kinematic quantities are calculated from these input variables.

$$-3 < y < 3$$

$$0 < \phi < 2\pi$$

$$m_0 = 0.13957 \text{ GeV}$$

$$\frac{1}{m_T} \frac{dm_T}{dy} = \exp -(m_T - m_0)/T$$

$$\begin{aligned}
p_T &= \sqrt{m_T^2 - m_0^2} \\
p_x &= p_T \sin \phi \\
p_y &= p_T \cos \phi \\
p_z &= m_T \sinh y \\
p &= \sqrt{p_x^2 + p_y^2 + p_z^2} \\
\eta &= \frac{1}{2} \ln \frac{p + p_z}{p - p_z}
\end{aligned}$$

In Fig. 5.1 we show the generated variables:

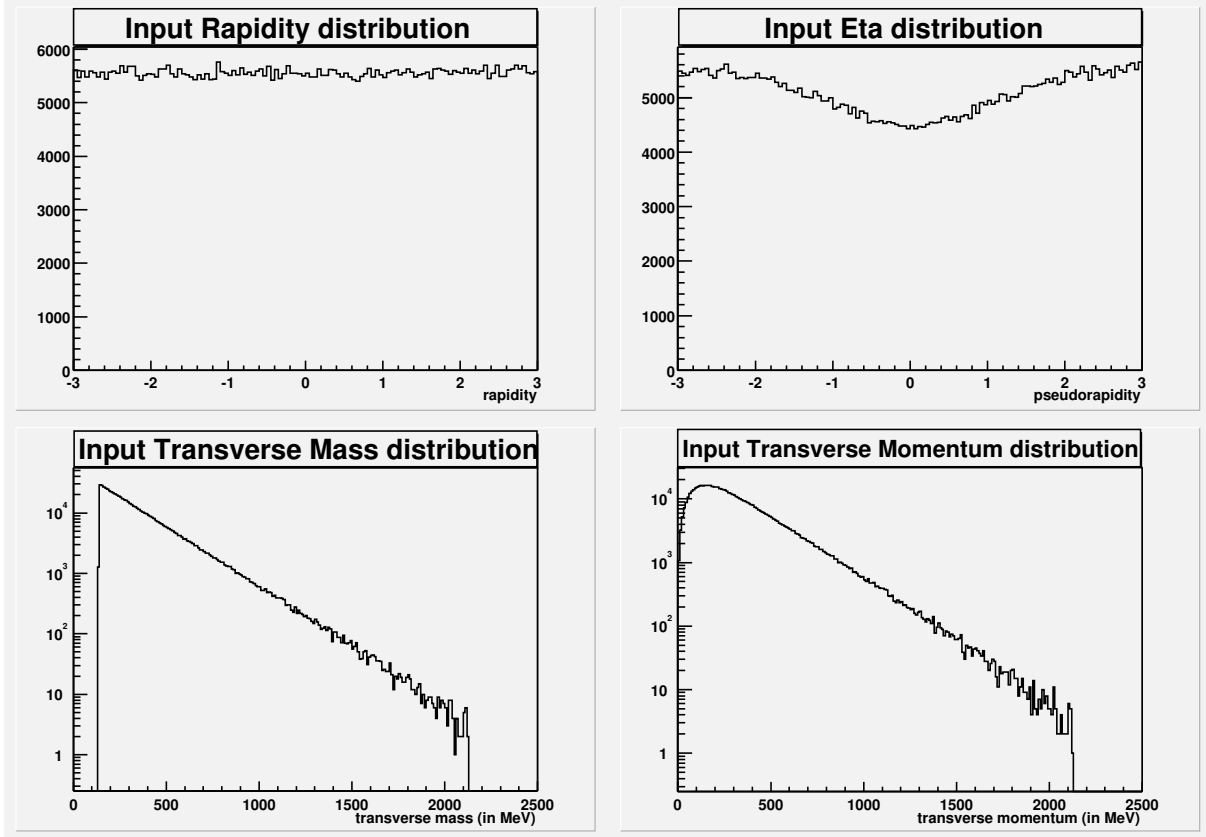


Figure 5.1: Input Variables. These are variables associated with the thrown particles. Clockwise from the top left (a) Rapidity Distribution, (b) Pseudorapidity Distribution, (c) Transverse Momentum Distribution, (d) Transverse Mass Distribution

### 5.2.2 Charge Deposition in Si by a Track

When a particle hits a strip in the MVD, it leaves a fraction of its energy in the silicon. The deposited energy then generates an electron-hole pair in the detector, provided that the deposited energy is larger than the energy required to produce an electron-hole pair. The track that has just sufficient energy to produce a single electron-hole pair is called a **M**minimum **I**onizing **P**article or MIP. So the number of pairs produced, or in other words, the amount of charges deposited in the strips is equal to the total energy deposited by the track in the strip divided by the MIP. The mean energy lose per unit length in a silicon detector is given by the Bethe-Bloch equation[33]

$$-\frac{dE}{dx} = K \rho z^2 \frac{Z}{A} \frac{1}{\beta^2} \left[ \frac{1}{2} \ln \frac{2m_e \eta^2 T_{max}}{I^2} - \beta^2 - \frac{\delta}{2} \right], \quad (5.2)$$

where

$$\begin{aligned} T_{max} &= \frac{2m_e \eta^2}{1 + 2s\sqrt{1 + \eta^2} + s^2} \\ \eta &= \gamma\beta = \frac{p}{M} \\ s &= \frac{m_e}{M} \end{aligned} \quad (5.3)$$

where  $m_e$  is the electron rest mass which is equal to 0.511 MeV, and  $M$  is the mass of the incident particle.  $\rho$ ,  $Z$  and  $A$  are the density, atomic number and mass of the medium and  $I$  is the minimum ionizing energy. For silicon,  $Z/A = 0.49848$  and  $I = 3.6\text{eV}$ . With these parameters and using Eq.(5.2) we can estimate the energy loss for a 10GeV particle in MVD:

Thus, the charge deposition depends not only on the particle type and particle energy, but also on the path-length it covers inside MVD. Therefore, the charge deposited by a track moving a distance  $dr$  inside MVD is

$$\Delta Q = \frac{\Delta E \times dr}{I} \quad (5.4)$$

where  $\Delta E = \frac{dE}{dx}$ .

Particle	Energy GeV	$dE/dx$ MeV/cm
Pion	10.0	4.49249
Kaon	10.0	4.41908
Proton	10.0	4.22217

Table 5.1: Rate of energy loss in Silicon for different particles

We now describe the simple geometry used for charge calculation. Since we have only one type of input particle, namely pions, we are primarily concerned about the path-length of the particle inside MVD, since charge deposition is proportional to the path-length inside the detector. The detector active region is about 10.5 cm and located between  $z=0$  cm and  $z=10.5$  cm. There are 512 strips in this region. So each strip roughly covers about 0.02cm. Let us call this  $z$  coverage of a strip as  $\Delta z$ . Each of the strips are 300  $\mu\text{m}$  thick. Let us call this thickness as  $dx$ . Moreover, there is a finite  $\phi$  coverage of each strip, which is between  $-30^0$  and  $30^0$ . The strips are located about 5cm from the beam pipe. When a track hits a strip we know the hit position, which we call  $z$  and the pseudorapidity  $\eta$  at the hit position. Thus we note all the quantities we know from a hit:

$z$ coverage of a strip	$\Delta z = 0.02\text{cm}$
Thickness of a strip	$dx = 0.03\text{cm}$
$\phi$ coverage of a strip	$-\frac{\pi}{6} < \phi < \frac{\pi}{6}$
Distance of the center of the strip from vertex	$x = 4.985\text{ cm}$
Hit Position at the strip	$z$
Pseudorapidity at the hit position	$\eta$
Angle at the hit position from vertex	$\theta = 2 \tan^{-1}(\exp(-\eta))$

Let us consider two scenarios: Let us look at the Fig. 5.2. A track passed through only one strip. In this case the total energy deposited by the track is concentrated to only one strip. From the geometry, it is easy to see that the path length of the track inside MVD is

$$dr = \frac{dx}{\sin \theta} \quad (5.5)$$

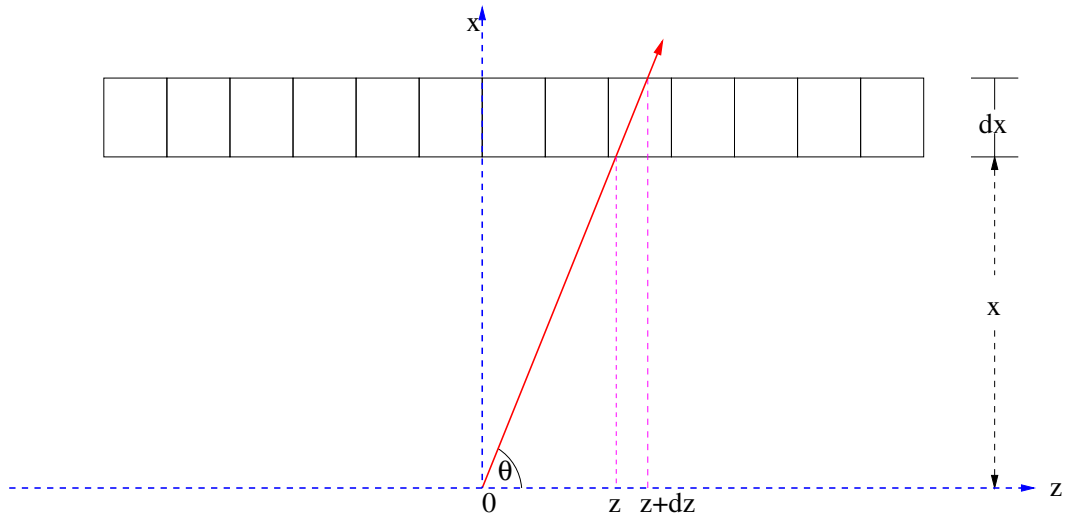


Figure 5.2: Geometry to calculate charge deposition when a track goes through a single strip

But the strip has a finite  $\phi$  coverage. So we should include a correction factor  $1/\cos \phi$  :

$$dr = \frac{dx}{\sin \theta} \times \frac{1}{\cos \phi} \quad (5.6)$$

And the charge deposited by the track is simply

$$\Delta Q = \frac{\Delta E \times dr}{I} \quad (5.7)$$

Now let us consider other scenario when a track passed through the neighboring strips in Fig. 5.3. In this case, the total energy deposited by the track inside MVD is shared be the two strips. Let us consider that the track passes through  $i$ th and  $(i + 1)$ th strip. From Fig. 5.3 we see that

$$\begin{aligned} dz_1 &= (i + 1)\Delta z - z \\ dz_2 &= dz - dz_1 \end{aligned} \quad (5.8)$$

Therefore the path length inside the strips is:

$$dr_i = \frac{dz_i}{\cos \theta} \times \frac{1}{\cos \phi}, \quad (5.9)$$

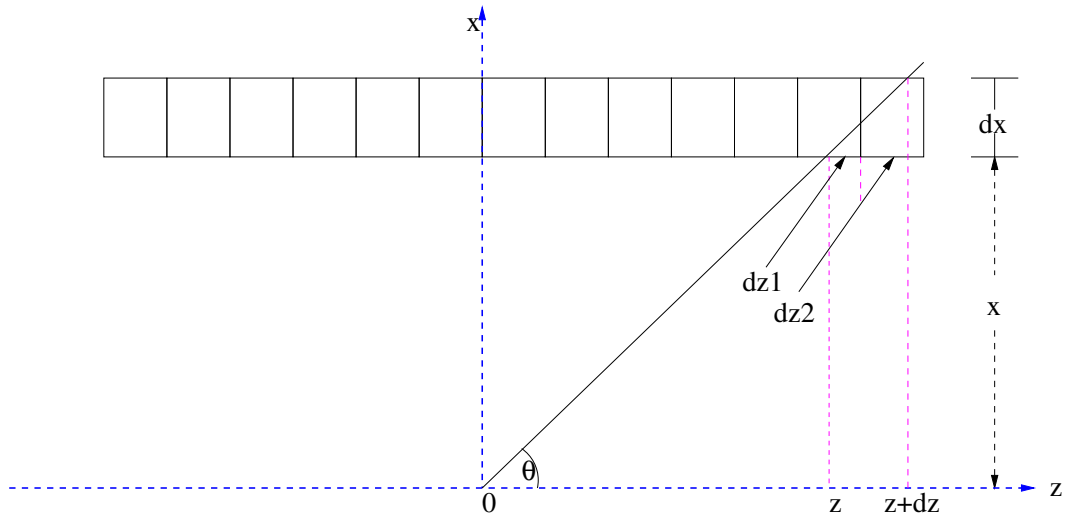


Figure 5.3: Geometry to calculate charge deposition when a track goes through multiple strips

from where the charge deposition can easily be calculated.

We now look at the charge distribution in MVD deposited by Monte Carlo tracks. Since the maximum distance that track cover during its passage in MVD is 0.040629 cm when it goes diagonally through the strip, the maximum charge deposited by a single track can be only  $8.52755 \times 10^{-15}$  Coulombs. But going exactly diagonally occurs very occasionally, rather the tracks, in most of the times, pass almost straight with some  $\phi$  angle. The Fig. 5.4 demonstrates this phenomenon. In fact if the track goes straight the maximum charge can be between  $6.29665 \times 10^{-15}$  Coulombs and  $7.03987 \times 10^{-15}$  Coulombs due to the finite  $\phi$  coverage. We see in figure 4.7 that the maximum number of entries occur around  $7 \times 10^{-15}$ . The charge corresponding to this peak is the charge due to a single track MIP.

Now what is about the entries below 6? These entries are for tracks going through more than one strip. Since while the track goes through more than one strip, the charge is “shared” be the strips. So we see a small charge in strips in these type of situation.

We can also clearly see two tracks MIP peak around 13 and also a three track

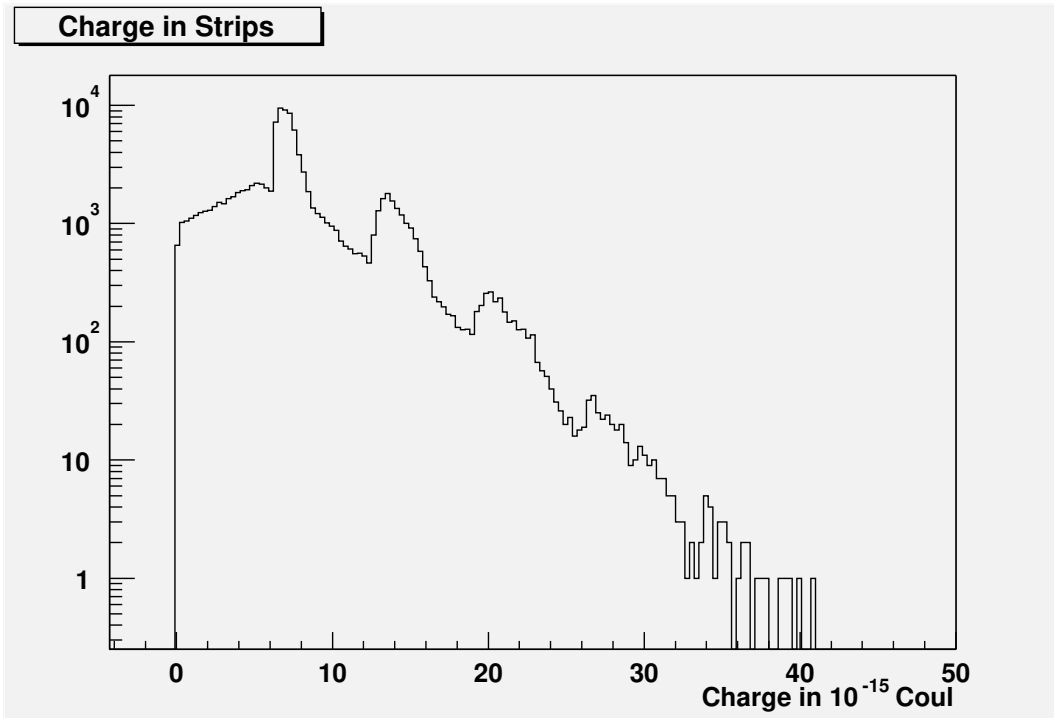


Figure 5.4: Charge Distribution in MVD from the Monte Carlo tracks

MIP peak around 19.

### 5.3 Real data : Run Condition and Vertex

We now describe the procedure and results obtained in the determination of the charged particle multiplicity  $dN/d\eta$  in the Au-Au collision at  $\sqrt{s} = 130$ .A GeV. The analysis is based on the information from the active region of MVD. But also BBC was used for vertex determination and BBC & ZDC for centrality measurement.

The analysis is based on the PHENIX run number 12397-0000 through 12397-0032, 12397-0034 through 12397-0078, and 12399-0000 through 12399-0002, a total 81 files. In these files there are 67610 events were recorded in the MVD active region. During these runs the central magnet was on. Fig. 5.5 shows the luminosity condition during the run.

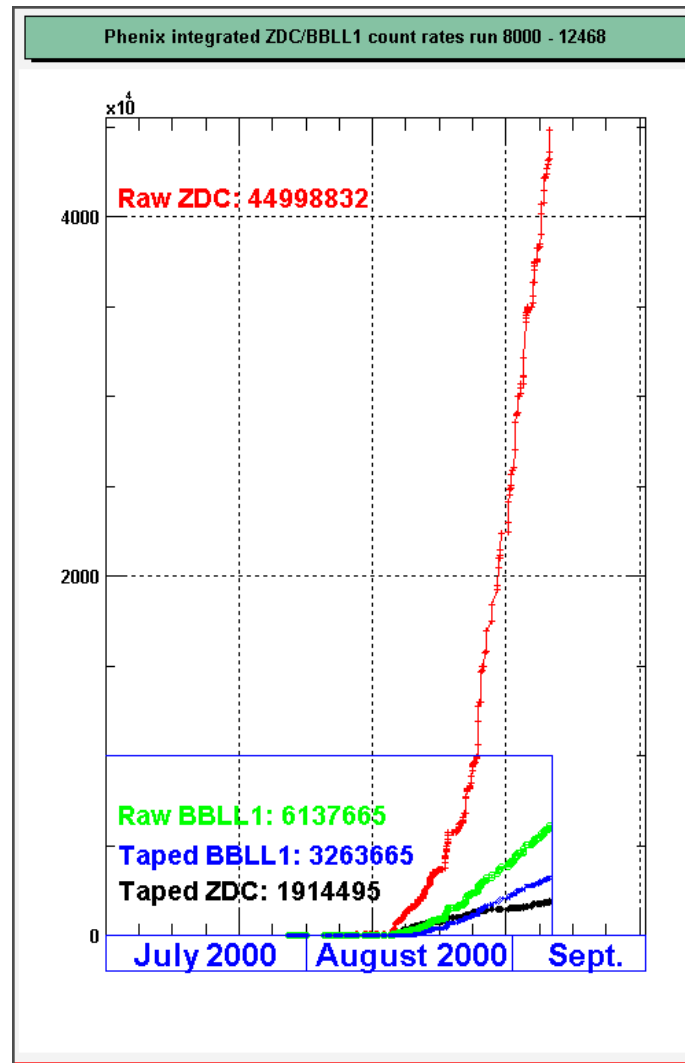


Figure 5.5: PHENIX Run Condition : The total number of triggers recorded in PHENIX during the Au-Au run in the year of 2000[37].

During this run events were accumulated using Zero Degree Calorimeter and Beam Beam Counter as the triggering device. The primary interaction trigger is generated by a coincidence between the north and south BBC with at least two photo multipliers fired in each of them. Another trigger is generated by a coincidence between the two ZDC, each one with an energy signal larger than 10 GeV. This trigger reflects the nuclear interaction plus the mutual Coulomb dissociation cross sections. Most BBC triggers (97.8%) also satisfy the ZDC trigger requirement.

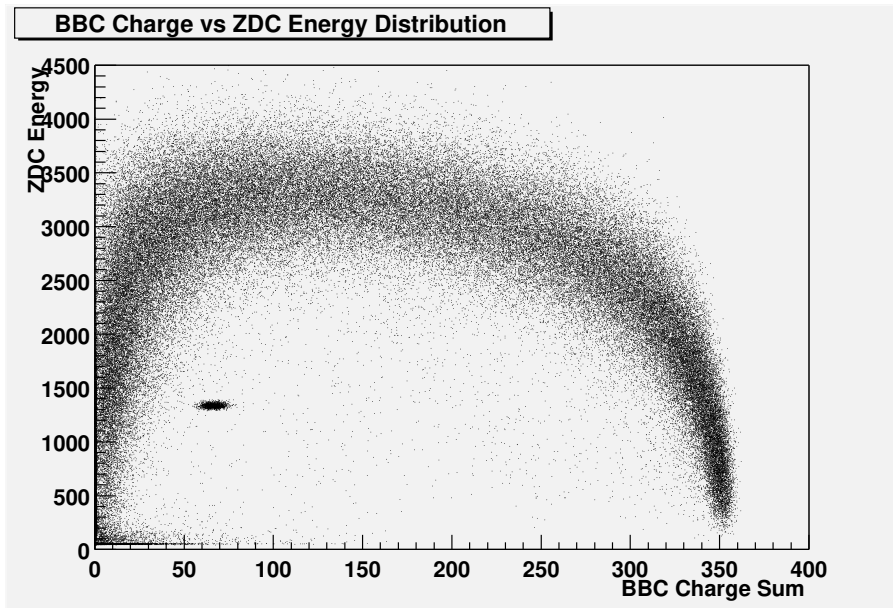


Figure 5.6: Trigger Selection from BBC Analog Sum and ZDC Energy Sum

Fig. 5.6 shows a 2-dimensional plot BBC total charge vs ZDC energy. There are some contamination near  $57.8 < \text{BBC charge} < 77.9$  and  $1150 < \text{ZDC energy} < 1400$ . We, therefore, make a cut in this region. In our analysis we will follow this cut throughout.

In the Fig. 5.7 we see the vertex reconstructed from BBC at the left plot and the ZDC vertex on the right plot. Figure 5.8 shows the nice correlation between BBC vertex and ZDC vertex.

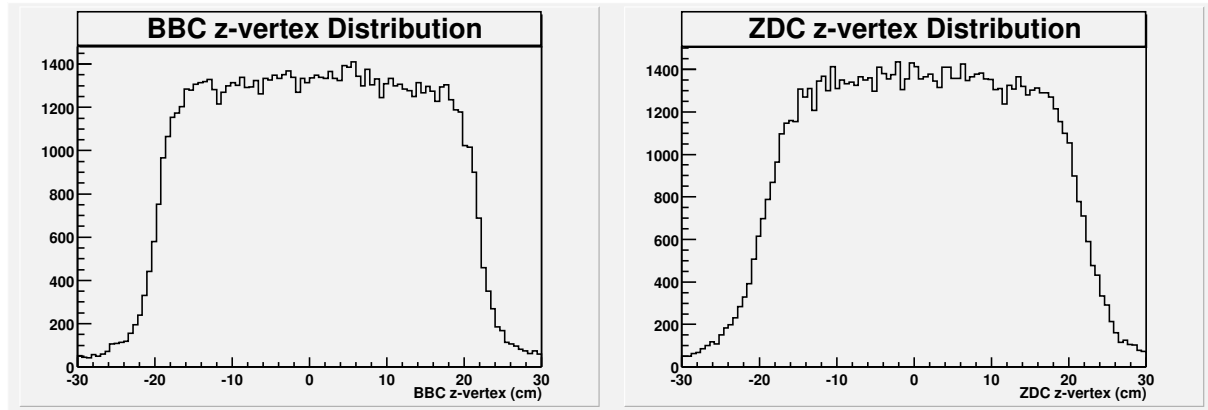


Figure 5.7: BBC and ZDC vertexes. The left plot is the BBC Z vertex, and the right one is ZDC Z vertex

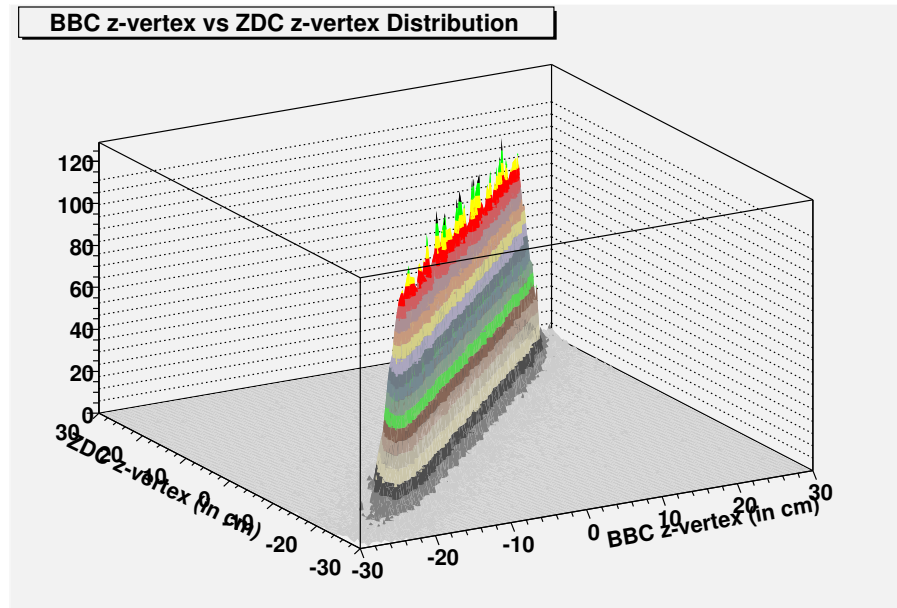


Figure 5.8: Correlation between BBC z-vertex and ZDC z-vertex

## 5.4 Centrality Selection

When the two Au-Au beams collide, they do not necessarily collide head on. In fact the beams may collide anywhere between head-on to barely touching each other. The situation of the collisions may be well described in the Fig. 5.9. The plot is a

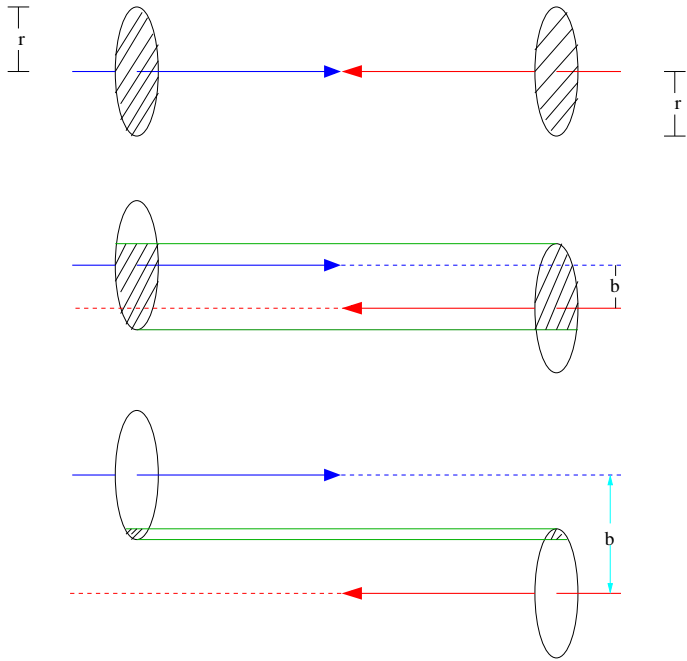


Figure 5.9: Collision between the two beams. The top figure describes the head-on collision, the middle is for a mid-central collision and the bottom is for a peripheral collision

description of the collisions in terms of the impact parameter  $b$ . The impact parameter is the distance between the centers of the two nuclei. Since we are considering the collision between two gold beams, the radii  $r$  of the two nuclei are the same. So in a head-on collision, the impact parameter  $b = 0$ , all the nucleons participate in the collision. These are the most *central collisions*. But when  $b > 0$  a fraction of the nucleons take part in the collision. The extreme condition is when the impact parameter  $b = 2r$ , when the edges of the beams barely touch each other. These types of collisions are the most *peripheral collisions*.

Now let us think of a way to measure the collision centralities experimentally. In a head-on (most central) collision all the nucleons will take part in the collision and as a consequence a large number of particles will be produced. This means no *spectator* will be left out in the beam. Of course collision at zero impact parameter very rarely happens. As the impact parameter deviates from zero, lesser numbers of nucleons takes part in the collision and lesser number of particles produced in the collisions. Which means more spectators left in the beam. So if we look at the collisions in terms of the centrality from most central to most peripheral, the number of particles produced in the collisions becomes smaller, but the number of spectators becomes larger. So if we record the number of particle produced and the number of spectator nucleons in each collision, it will give us a clear indication as the collision centrality. In PHENIX we utilize this idea to measure the centralities of the collisions and group the events accordingly. The PHENIX definition of centrality is the fractional difference between the collision cross section and the total geometrical cross-section measured in PHENIX, i.e. ,

$$\text{centrality} = \frac{\sigma_{tot} - \sigma}{\sigma_{tot}}, \quad (5.10)$$

where  $\sigma_{tot} = \pi r^2 = 139 \text{ fm}^2$  is the total geometrical cross-section, with  $r = 6.65 \text{ fm}$  is the radius of the gold nucleus and  $\sigma$  is the collision cross section.

As mentioned we need two detectors in order to record the number of particles produced and the number of spectator nucleons. To record the number of particles produced, the detector should be within the interaction region. To record the spectator nucleons, the detector should be away from the collision vertex, but along the beam line. That is why in PHENIX we use the Beam-beam counter (BBC), which is located along the beam line up and downstream of the beam crossing point and within the interaction region, to record the number of produced particles. The Zero Degree Calorimeter (ZDC), which is also located along the beam line up and downstream of the beam crossing point, but outside of the interaction region (18 m), is used to

record the number of the spectator nucleons. The BBC measures charge deposited by the tracks produced in the collisions and the ZDC record the energy of the deposited spectator nucleons. In the Fig. 5.10 we see the the BBC analog charge sum from the produced tracks and the energy sum in the ZDC from the spectator nucleons.

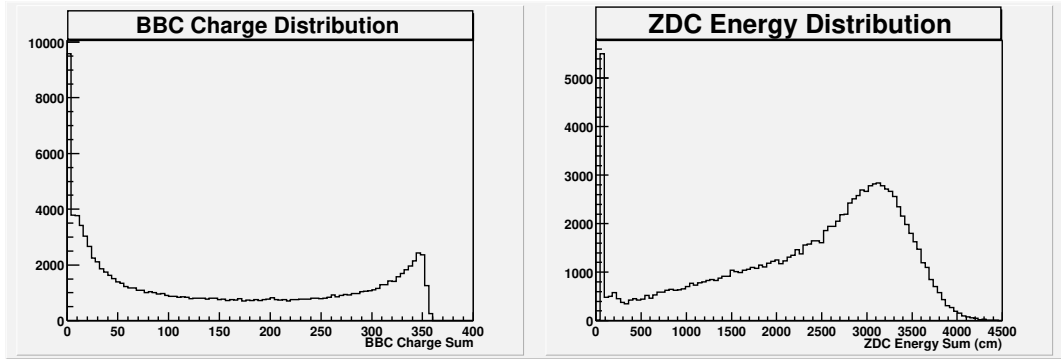


Figure 5.10: BBC and ZDC quantities used for collision centrality determination. The left plot is the BBC charge sum, and the right one is ZDC energy

We adopt the procedure described in the reference[38]. We plot a 2-dimensional plot of BBC charge ( $Q$ )vs ZDC energy ( $E$ ). For a given point on the graph, one can calculate the angle  $\phi$  of a given  $(Q,E)$  point with respect to a fixed origin  $(Q_0,E_0)$ . This method allows a quick and simple calculation of a centrality based on the BBC  $Q$  and ZDC  $E$ . The centrality angel  $\phi_{cent}$  is determined from the 2D  $(Q,E)$  space.

Fig. 5.11 shows the BBC charge vs ZDC energy plot. The maximum BBC charge  $Q_{max}$  is 400 and the maximum ZDC energy  $E_{max}$  is 4500 GeV. Then

$$\phi_{cent} = \tan^{-1} \left( \frac{(Q - Q_0)/Q_{max}}{E/E_{max}} \right) \quad (5.11)$$

where  $Q_0 = 0.2Q_{max}$ [38]

with the centrality bins shown in alternate colors. The bin at the bottom right corner corresponds to the top 5% most central events, the next bin is 5%-10% of the most central events, and so on. The centrality classes and the corresponding upper and lower value of the  $\phi_{cent}$  is tabulated in Table 5.2.

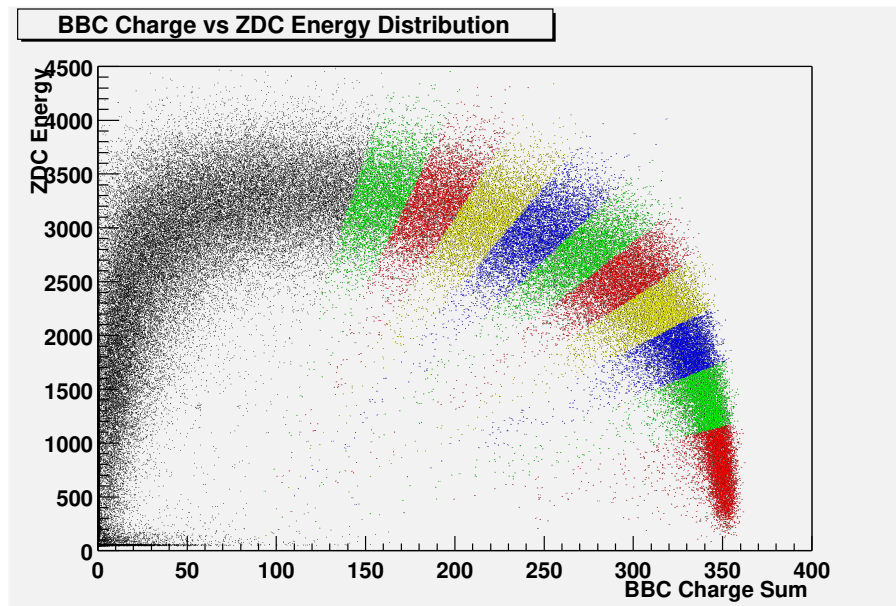


Figure 5.11: Centrality Selection from BBC Analog Sum and ZDC Energy Sum

Centrality (%)	$\phi_{min}$	$\phi_{max}$
min bias	-1.57	1.57
0-5	1.208	1.57
5-10	1.048	1.208
10-15	0.92	1.048
15-20	0.8112	0.92
20-25	0.712	0.8112
25-30	0.616	0.712
30-35	0.5136	0.616
35-40	0.4112	0.5136
40-45	0.312	0.4112
45-50	0.2096	0.312

Table 5.2: The angular coverage of centrality classes in the (BBCQ,ZDCE) space.

## 5.5 Number of Participants

In this section we describe the way PHENIX measures the number of participants ( $N_{part}$ ) and the number of binary collisions ( $N_{coll}$ ) in a nuclear collision. The discussion is based on Reference[38]-[40]. The calculations are based on the measurements made in the BBC and ZDC. The calculation uses the Glauber Model with a Woods-Saxon density profile distribution for the nucleus.

The Glauber model calculates the thickness of a nuclear matter in the direct path of each incoming nucleon and uses the nucleon-nucleon inelastic cross-section ( $\sigma_{nn}^{inel}$ ) to decide whether a nucleon-nucleon collision has occurred. The integration over the total nucleon distribution in each nucleus gives the number of nucleons that took part in the collision. The model uses a few simple assumptions:

1. Nucleons of one nucleus passes straight through the other nucleus.
2. Nucleon-nucleon cross-section remains unchanged in the collisions.

A Monte-Carlo approach is used for the determination of  $N_{part}$  and  $N_{coll}$ . The nucleons of the two gold nuclei are randomly distributed according to a Woods-Saxon distribution :

$$\rho(r) = \frac{1}{1 + \exp\left(\frac{r-r_n}{d}\right)} \quad (5.12)$$

where,

$$r_n = 1.19 A^{1/3} - 1.61 A^{-1/3} \quad (5.13)$$

$$A = 197$$

$$d = 0.54 \text{ fm}$$

In the Glauber calculation the nucleons interact like little black discs with an inelastic cross section of  $\sigma_{nn} = 40 \text{ mb}$ . For the above parameters inelastic Au+Au cross-section of is 7200 mb. The number of participants and the binary collisions calculated from the model is tabulated in Table 5.3.

Centrality	$\langle N_{part} \rangle$	$\langle N_{coll} \rangle$
0%-5%	347 $\pm$ 10	946 $\pm$ 146
5%-10%	293 $\pm$ 9	749 $\pm$ 116
10%-15%	248 $\pm$ 8	596 $\pm$ 93
15%-20%	211 $\pm$ 7	478 $\pm$ 75
20%-25%	177 $\pm$ 7	377 $\pm$ 61
25%-30%	146 $\pm$ 6	290 $\pm$ 47
30%-35%	122 $\pm$ 5	226 $\pm$ 38
35%-40%	99 $\pm$ 5	170 $\pm$ 30
40%-45%	82 $\pm$ 5	130 $\pm$ 24
45%-50%	68 $\pm$ 4	101 $\pm$ 19

Table 5.3: Number of participants and collisions for different centralities[38].

## 5.6 Raw ADC Distribution

In order to calculate the multiplicity distribution it is imperative that we get the MIP distribution. We look at the ADC distribution for strips and we should see a pedestal (noise) distribution and a clear MIP distribution. To see that whether we really see any MIP we plot the ADC values of strips as a function of strip number.

What we observe from the Fig. 5.12 and Fig. 5.13 that

- The uncalibrated raw ADC distribution does not show clear MIPs. The MIPs are “hiding” behind the pedestals (This is due to the fact that the pedestals jumped in event by event. This feature will be discussed in Section 5.9).
- We have a very wide distribution of pedestals.
- The 512 strips do not behave in the same manner. In fact each group of consecutive 32 channels follow same pattern.

The behavior of strips as a group of 32 are not unexpected, since the each MCM that have 256 channels is consisting of 8 chips. So each chip contains 32 channels and each channel have one-to-one correspondence with strips. So the behavior of each 32

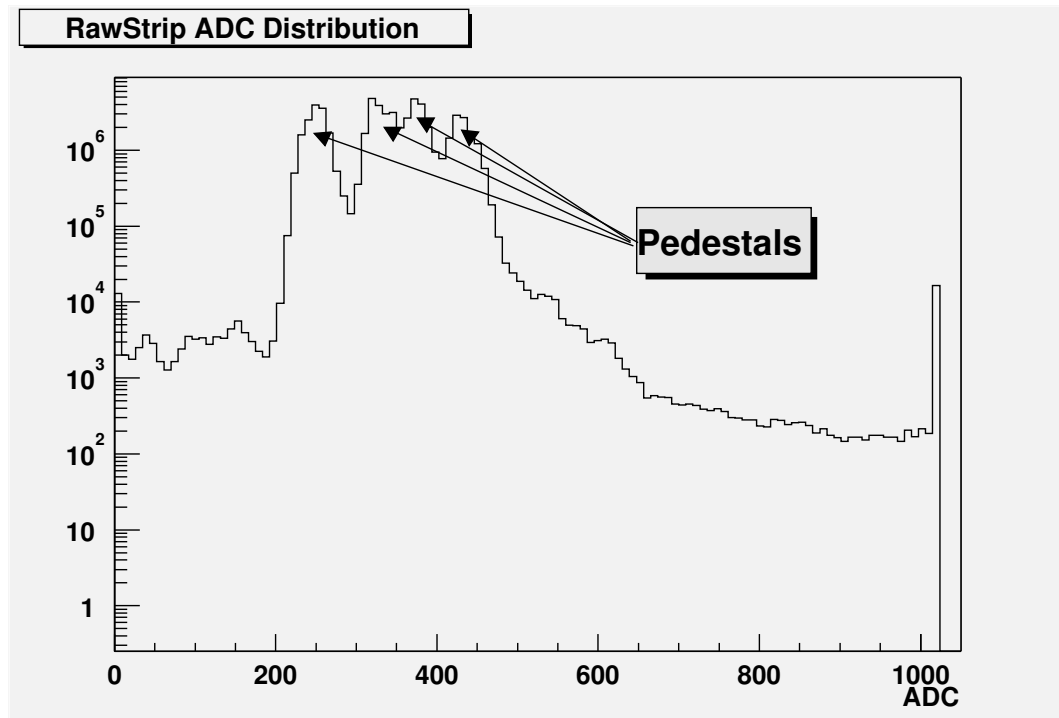


Figure 5.12: Raw ADC Distribution for Strips

strips is due to the behavior of electronic chip it is connected to. It is apparent from this plot that the chips are not calibrated. So we should calibrate all channels. It was found that the pedestals depend on the AMU cell in the MVD electronics chain.

## 5.7 AMU Cell Dependence of Pedestal

In the MVD electronics chain, analog memory units (AMU) are used as analog RAM. It stores the analog signal in its “memory”, which can later be retrieved and passed to the analog to digital converter for digitization. In general, the pedestals should not depend on the position of the AMU cell. But it has been observed that the ADC in a chip (32 channel) shows a strong dependence on the position of the AMU cell. Let us look at the Year-1 data for MVD. We look at the data from all 80 files combined. To show the dependence of ADC on the AMU cell position, we randomly choose one

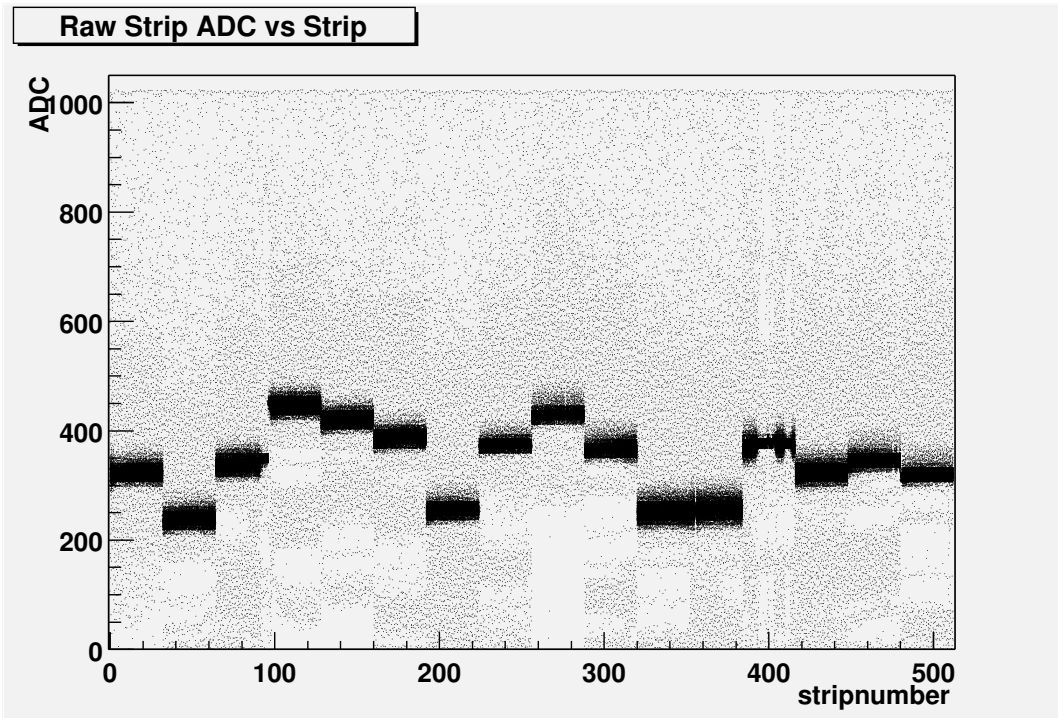


Figure 5.13: Raw ADC Distribution for Strips vs Strip Number

channel from a chip and plot ADC vs AMU. From Fig. 5.14 we see that there are strong dependence of pedestal on AMU cell position. These fluctuations are AMU cell dependent and not depends on the event number. These fluctuations were not observed during the electronics test, this effect was not known until an offline analysis was underway. If it was known earlier, the fluctuations could be corrected online while taking data. In fact this is implemented for the Year-2 data taking. But for the current analysis, we need to develop a tool to take care of these fluctuations offline. Since these is a AMU induced fluctuation, it is worth spending a few paragraphs on AMU cell and its working principle.

### 5.7.1 AMU Operation

Fig. 5.15 shows a block diagram of the AMU-ADC. It consists of 32 parallel analog memory pipes, each pipe 64 cells deep. Each memory cell is a small capacitor, which

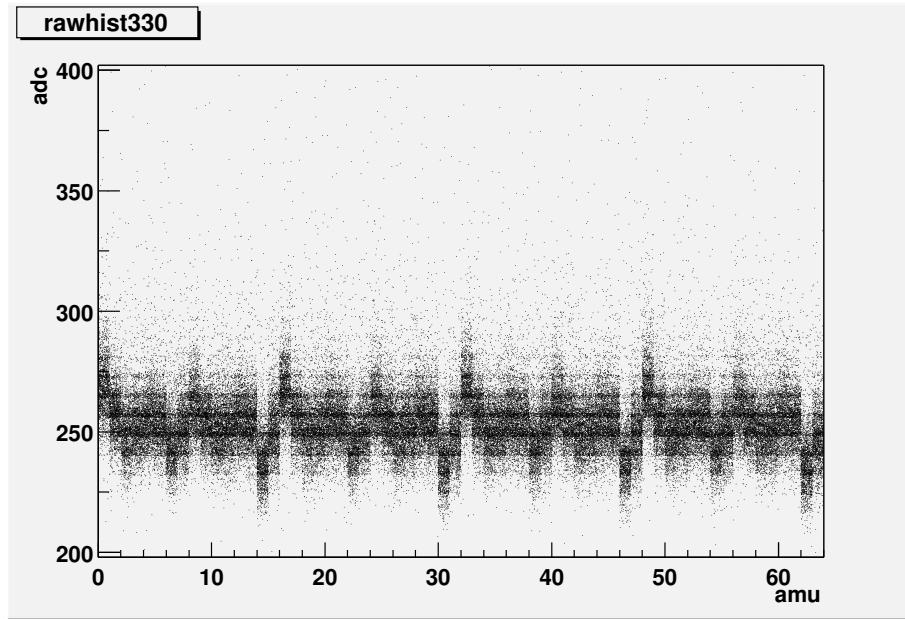


Figure 5.14: AMU vs ADC plot for Strip 330. In one event the data from one strip is handled by any one of the 64 AMU cells. So over a large number of events, all AMU cells contributes to the data handling from a particular strip.

stores the sampled input analog voltage, and read and write switches that connect the memory capacitor to either the Read amplifier or input signal, respectively. The output of each pipe is buffered through a Read amplifier to drive its corresponding ADC channels.

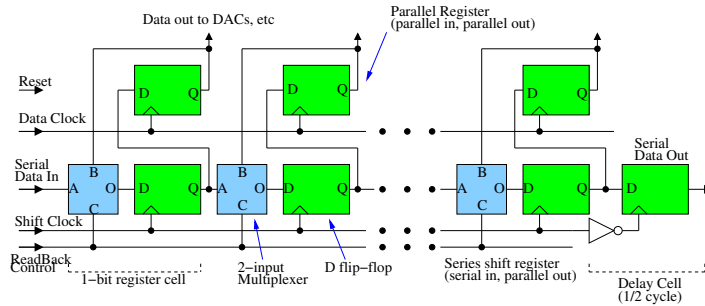


Figure 5.15: Block Diagram of AMU-ADC Block. For the location of the AMU in the MVD electronics chain please refer to Chapter3, Section 3.5

The analog memory section can be thought of as an analog equivalent of the digital

random access memory (RAM). It stores a voltage at a specified cell address, and then later it can read out the specified cell address. To illustrate how the reading and writing is performed in AMU in Fig. 5.16. Each AMU cell is basically a capacitor,

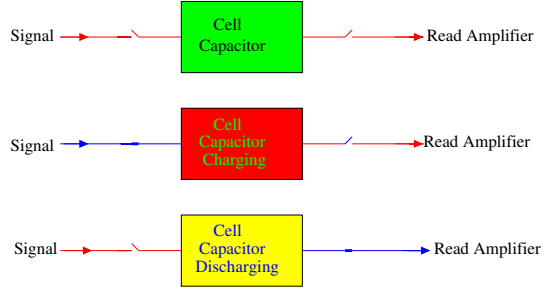


Figure 5.16: Operation of AMU

with a write and a read switch attached to the two ends. In the write mode, the write switch is closed and the signal from the PreAmp charges the capacitor. The amount of charge stored in the capacitor depends on the voltage of the input signal. Later the read switch is closed and the capacitor discharges, which means it passes the input signal information to the read amplifier. At this point it is evident that we need more than just couple of AMU cells. During the collision, thousands of charged tracks will hit the silicon strips. Therefore there is a strong probability that the electronics chains should be ready to handle a large amount of signals within a very short amount of time. Since the AMU cells are capacitors, it takes time for charging as well as discharging. So imagine the situation that the time for charging and discharging of the capacitor is more than the time interval between two consecutive signals. Then the signal that comes later will find the circuit already occupied and will thus be lost. But the beauty of the 64 cell deep AMU is that when a signal comes and finds a cell being already occupied. it finds the next available cell. Thus no information is lost. The 64 cell deep AMU can handle the most central events, when a strip may have high multiplicity. Writing to the cell is performed by sampling an input analog voltage and storing it across a capacitor. The sampling rate will be the PHENIX beam clock

frequency of approximately 9.4 MHz. The maximum writing rate is approximately 12 MHz due to trade-offs in capacitor and switch size versus circuit layout area. Due to the time constant resulting from the resistance of the CMOS switches in the WRITE circuit and the memory cell storage capacitor, 40 ns is required to charge the memory storage capacitor to 12-bit accuracy. Each AMU pipe has its own readout amplifier. The AMU also includes a correlator circuit which is used to look at the voltage difference between two different cell addresses in a pipe. The Multiplicity Vertex Detector subsystem requires this mode of operation due to limited bandwidth available for data transmission. A difference amplifier implemented with switched capacitors obtains this voltage difference. The difference voltage is then presented to the ADC section for digitization.

## 5.8 ADC Fluctuation Correction Procedure

From the ADC vs AMU cell plots we see that there are strong dependence of pedestals on AMU cell position. We need to correct the fluctuation. The idea is that we simply line up the pedestals to a certain value, say at 300. For that purpose we need to plot the ADC for each channel and each AMU cell position. It would be the best if it could be done on an event-by-event basis. But the statistics is so low that an event-by-event plot will not give any significant mean and RMS. We thus plot the ADC per channel per AMU for all events combined, get the mean and normalize at 300. Thus the procedure is as follows:

1. Plot a one-dimensional plot for each channel for each AMU. There will be a total of  $512 \times 64 = 32768$  plots.
2. For each plot (for each channel for each amu) we find the mean of the ADC.
3. We normalize the ADC around 300 :

$$\text{ADC(normalized)} = (\text{ADC(raw)}/\text{Mean}) \times 300$$

As an example we look at the ADC distribution for strip 489 for AMU cell 4. Fig. 5.17(a) shows the raw distribution from all events. Although the distribution is

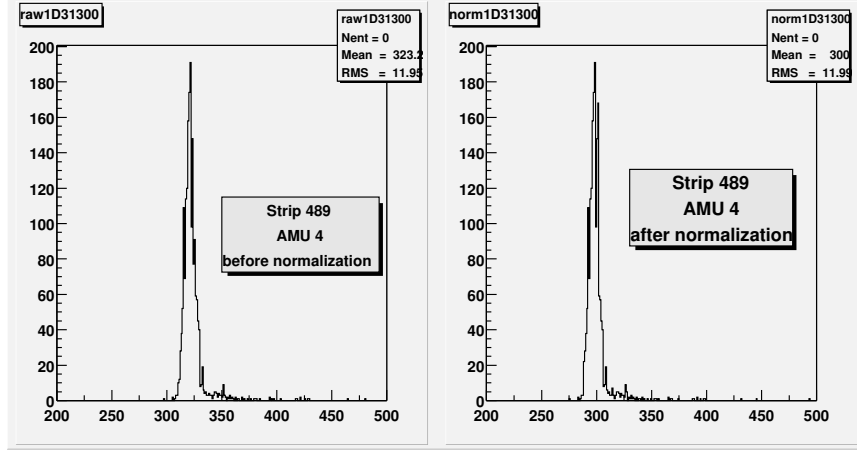


Figure 5.17: Normalization of Pedestals : (a) Raw, (b) After Normalization

Gaussian, we do not fit the distribution, rather record the mean of the distribution, which are 323.2. Then we look at all the events again and whenever there is an entry for strip 490 and AMU cell 4, we divide that ADC by 323.2, and multiply by 300. The resulting distribution from all events is shown in Fig. 5.17(b). The mean is here is 300 as expected.

The normalized plot of ADC vs AMU cell are shown in Fig. 5.18. The pedestal is

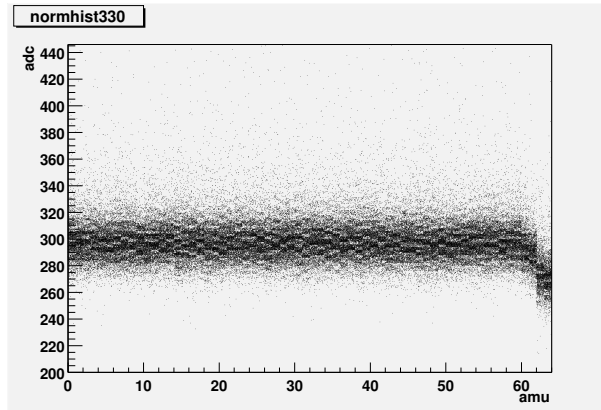


Figure 5.18: AMU vs ADC plot for Strip 330 after pedestal normalization

lined up at 300. But if we look at the plot we see that for  $\text{AMU cell} \geq 60$  still shows a perturbed behavior. This is seen in all 512 channels of data. Therefore we conclude that this is related to the properties of the last 4 AMU cells. The behavior of these cells are far from expected, even after the corrections. We therefore trim these entries from our analysis. But the question is if we ignore these entries how much statistics do we lose? Well the probability that a given AMU cell handles a signal is same as any other AMU cell, the probability is simply  $\frac{1}{64}$ . Thus if we ignore AMU cells  $\geq 60$ , we lose  $\frac{4}{64} \times 100\% = 6.25\%$  statistics, which is not a very large chunk of the statistics. Therefore, we decide to ignore entries for which  $\text{AMU cell} \geq 60$  throughout our analysis.

## 5.9 Event-by-event Pedestal Jumping

It was observed that the pedestals jump event to event. These jumping could be such that the pedestals can occupy the ADC range which could be that of a track, meaning the jumping pedestals can screen out the tracks. Therefore it is imperative that we identify the true pedestals before we proceed with any analysis. In the raw ADC distribution we see some high ADC. To see that whether the high ADC clusters are MIPs we do a simple test. We know that in an event if all the strips in a chip suddenly jumps to a high value, it is unlikely that the phenomenon is due to the hit from MIP producing tracks. And if this happens more than once or twice, it is a clear evidence that the jumps in ADC are not due to MIPs, rather it is due to some electronic problem. On the other hand, in the MVD active region we expect only a handful of strips to be hit by MIP producing tracks per event.

Let us test our idea for one sequence of a run. We randomly choose run 12397-0012 and look at the ADC vs strip event by event for high ADC clusters. We look at the difference between the ADC of any two consecutive strips. Since the probability of getting hit by a MIP producing track is low, and since we have a very wide pedestal

distribution, the difference of ADC between any two pairs should be very small, with the exception of when one of them gets hit by MIP, when the difference should be high, the frequency of which should be very low. Therefore we should expect a very narrow band if we plot ADC difference between any two neighboring pairs of strips as a function of the event number. Let us look at one of them.

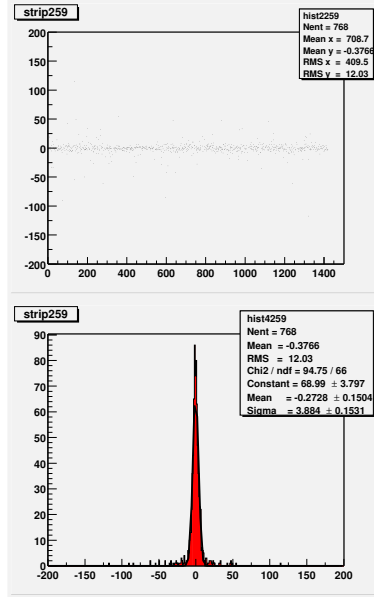


Figure 5.19: ADC Difference between strip 259 and 260. The top Plot is a plot of ADC Difference vs Event number, the bottom plot is 1-D plot of ADC Difference, fitted with a Gaussian

In the Fig. 5.19 we see that the difference in ADC between pairs are wide spread. It is a clear indication that the pedestals are jumping event-by-event. Also we can test in another way. We can find the difference between the first strip in a chip with all other strips in the chip. We should also expect narrow band if we plot the ADC difference with the event number. As examples we show plots for chips number 1 in Fig. 5.20.

So we are convinced that the pedestals are moving event-to-event. Then how about the clusters of high ADCs? Are they MIP or not? To test we just plot those

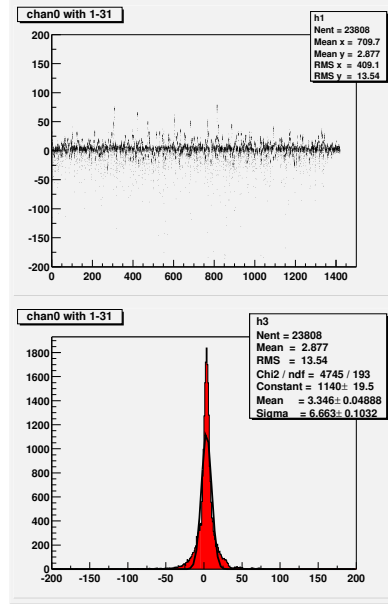


Figure 5.20: ADC Difference between strip 0 and strips 1-31. The top Plot is a plot of ADC Difference vs Event number, the bottom plot is 1-D plot of ADC Difference, fitted with a Gaussian

ADC values in event by event, an example is given in Fig. 5.21, where we have shown the ADC vs stripnumber plot for the high ADC clusters, in an event-by-event basis for events 416 and 417.

We look at the plot, especially for event number 416, we clearly see that in most chips all the channels got high ADC. If this was due to MIP, we should expect only a few of the strips attain high ADC, not all of them. This plot is another demonstration that pedestals are jumping. The high ADC clusters in the ADC vs strip plot do not necessarily represent MIPs, rather the plot demonstrates that they are the jumps of pedestals. We, therefore should look at alternate way to extract MIPs.

### 5.9.1 Event-by-event Correction

We have demonstrated in the previous subsection that the pedestals are moving in event to event. The clusters of high ADCs do not represent the MIPs, rather a jump

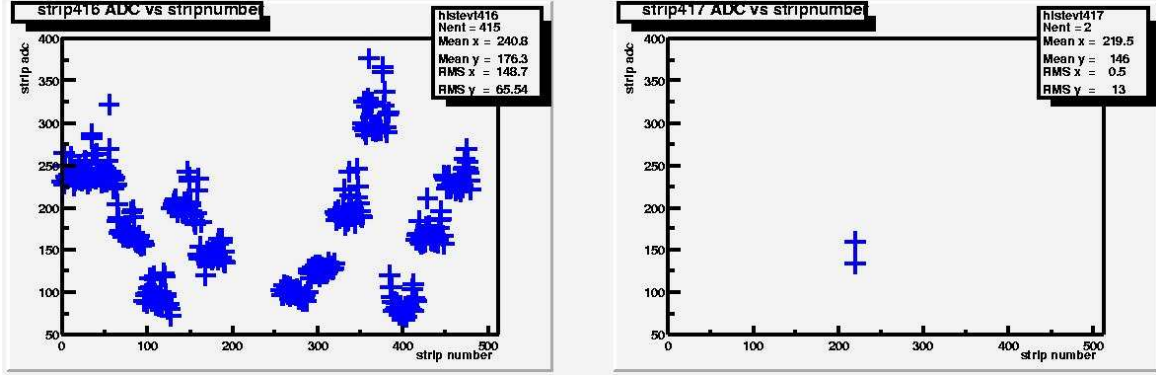


Figure 5.21: ADC of strips in Event number 416 and 417 for the high ADC clusters.

of the pedestals. We thus look at a way to extract MIP producing tracks.

If we look at the ADC vs strip plot in Fig. 5.12 or Fig. 5.13, there is no way to definitely conclude that a particular entry is due to a track. If there any MIP, they are “hiding” under the pedestals. So we have to “filter-out” the MIP tracks. Since the pedestals are moving event to event, we do the correction event by event. We need to identify the pedestals first and once they are identified we can subtract them. Our strategy is:

- In each event identify the *true* pedestals.
- Once identified, find the mean of the pedestal distribution. This mean contains the amount the pedestals *jumped* in that event.
- Then subtract the mean from all the measurements in that event. This will eliminate the pedestal jumping.

The trickiest part of this correction procedure is the pedestal identification. We should be very careful for pedestal identification. We therefore adopt an iterative procedure for the correction procedure:

- Step 1 : Find the lowest 30% of entries in an event for each chip (32 channels). These entries are undoubtedly pedestals. Plot them and get mean ( $m_1$ ) and

RMS ( $\sigma_1$ ).

- Step 2 : Extend the window. Find the entries those are less than  $m_1 + 2\sigma_1$ . Plot them and find mean ( $m_2$ ) and RMS ( $\sigma_2$ ).
- Step 3 : Extend the window even further. Find entries that are less than  $m_2 + 3\sigma_2$ . These are our identified pedestals. Plot them and get mean ( $m_3$ ).
- Step 4 : Subtract this mean from all ADCs.
- Step 5 : The process is repeated for all events.

## 5.10 Event-by-event Correction Procedure : Simulation

We have the procedure to do the event-by-event correction, that is to bring the jumping pedestals to the expected position. We now need to test whether the event-by-event correction procedure does what it is intended to do. To test that we do a very simple simulation. The experiment is called *Measuring Masses with a Scale*. The scale is such that it has an offset and the offset changes time to time. We measure two quantities on the scale, a block of 65 lb and a person of weight of 130 lb. This scenario resembles our whole ADC scenario : the analogy is between the jumping pedestals and the changing offset, the block and the person are analogous to the first and second MIP peaks.

Our experiment is as follows :

1. measure two quantities on a scale whose offset changes in each measurement.
2. Think of an *event* where we change the offset and record offset 10 times, and measure a block and a persons weight once. So each event has 12 entries.
3. Let us record 100 such events.

4. Pass the events through the event-by-event correction procedure.

If the procedure works, it will find the amount the offset changes in each event and subtract that from all measurements in the event. Therefore the output of the event-by-event correction procedure will result three delta like distribution for the three quantities. Fig. 5.22 shows the raw distribution. Fig. 5.23 shows the distribution

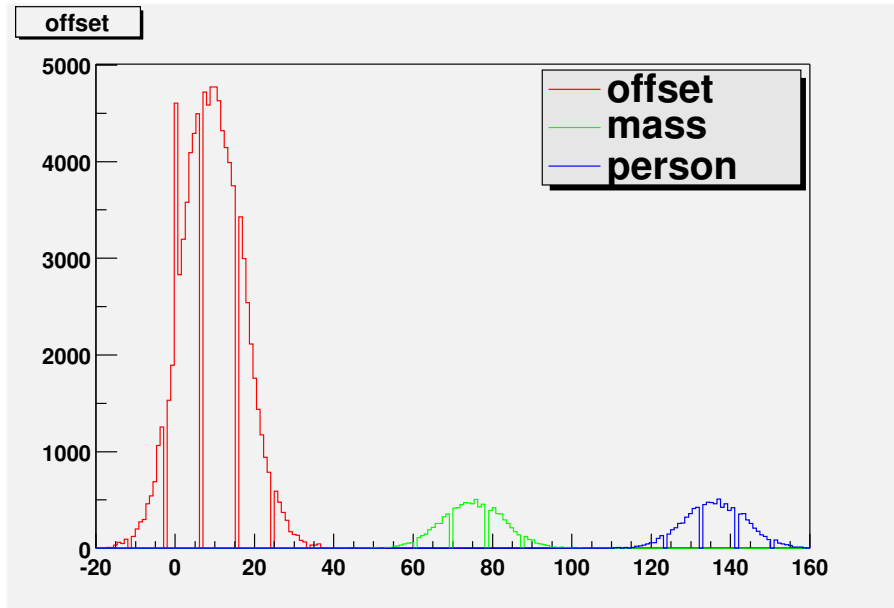


Figure 5.22: Raw Distribution

once the event correction procedure identifies the pedestals. But there is an inefficiency associated with the procedure. It fails to identify all the offset if the number of entries are high. Fig. 5.24 shows the distribution after offset subtraction. We see three delta like distribution. It proves that the procedure works. We apply to the procedure for the real data. In Fig. 5.25 we see the ADC distribution for the chip 1. We clearly see the MIPs in the plot.

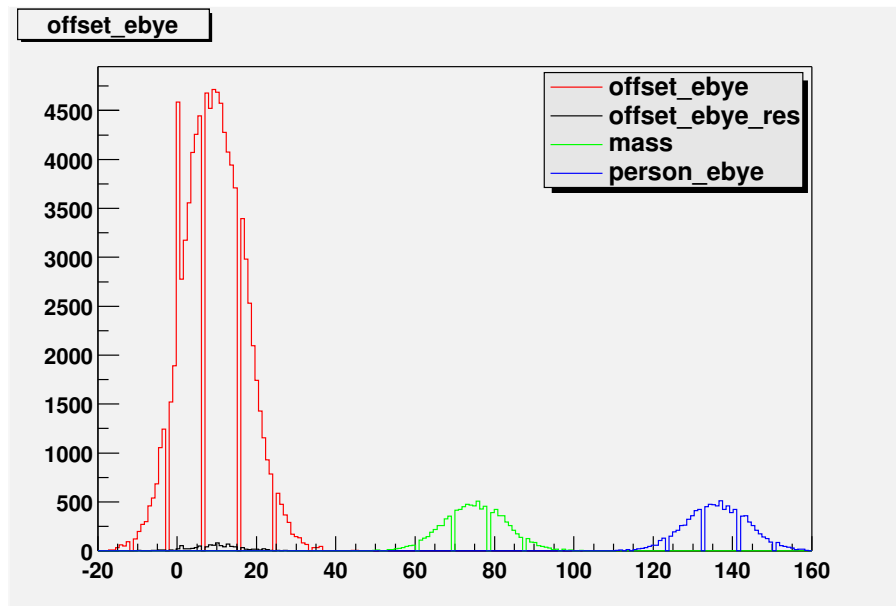


Figure 5.23: Distribution After Event-by-Event Pedestal Identification

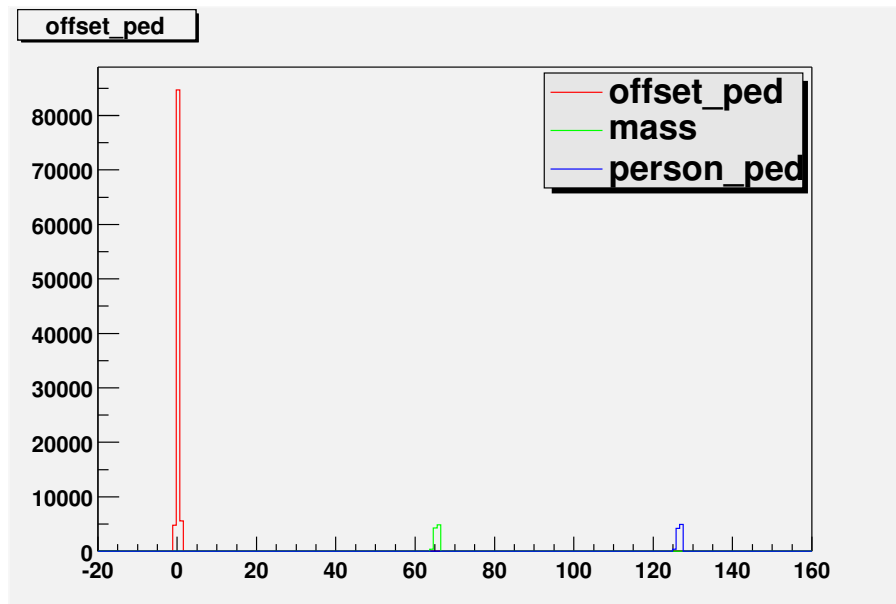


Figure 5.24: Distribution After Event-by-Event Pedestal Subtraction

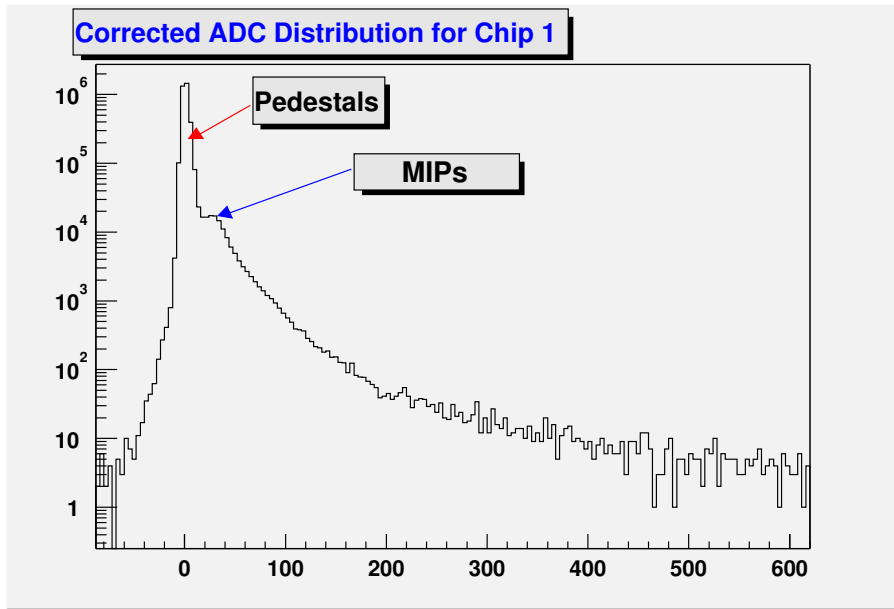


Figure 5.25: Corrected ADC distribution after AMU event by event jumping correction. The AMU cell corrections are also applied before the event by event jumping correction was applied.

## 5.11 Fitting of the Data

MVD detects particle by measuring the energy loss of incident particles in the silicon. Thus it is of utmost importance to study the energy loss spectrum. The theoretical (or empirical) description of the distribution depends on the thickness of the detector. By “thickness” we mean the actual physical thickness of the detector and the density of the material of the detector (the incident particle will “see” a denser medium as thicker).

When a charged particle passes through a detector, its passage is characterized by two main features : energy loss of the particle and the deviation from its initial trajectory. These are due to mainly these two processes:

- inelastic collisions with the electrons of the material
- elastic scattering from nuclei

These are cumulative process as long as the particle is inside the material and causes the particle to lose energy and deviate from its path. The inelastic collisions are almost solely responsible for the energy loss of heavy particles in matter. The atom in the particle absorbs energy in such collisions and becomes excited or ionized. Usually the energy loss per collision is very small. But in a dense matter the number of collisions per unit length is very large. The particle therefore departs a considerable amount of its energy in the medium. Therefore, the energy loss distribution depends on the number of collisions the particle encounters during its passage through the material of the detector. We need to find the probability  $f(x, \Delta)$ , of the energy loss  $\Delta$  in a sample of thickness  $x$ . We thus categorize the energy loss distribution depending on the thickness of the detectors:

### 5.11.1 Thick Detectors

For the energy loss distribution in a thick detector, we can use the central-limit theorem to find out what the shape of the distribution should be. The Central Limit Theorem says that if  $S_n$  is the sum of  $n$  mutually independent random variables, then the distribution function of  $S_n$  is well-approximated by a certain type of continuous function known as a normal density function, which is given by the formula

$$f_{\mu, \sigma}(x) = \frac{1}{\sqrt{2\pi}\sigma} e^{-(x-\mu)^2/(2\sigma^2)} \quad (5.14)$$

The Central Limit Theorem tells us, quite generally, what happens when we have the sum of a large number of independent random variables each of which contributes a small amount to the total.

We can readily see what type of distribution will it be in case of a thick detector. We can take our random variable to be  $\delta E$ , the energy loss in the medium due to a single collision. Then  $f(x, \Delta)$  is given by,

$$f(x, \Delta) \propto \exp\left(\frac{-(\Delta - \bar{\Delta})^2}{2\sigma^2}\right) \quad (5.15)$$

The spread  $\sigma$  is calculated by Bohr[41] for the non-relativistic heavy particles as:

$$\sigma_0^2 = 0.1569 \rho \frac{Z}{A} x \text{ MeV}^2 \quad (5.16)$$

where  $\rho, Z, A$  are density, atomic number and atomic weight of the material. For relativistic particles we have

$$\sigma^2 = \frac{1 - \frac{1}{2}\beta^2}{1 - \beta^2} \quad (5.17)$$

### 5.11.2 Thin Detectors

In a thin medium the number of collisions  $N$  is not too large. Therefore the central limit theorem is no longer applicable in this type of situation. The fact that in a thin material the total energy loss is given by a small amount of interactions, each one with a very wide range of possible energy transfers, determines a characteristic shape of the energy loss distribution. Landau[42] derived a formula for such a distribution. He made two assumptions to derive his formula:

1. the typical energy loss in the sample should be large compared to the binding energy of the most tightly bound electron,
2. the energy loss should be small compared to the maximum energy loss in a single collision.

The landau formula can be written in a closed analytical form as:

$$f(\lambda) = \frac{1}{\sqrt{2\pi}} \exp \left[ -\frac{1}{2} (\lambda + \exp(-\lambda)) \right] \quad (5.18)$$

where the reduced energy variable  $\lambda$  represents the normalized deviation from the most probable energy loss  $\Delta_{mp}$ :

$$\lambda = \frac{\Delta - \Delta_{mp}}{\xi} \quad (5.19)$$

where  $\xi$  is approximated, for most purposes, by taking the first multiplicative term in the Bethe-Bloch formula

$$\xi = K \rho \frac{Z}{A} \frac{z^2}{\beta^2} x \quad (5.20)$$

### 5.11.3 Very Thin Detectors

The Landau approach fails to explain the energy loss curve for a very thin detector. By very thin detectors we mean absorber widths about  $10\text{mg/cm}^2$ , which is typical for gas proportional counters and chambers. The main features of energy loss curves are :

- $\Delta_{mp}$  : the most probable value corresponding to the maximum of a fluctuation curve,
- $\delta$  : relative half width, which is a full width at a half maximum, fwhm, divided by  $\Delta_{mp}$ .

Many detectors filled with rare gases with additions of 5-10% of  $\text{CH}_4$  or  $\text{CO}_2$  showed that  $\delta$  values are considerably greater and the  $\Delta_{mp}$  values are somewhat lower[34] than the Landau theory predictions. The measured relativistic rise of the most probable ionization was found to be 10-20% lower than that was expected according to this theory corrected for density effect[43].

Ermilova el.al[34] came up with a Monte Carlo calculation for the modification of the Landau function for small thickness detectors. Their analysis was found to accounts for the broadening of the landau curve. To do the analysis, the modified to Moyal function[44] as:

$$f(\lambda) = a_1 \exp \{-a_2(\lambda + a_5\lambda^2) - a_3 \exp [-a_4(\lambda + a_6\lambda^2)]\} \quad (5.21)$$

where  $a_1 \dots a_6$  are the parameters found by fitting and doing  $\chi^2$  minimization.

### 5.11.4 Is MVD a Thin or Very-Thin Detector?

We are in a position to ask ourselves is MVD Thin or Very Thin? MVD is silicon detector with a thickness of 0.03cm. So it seems that we should consider it Very-Thin

and use the modified Moyal Function to describe the energy loss distribution. But is it really Very Thin?

If we look in reference [3], They tell that the modified Moyal Function explains the energy loss distribution from Gas Detectors for *absorber widths* about 10 milligrams/cm (*absorber widths* is the density of the gas times the detector width). Let us calculate some typical parameters:

Material	density mg/cc	Thickness cm	density.Thickness mg/cm <sup>2</sup>
Ar	1.3960	5	6.98
CH <sub>4</sub>	0.4224	5	2.112
He	0.1249	5	0.6245
Si	2330	0.03	69.9

Looking at the above table we see that a 0.03cm thick Si detector is as thick as 50cm of Ar or 165cm of CH<sub>4</sub> or 560cm of He. Therefore the Very-Thin approximation does not hold for our detector. We should treat MVD as Thin Detector. But we can not simply describe the energy loss curve by a Landau Distribution, since the detector has some resolution (or smearing) of the measurement. We should therefore use a Landau function convoluted with a Gaussian to describe the energy loss distribution in MVD.

### 5.11.5 Energy Loss Distribution in MVD

MVD employs very thin (<300  $\mu\text{m}$ ) silicon detectors and low noise electronics in order to achieve high spatial resolution and to detect change in charged particle multiplicity. Under these conditions, there is a significant deviation from the landau theory, since we cannot neglect the atomic electron binding energy. Also there is some resolution associated with the measurement made in the detector. The modified energy loss distribution can be expressed by a convolution of a Landau function with a Gaussian function:

$$f(\Delta, x) = \int f_{\text{landau}}(\tau, x) f_{\text{gaus}}(\Delta - \tau) d\tau \quad (5.22)$$

## Convolution of a Landau with a Gaussian Function

We use ROOT to calculate the convolution. The landau function, although can be generated, we use the Landau distribution in ROOT, represented by the CERNLIB approximation. But we need to make a simple modification of the function. The maximum is located at  $x=-0.22278298$  with the location parameter=0. This shift is corrected within our function, so that the actual maximum is identical to the most probable parameter. For the Gaussian Function we use the following expression:

$$f(x) = \frac{1}{\sqrt{2\pi}\sigma} \exp \left[ -\frac{1}{2} \left( \frac{x - \bar{x}}{\sigma} \right)^2 \right] \quad (5.23)$$

In ROOT we perform integration by summation. The simple relation between direct integration and integration by summation can be written as:

$$\int_a^b f(x)dx \approx \lim_{n \rightarrow \infty} \sum_{i=1}^n f(c_i)\Delta x_i \quad (5.24)$$

where

$$\begin{aligned} \Delta x_i &= \frac{b-a}{n} \\ c_i &= a + \frac{b-a}{n}i, \quad i = 1, 2, \dots, n \end{aligned}$$

Therefore for a Landau function  $L(x, mpv, \sigma_1)$ , of Most Probable Value  $mpv$  and the width  $\sigma_1$  and a Gaussian function  $G(x, \bar{x}, \sigma_2)$ , of mean  $\bar{x}$  and the RMS  $\sigma_2$ , the convolution integration is given by

$$L * G = \int_a^b L(\tau, mpv, \sigma_1)G(x - \tau, \bar{x}, \sigma_2)d\tau \quad (5.25)$$

which can be approximated as:

$$\begin{aligned} \int_a^b L(\tau, mpv, \sigma_1)G(x - \tau, \bar{x}, \sigma_2)dx &\approx \lim_{n \rightarrow \infty} \sum_{i=1}^n L(c_i, mpv, \sigma_1)G(x - c_i, \bar{x}, \sigma_2)\Delta \tau_i \\ \Delta \tau_i &= \frac{b-a}{n} \\ c_i &= a + \frac{b-a}{n}i, \quad i = 1, 2, \dots, n \end{aligned}$$

But

$$\begin{aligned} G(x - c_i, \bar{x}, \sigma_2) &= \frac{1}{\sqrt{2\pi}\sigma_2} \exp \left[ -\frac{1}{2} \left( \frac{x - (\bar{x} - c_i)}{\sigma_2} \right)^2 \right] \\ &= G(x, \bar{x} - c_i, \sigma_2) \end{aligned}$$

Now to fit the data, we need the initial parameters. We need to supply four parameters:

- Gaussian width  $\sigma_2$
- Landau MPV,
- Landau width  $\sigma_1$
- Total Area (Normalization constant) of the fit

How do we get the parameters? Well, the RMS of the Gaussian is basically the detector resolution. In order to get the detector resolution, we look at the pedestal distribution. In the perfect world the pedestals should all be zero. So we should expect a perfect  $\delta$ -function at zero. But the world is not perfect so is the detector. Therefore, the pedestals will follow a Gaussian distribution. The width of the pedestal will therefore be the detector resolution. For the other three parameters, we do the following. We fit the neighborhood of the peak in the track distribution with a simple Landau. We record the constant, MPV and width of the fit. We supply these numbers as the initial parameters for the landau part of the convolution.

Our data has both pedestal and the tracks in it. Therefore, the total distribution is simply a sum of a Gaussian fitting the pedestal and a convolution of Gaussian and pedestal to fit the tracks. Symbolically which can be expressed as:

$$\text{Total} = \text{Gaussian} + \text{Landau} * \text{Gaussian} \quad (5.26)$$

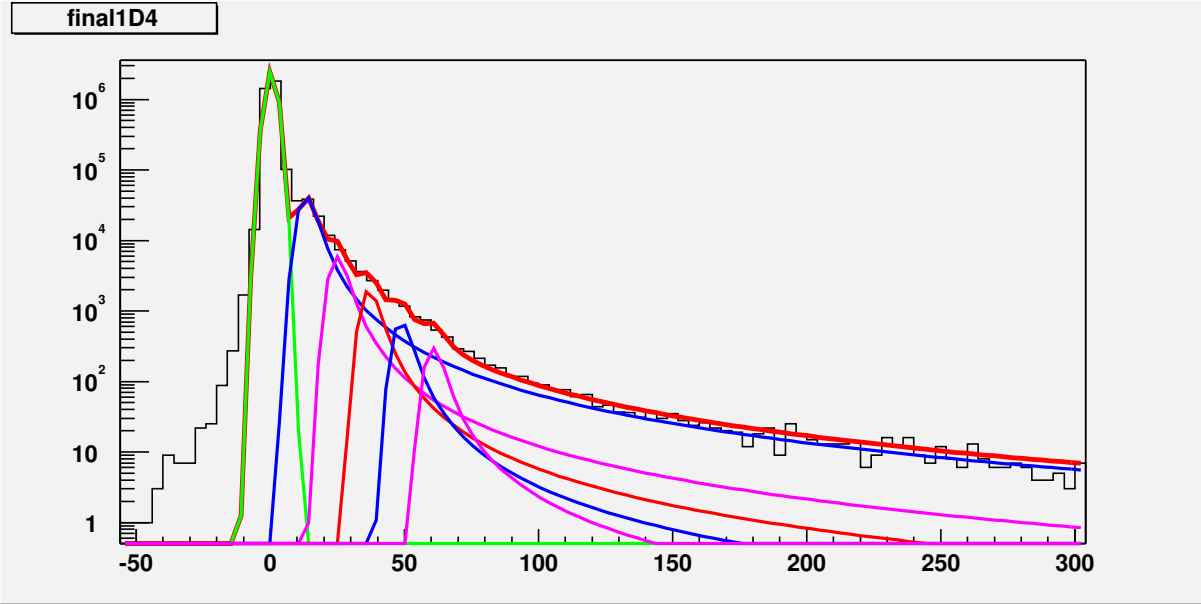


Figure 5.26: Fitting of Data. The corrected data is fitted with a Gaussian function for the pedestal and a Landau convoluted with a Gaussian for the MIPs.

### 5.11.6 Fitting Example

With the fitting procedure outlined above we now show an example of the fitting of data. As mentioned, the data points consists of pedestals and the tracks. As an example we show the fitting of chip 4 in Fig. 5.26.

The fitting was done in several steps. The first step is to fit the pedestals. The pedestals are fitted with a Gaussian. The mean of the fitting should be zero, as we expect that the pedestals be normalized at zero. Although we tried to correct the fluctuations of ADC due to amu cells and eliminate the pedestal jumping, there still are some effects. That is why the pedestal distribution has a little deviation from a perfect Gaussian. The means of the fittings were found a little away from zero. We will incorporate this very small offset in our subsequent measurement of the track MPV positions. The width of the fit is the resolution of the measurement in the detector and will be used in all the convolutions.

Beyond the Gaussian we have the tracks. As describes in the previous subsection,

we zoom-in the track region to find the peaks. Once we find the peak, we get a rough estimate of the MPV and width by fitting with a landau. Then we convolute a landau with a Gaussian of fixed width, the Gaussian fixed width being the width of the pedestal fitting. We play with the landau width to get the best possible fitting of the peak in track region. We use all the parameters from the pedestal fit and the track fit to fit the total distribution. It is seen that the total fit is a good fit at the pedestal and near the peak in the track region, but it is not a good fit away from the track peak at its right. The total fit falls off from the data point. This is an indication that the peak we found and fitted is due to one track passing through one strip and there are entries at the right of the peak that are due to more than one track going through one strip. Since the minimum ionizing tracks departs almost equal amount of charge (which is converted to ADC), we look for peaks at multiples of track1 MPV minus the mean of pedestal. After zooming in these regions we indeed see some tiny peaks. Therefore we try to fit the 2-tracks with the constraints that the MPV of these 2-tracks are twice that of MPV of 1-track minus the mean of pedestal. As usual we keep the Gaussian width fixed and play with the same landau width as the 1-track. After fitting the total distribution is seen to be pushed upward. It fits well in the pedestal+1-track+2-track region, but still not a good fit at the right of the 2-track. Therefore we continue with 3-tracks, 4-tracks, 5-tracks until we get a very good fit of the total.

## 5.12 Strategy to Calculate $dN/d\eta$

Once we fit the data we are in a position to select tracks. But if we look at the fitting plots in Fig. 5.27, we see that the fitting of the pedestals, 1-track, 2-tracks etc are all overlapping. There is no way to distinguish that a given ADC is really a 1-track or 2-track or a pedestal. But depending on the value of the ADC and the fitting we can assign a weight to the ADC whether it is a pedestal, or a 1-track or a 2-track or

something else.

To elaborate the procedure let us look at the fitting of the data once again. In figure below we show the different regions of interest by dotted lines. In each region,

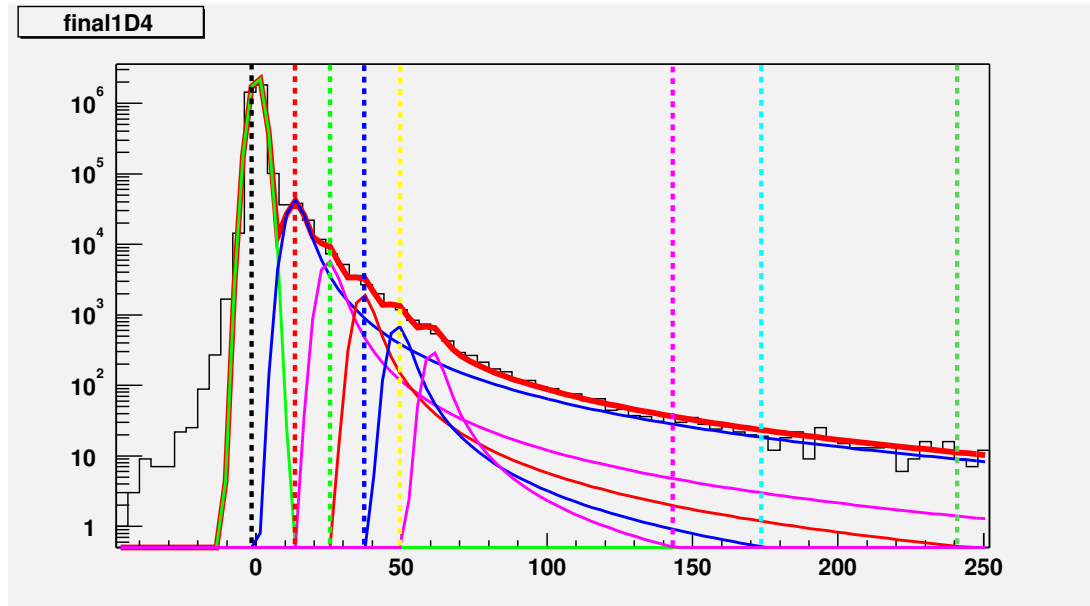


Figure 5.27: Fitting of Data Showing the Different Region of Integration

we find the integral (area under the curve) of each fitting functions. Say in a given region we have the following:

$I_0$  = Area under pedestal curve

$I_1$  = Area under 1track curve

$I_2$  = Area under 2track curve

$I_3$  = Area under 3track curve

$I_4$  = Area under 4track curve

$I_5$  = Area under 5track curve

Then the probability that a given ADC in that region is

$$\text{a pedestal is } p_0 = \frac{I_0}{I_0 + I_1 + I_2 + I_3 + I_4 + I_5}$$

$$\begin{aligned}
\text{a 1track is } p_1 &= \frac{I_1}{I_0 + I_1 + I_2 + I_3 + I_4 + I_5} \\
\text{a 2track is } p_2 &= \frac{I_2}{I_0 + I_1 + I_2 + I_3 + I_4 + I_5} \\
\text{a 3track is } p_3 &= \frac{I_3}{I_0 + I_1 + I_2 + I_3 + I_4 + I_5} \\
\text{a 4track is } p_4 &= \frac{I_4}{I_0 + I_1 + I_2 + I_3 + I_4 + I_5} \\
\text{a 5track is } p_5 &= \frac{I_5}{I_0 + I_1 + I_2 + I_3 + I_4 + I_5}
\end{aligned}$$

Therefore, the number of tracks associated with an ADC is

$$n = 0.0 \times p_0 + 1.0 \times p_1 + 2.0 \times p_2 + 3.0 \times p_3 + 4.0 \times p_4 + 5.0 \times p_5 \quad (5.27)$$

As an example we show the probabilities in the table below for the ADCs in chip 4:

Region	From	To	$p_0$	$p_1$	$p_2$	$p_3$	$p_4$	$p_5$
1	-100	1.26	1	2.31015e-08	0	0	0	0
2	1.26	12.27	0.976944	0.0230557	1.54387e-09	0	0	0
3	12.27	12.95	3.35293e-06	0.999996	1.10999e-06	0	0	0
4	12.95	26.05	6.39073e-08	0.889741	0.110259	5.82071e-07	0	0
5	26.05	36.84	5.29473e-32	0.391315	0.461379	0.147305	1.01379e-07	0
6	36.84	48.8	1.32924e-64	0.325616	0.13547	0.424371	0.114542	9.66449e-08
7	48.8	145.79	1.28707e-115	0.479535	0.111012	0.0839567	0.192791	0.132706
8	145.79	176.0	0	0.782183	0.12962	0.0522986	0.0233957	0.0125026
9	176.0	244.0	0	0.794413	0.126363	0.0485358	0.0204837	0.0102048
10	244.0	384.0	0	0.806014	0.122811	0.0448889	0.017913	0.00837238
11	384.0	400.0	0	0.811428	0.121005	0.0431726	0.0167779	0.0076166

For an estimation of how many tracks are there in the chip 4, we count the number of entries in each region and find the number of entries as candidates for pedestals, 1-track, 2-tracks etc. The entries are tabulated below:

Region	From	To	pedestals	1-track	2-tracks	3-tracks	4-tracks	5-tracks
1	-100	1.26	1445490	0	0	0	0	0
2	1.26	12.27	1923710	45399	0	0	0	0
3	12.27	12.95	0	0	0	0	0	0
4	12.95	26.05	0	64119	7945	0	0	0
5	26.05	36.84	0	6297	7425	2370	0	0
6	36.84	48.8	0	1988	827	2591	699	0
7	48.8	145.79	0	2753	637	482	1107	762
8	145.79	176	0	159	26	10	4	2
9	176	244	0	109	17	6	2	1
10	244	384	0	175	26	9	3	1
11	384	400	0	20	3	1	0	0
ALL	-100	400	3369200	121019	16906	5469	1815	766

We have 512 active silicon strips. To measure the charged particle multiplicity we adopt the following strategy.

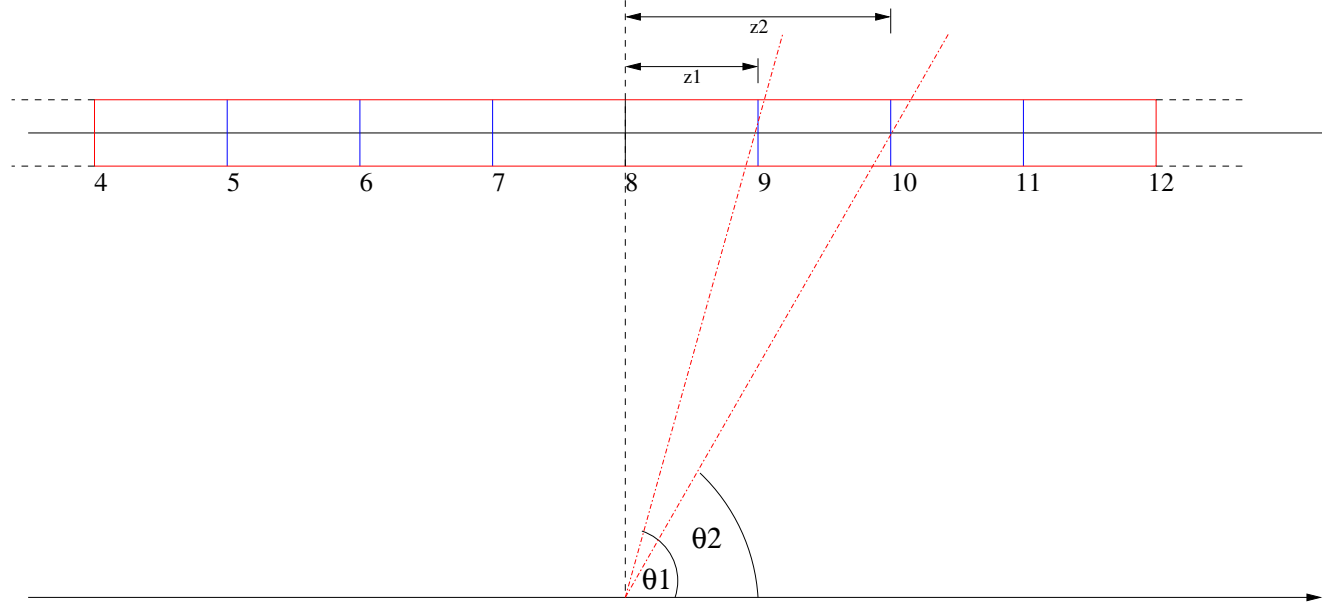


Figure 5.28: A part of the MVD: Strategy to Calculate  $\eta$  of Strips

1. Look the total active region into 16 chips, each containing 32 strips. Since each strip in a chip behave in a similar fashion and chips behavior varies from chip to chip, it is a good idea to consider one chip at a time instead of looking into the total MVD active region at a time. Each strip occupies a length of  $0.02 \times 32\text{cm}$  in  $z$ . It has a thickness of  $0.03\text{cm}$  and covers  $-30^\circ$  to  $30^\circ$  in  $\phi$ . Let us denote these strips by  $kk = 0, 1, \dots, 15$ .
2. For each chip we calculate the  $z$ -position of the beginning and the end of the strip. Let's call these  $z$ -positions as:  
 $z_1 \equiv z$ -position of the beginning of the bin  
 $z_2 \equiv z$ -position of the end of the bin

For each of the strips we calculate  $\theta_1$  and  $\theta_2$  by using the following relations:

$$\theta_1[kk] = \tan^{-1} \left[ \frac{4.985}{(z_1[kk] - \text{vertexBBC})} \right] \quad (5.28)$$

$$\theta_2[kk] = \tan^{-1} \left[ \frac{4.985}{(z_2[kk] - \text{vertexBBC})} \right] \quad (5.29)$$

where we have taken the distance of the MVD barrel from the collision point to be 4.985 cm. We thereby calculate  $\eta$  as :

$$\eta_{min}[kk] = -\log \left[ \tan \left( \frac{\theta_1[kk]}{2} \right) \right] \quad (5.30)$$

$$\eta_{max}[kk] = -\log \left[ \tan \left( \frac{\theta_2[kk]}{2} \right) \right] \quad (5.31)$$

$$(5.32)$$

Therefore,

$$d\eta[kk] = \eta_{max}[kk] - \eta_{min}[kk] \quad (5.33)$$

$$\eta[kk] = \frac{\eta_{max}[kk] + \eta_{min}[kk]}{2} \quad (5.34)$$

3. Now in each chip whatever ADC value we get, we assign a weight in accordance with the Eq.(5.27). We then loop over the event and find how many of the tracks are there in the chip. The total of all tracks in the chip in that event is  $dN[kk]$ .
4. for each chip, we calculate  $dN/d\eta$  by using the following equation

$$\frac{dN}{d\eta} = \frac{dN[kk]}{d\eta[kk]} \quad (5.35)$$

5. To plot the  $\frac{dN}{d\eta}$  vs  $\eta$  for the chips, we plot  $\frac{dN[kk]}{d\eta[kk]}$  vs  $\eta[kk]$ .

## 5.13 Length Correction and Multiple Counting of Tracks Correction

During the collision, there are numerous occasions when a track will pass through more than one strip. This due to the angular position of the strip from the vertex

position. The algorithm to count the multiplicity is such that we look at the ADC value from a strip and then make a decision that whether the ADC value is due to one track in the strip or more than one track. We, at this point need to make a correction of the fact that one track may pass through more than one strip. Then the strips the track pass through will output an ADC value which is proportional to the path-length of the track in the strip. All the strips that got hit by the same track may have enough ADC that all of them may claim that they saw one MIP. If there are  $n$  such strips, we will count that in that event we have  $n$  tracks. But in reality it is only one track. We need to correct this multiple counting of one track. This effect is due to the path-length of the track from the vertex position and angle of incidence on the MVD strips.

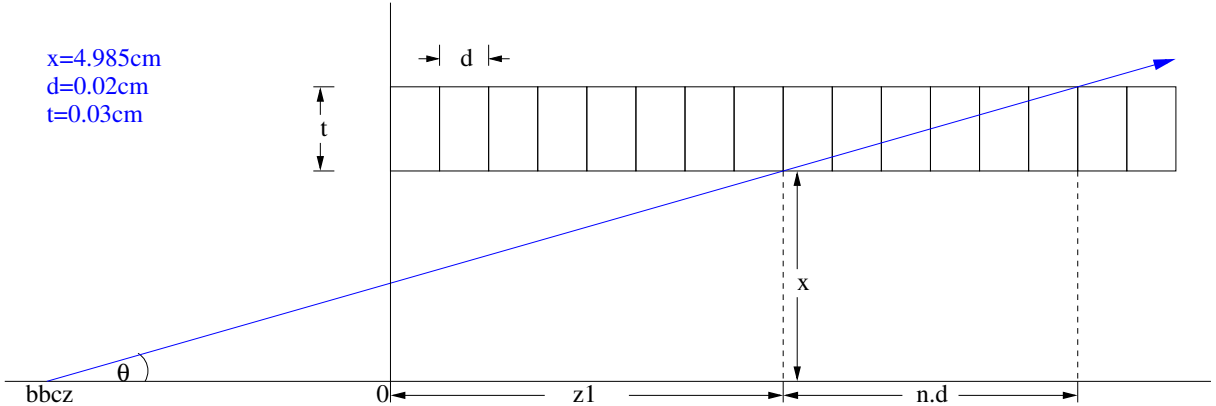


Figure 5.29: A track passing through a number of Strips

Let us look at the Fig. 4.31. The collision vertex at  $bbc z$ . The tracks makes an angle of  $\theta$ . It passes through  $n$  strips. The MVD strips are at 4.985cm from the beam-axis. Each of the strips covers 0.02cm in  $z$ -direction and has a thickness of 0.03cm. The number  $n$  can be determined from the vertex position and the position of the strip.

$$\sin \theta = \frac{x}{z_1 - bbc z} = \frac{x + t}{(z_1 - bbc z) + nd} \quad (5.36)$$

from which we can find  $n$ :

$$n = \frac{t}{d} \frac{1}{x} (z_1 - bbcz) \quad (5.37)$$

Using the values for  $n, t$  and  $d$ , we find that

$$n = 0.301(z_1 - bbcz) \quad (5.38)$$

Let us make an estimate as how large the number  $n$  may be. Lets think for instance that the collision occurs at  $bbc z = -20\text{cm}$ . It comes at MVD at the position of the, say 256th strip, which has  $z_1 = 5.39\text{cm}$ . Then using the expression of  $n$  we find that  $n$  will be 7.64. So the effect of incident is large.

How to make this correction? Let us look at the first strip that got hit. From the figure we see that

$$\tan \theta = \frac{y_1}{d}, \quad (5.39)$$

where  $y_1$  is the position along thickness  $t$  where the track leaves the strip.

Also

$$\tan \theta = \frac{t}{nd} \quad (5.40)$$

From the above two equations we find that

$$y_1 = \frac{t}{n} \quad (5.41)$$

Therefore the path-length of the track inside the strip is

$$r_1 = \frac{\sqrt{t^2 + n^2 d^2}}{n} \quad (5.42)$$

Now if a track passes straight through the strip, it produces a 1-mip. That is, if the path-length of the track inside the strip is about equal to  $t$ , it will deposited charge (which is converted to ADC) is proportional to, roughly, 1-mip. Therefore a path-length of  $r_1$  inside the strip will generate an ADC which will be proportional to

$$N_{1_{uncorrected}} = \frac{\sqrt{t^2 + n^2 d^2}}{nt} \quad (5.43)$$

MIPs. We can make an assumption that when a track passes through  $n$  strips, the path-length in each strip are almost the same. Therefore, we will count, after the end of the event, that this particular track is miscounted as

$$dN_{uncorrected} = n \cdot N_{1_{uncorrected}} = \frac{\sqrt{t^2 + n^2 d^2}}{t} \quad (5.44)$$

Experimentally,  $dN_{uncorrected}$  is the sum of the ADC measured in the strips in that event.

Now

$$\sin \theta = \frac{t}{\sqrt{t^2 + n^2 d^2}} \quad (5.45)$$

Therefore the correction factor is just  $\sin \theta$ :

$$dN_{corrected} = dN_{uncorrected} \times \sin \theta \quad (5.46)$$

So we simply measure the ADC of the strips and multiply the ADC by  $\sin \theta$ .

## 5.14 $dN/d\eta$ in MVD

Once we have selected the tracks we can measure the charged particle multiplicity in MVD.

We first look the number of tracks in the MVD divided by the  $\eta$ -coverage of the MVD. Also we plot for different centralities on the same plot in Fig. 5.30.

The shape of the measured charged particle multiplicity spectrum shows the characteristic form of multiplicity distributions in limited apertures[36] : a peak and a sharp drop off at low values of  $dN/d\eta$  corresponding to peripheral collisions with grazing impact; a broad, gently sloping plateau at the midrange of impact parameters, dominated by the nuclear geometry; and then at higher values of  $dN/d\eta$  , which correspond to the most central collisions where the nuclei are fully overlapped, a knee leading to a falloff which is very steep for large apertures and which becomes less steep, the smaller the aperture[22].

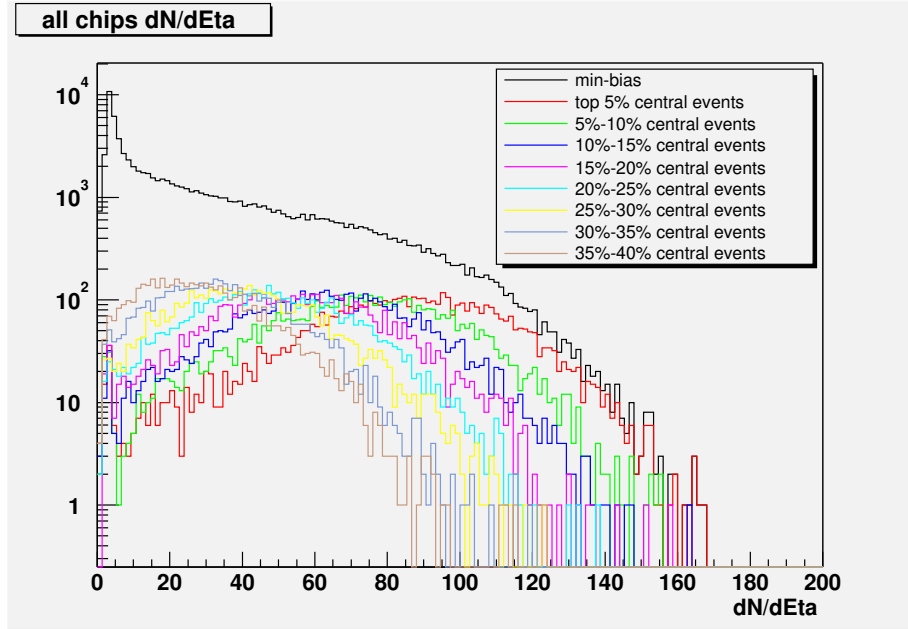


Figure 5.30:  $dN/d\eta$  in the MVD Active Region. Here the min. bias distribution is plotted together with the distribution for the centrality classes 0%-5%, 5%-10%, 10%-15%, 15%-20%, 20%-25%, 25%-30%, 30%-35%.

We now plot the profile histogram of  $dN/d\eta$  vs  $\eta$  for the minimum bias events in Fig. 5.31:

## 5.15 Acceptance Correction and Results

Before we proceed to compare our result with models, we first need to make a correction for the acceptance. As mentioned earlier, MVD has a coverage between  $z=0$  cm and  $z=10.6$  cm and  $57^\circ$  in azimuth. Therefore we need to make a correction of the multiplicity measured in MVD.

In order to make the correction we make use of a Monte-Carlo. The generated particles are pions random in rapidity  $y$  and azimuth  $\phi$  and exponential in the transverse mass  $m_T$  at temperature  $T$ .

$$-3 < y < 3$$

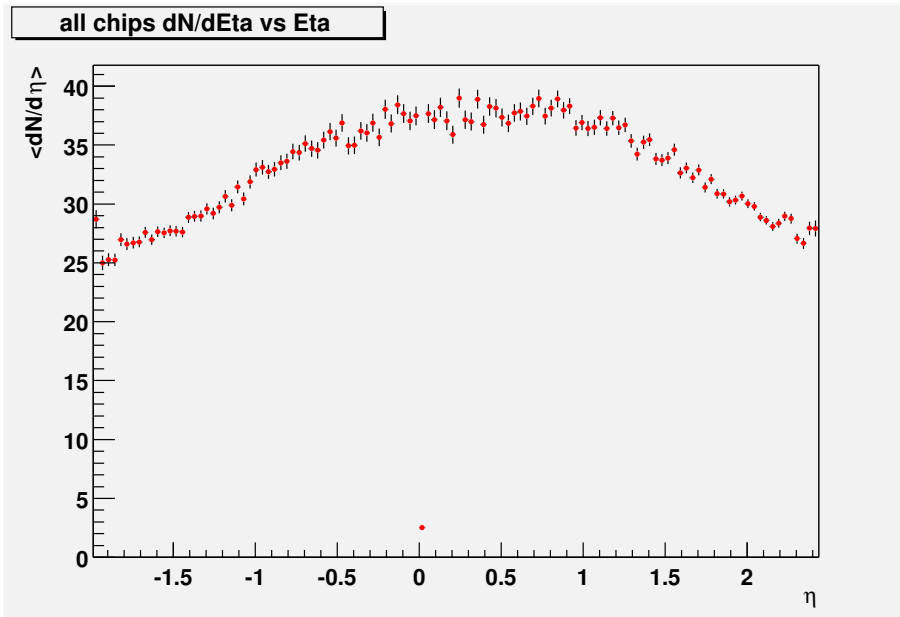


Figure 5.31: Average  $dN/d\eta$  vs  $\eta$  for minimum-bias Events

$$\begin{aligned}
 0 &< \phi < 2\pi \\
 \frac{1}{m_T} \frac{dm_T}{dy} &= \exp -(m_T - m_0)/T
 \end{aligned}$$

We generate 1000 events. In each event there are 1000 particles per unit rapidity. We then see how many of the generated particles are detected in the MVD active region. The input pseudorapidity ( $\eta$ ) distribution and the  $\eta$  distribution of the detected particles are seen to be as below for temperature  $T = 220$  MeV:

The corrections are applied for all the analysis described in all subsequent sections. It is noted that there is a *skewing* in the accepted pseudorapidity Distribution. This is due to the physical coverage of MVD active region. MVD active region is located between  $z = 0.09$  cm and  $Z = 10.51$  cm. For example if the  $z$ -vertex is between -25 cm and +25 cm, then due to the coverage the pseudorapidity coverage will be between -2.31185 and 2.66142. So there will be more pseudorapidity in the positive than negative.

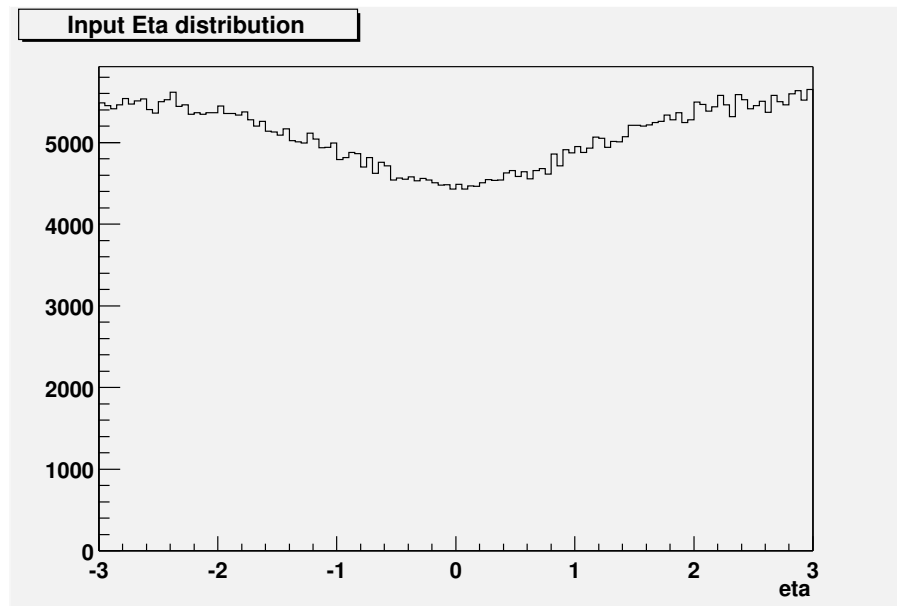


Figure 5.32: Input  $\eta$  Distribution

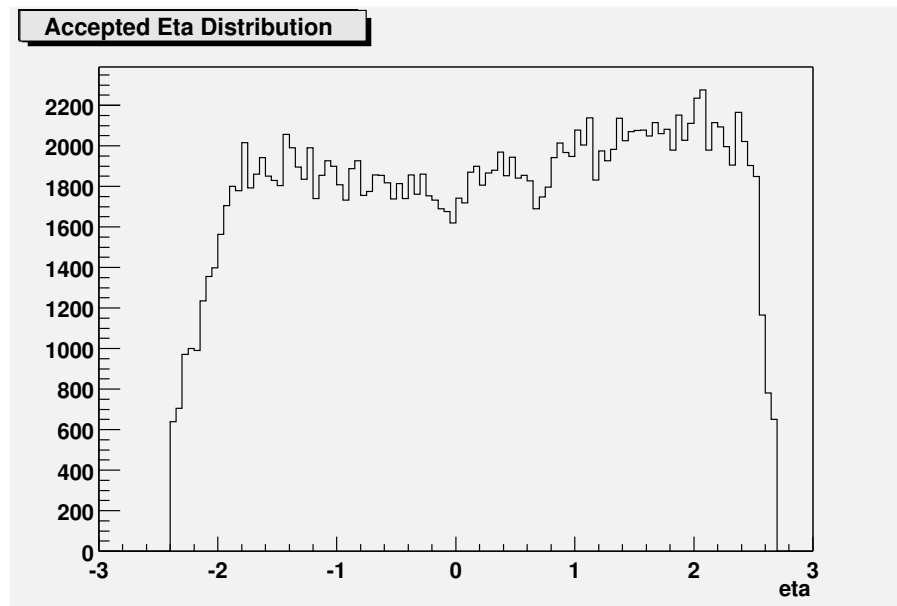


Figure 5.33:  $\eta$  Distribution of the tracks accepted in MVD active Region

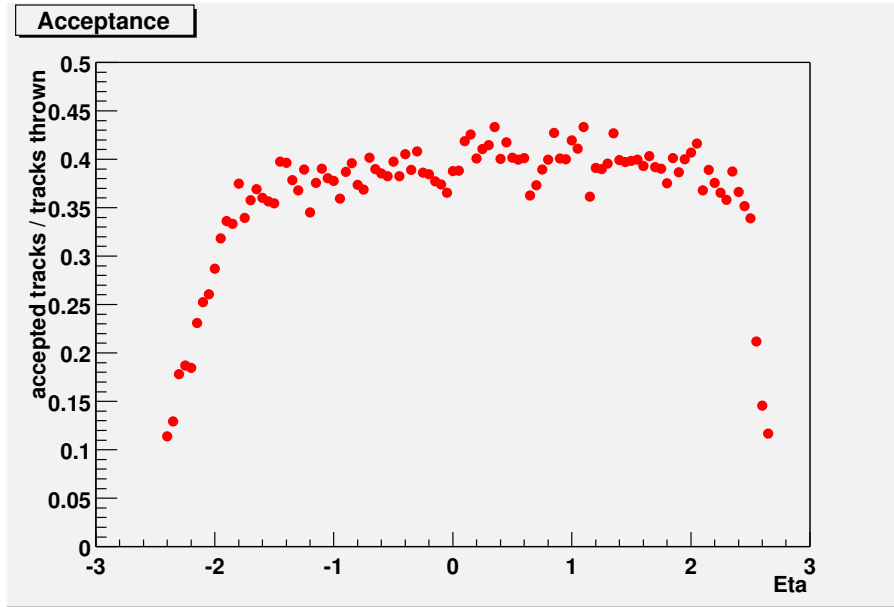


Figure 5.34: Acceptance in MVD

## 5.16 Systematic Errors

The main contribution for the systematic error arises from the assignment of weight to the tracks. We have assigned weight to any ADC as shown in the Eq. 5.27 Now, depending on the fitting of the ADC distribution we have counted the number of tracks to be a 1-track, 2-tracks and so on.

The error comes in as follows. Say an ADC is really due to 2-tracks. But we are assigning it as Eq. 5.27 Therefore we are undercounting the track by an amount of

$$e_2 = -1.0p_1 + 0.0p_2 + 1.0p_3 + 2.0p_4 + 3.0p_5 \quad (5.47)$$

If we have  $N_2$  such tracks in  $N$  number of tracks, the error in 2-tracks is:

$$err_2 = (-1.0p_1 + 0.0p_2 + 1.0p_3 + 2.0p_4 + 3.0p_5) \times \frac{N_2}{N} \times 100\% \quad (5.48)$$

But  $\frac{N_2}{N} = p_2$ . Therefore,

$$err_2 = (-1.0p_1 + 0.0p_2 + 1.0p_3 + 2.0p_4 + 3.0p_5) \times p_2 \times 100\% \quad (5.49)$$

Similarly,

$$\begin{aligned}
 err_3 &= (-2.0p_1 - 1.0p_2 + 0.0p_3 + 1.0p_4 + 2.0p_5) \times p_3 \times 100\% \\
 err_4 &= (-3.0p_1 - 2.0p_2 - 1.0p_3 + 0.0p_4 + 1.0p_5) \times p_4 \times 100\% \\
 err_5 &= (-4.0p_1 - 3.0p_2 - 2.0p_3 - 1.0p_4 + 0.0p_5) \times p_5 \times 100\%
 \end{aligned} \tag{5.50}$$

Another systematic error comes from the acceptance corrections. We have mentioned that in the simulation we took  $T=220$  MeV. We tried to find the effect of temperature change on the yield. We counted the number of tracks as we changed the temperature from 180 MeV to 260 MeV in an increment of 20 MeV. It is seen that Increment in temperature from 180 MeV to 200 MeV increases the yield by 1.07%, change from 200 MeV to 220 MeV increases the yield by 1.05% , change from 220 MeV to 240 MeV increases the yield by 0.7%, change from 240 MeV to 260 MeV increases the yield by 0.7%. Therefore on an average the systematic error is about 1% per 20 MeV change in temperature. The systematic error due to temperature is therefore very small.

The combined systematic errors from these two sources for different centralities are tabulated in Table 5.4.

## 5.17 Results

After we make the acceptance correction we get the following numbers for the multiplicities tabulated in Table 5.5.

We can make comparison with the measurements made in the other detector. In Fig. 5.35 we plot the charged particle multiplicity measured in the MVD as a function of the number of participants. For comparison we plot the multiplicities measured in PHENIX Pad Chambers and  $dN/dE_T$  in the Electromagnetic Calorimeter. From the plot we see that all of them show the same behavior, the multiplicities increases with the number of participants in almost the same manner. We also plot the multiplicity

Centrality	systematic error (%)
0%-5%	6.6
5%-10%	7.6
10%-15%	6.4
15%-20%	5.8
20%-25%	7.0
25%-30%	8.2
30%-35%	8.5
35%-40%	8.6
40%-45%	6.2
45%-50%	8.9

Table 5.4: Systematic errors for the Charged Particle Multiplicities at different centralities

Centrality	$< dN/d\eta >$	$< dE_T/d\eta > [36]$	$< dN/d\eta > [35]$	$< N_{part} > [35]$
0%-5%	639 $\pm$ 48	503 $\pm$ 2	622 $\pm$ 41	347 $\pm$ 10
5%-10%	539 $\pm$ 48	409 $\pm$ 4	498 $\pm$ 31	293 $\pm$ 9
10%-15%	456 $\pm$ 35	340 $\pm$ 5	413 $\pm$ 25	248 $\pm$ 8
15%-20%	379 $\pm$ 28	283 $\pm$ 7	344 $\pm$ 21	211 $\pm$ 7
20%-25%	314 $\pm$ 27	233 $\pm$ 7	287 $\pm$ 18	177 $\pm$ 7
25%-30%	257 $\pm$ 27	191 $\pm$ 8	235 $\pm$ 16	146 $\pm$ 6
30%-35%	211 $\pm$ 22	154 $\pm$ 8	188 $\pm$ 14	122 $\pm$ 5
35%-40%	162 $\pm$ 18	123 $\pm$ 7	147 $\pm$ 12	99 $\pm$ 5
40%-45%	129 $\pm$ 12	98 $\pm$ 7	115 $\pm$ 11	82 $\pm$ 5
45%-50%	101 $\pm$ 14	76 $\pm$ 6	89 $\pm$ 9	68 $\pm$ 4

Table 5.5: Charged Particle Multiplicities for different centralities from the MVD is shown in the second column. The errors include the systematic and statistical. The Particle Multiplicities from the PHENIX Pad Chambers and the  $dN/dE_T$  from EMCal is also tabulated, together with the Number of participants.

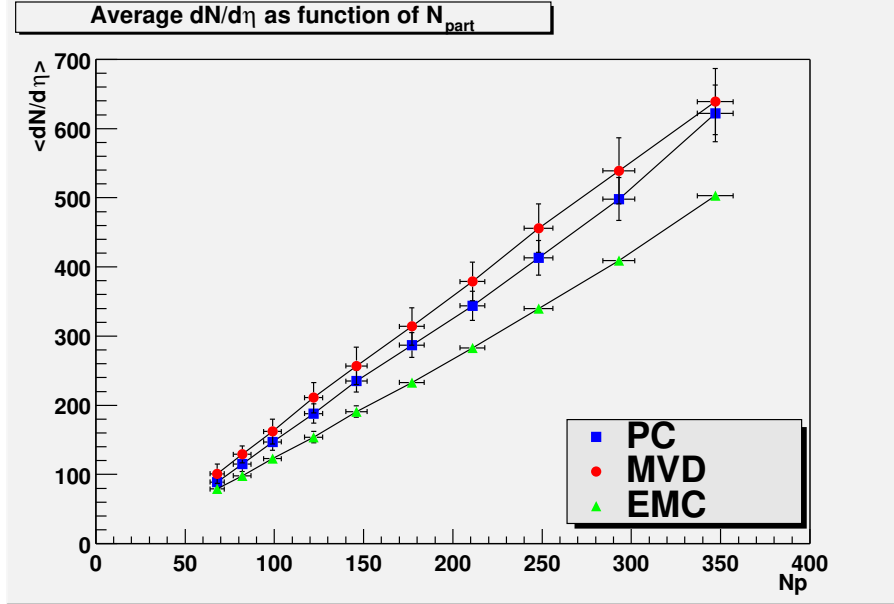


Figure 5.35: Comparison of Charged particle multiplicities in MVD and Pad Chamber in PHENIX. Also is shown the  $dN/dE_T$  measured in the PHENIX Electromagnetic Calorimeter.

per participant vs number of participants in Fig.(5.36). In Fig.(5.37) we show the ratios of the charged particle multiplicities in MVD and in Pad Chambers. It is seen that irrespective of the centrality, the ratio remains almost constant. the same is seen in the ratio of the multiplicity in MVD and the  $dN/dE_T$  in the EMCAL.

We now show the  $dN/d\eta$  vs  $\eta$  plots for different centralities in Fig. 5.38 through Fig. 5.47. We also show the PHOBOS data[45] on the same plot for comparison.

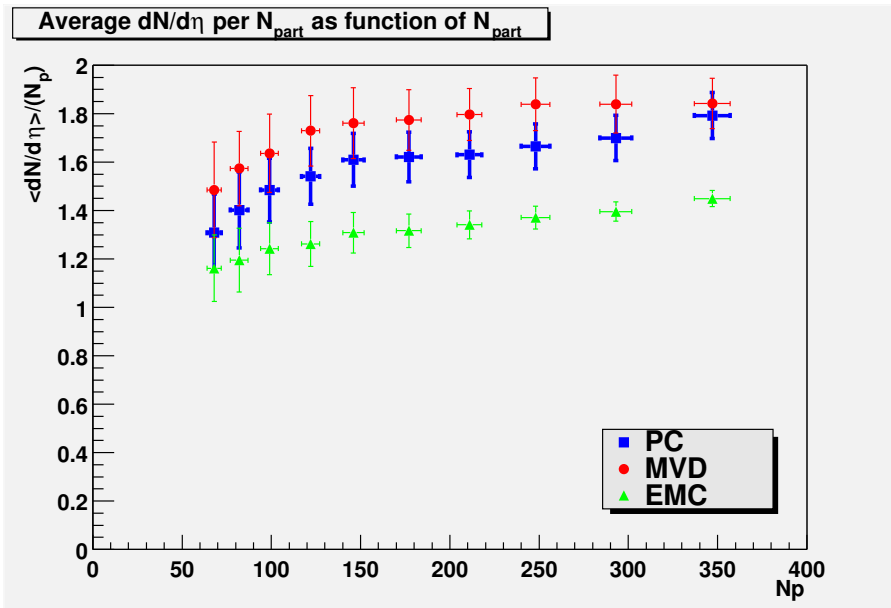


Figure 5.36: Comparison of Charged particle multiplicities per Participant vs The Number of Participants in MVD and Pad Chamber in PHENIX. Also is shown the  $dN/dE_T$  measured in the PHENIX Electromagnetic Calorimeter.

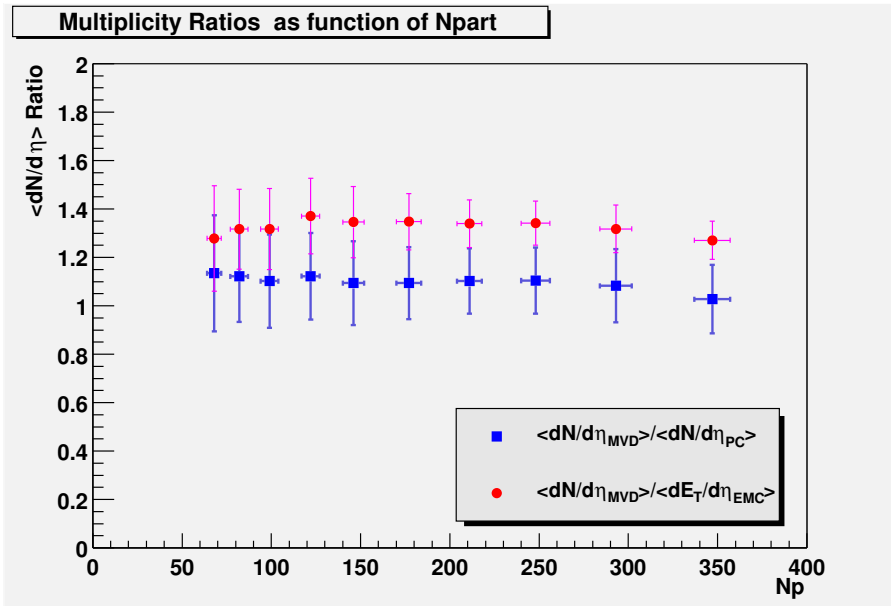


Figure 5.37: Ratio of Charged particle multiplicities per Participant vs The Number of Participants in MVD and Pad Chamber in PHENIX. Also is shown the ratio to  $dN/dE_T$  measured in the PHENIX Electromagnetic Calorimeter.

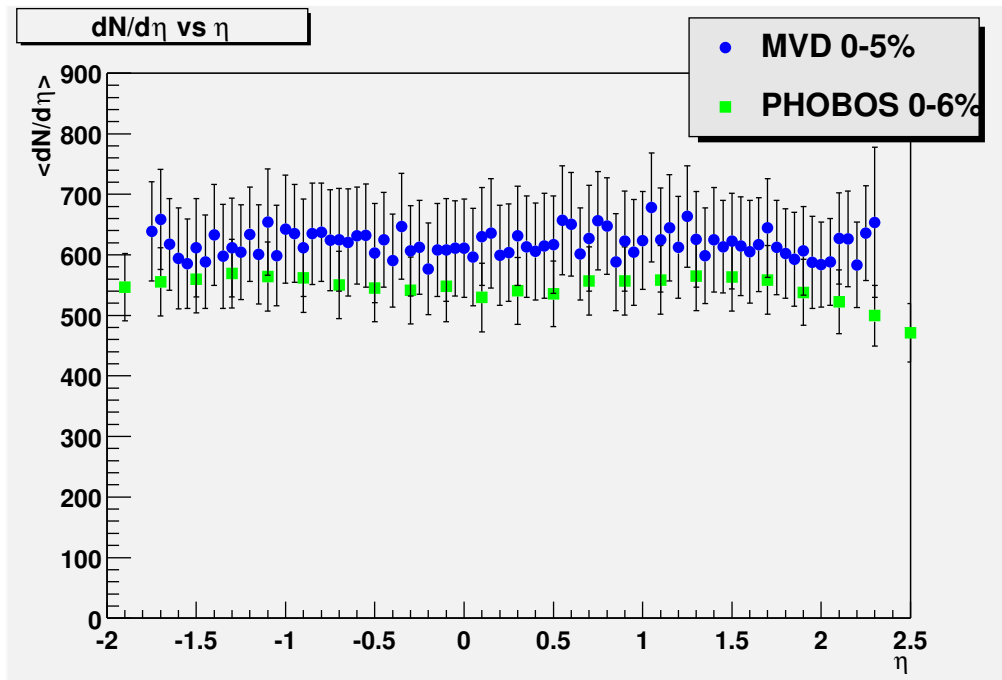


Figure 5.38:  $dN/d\eta$  vs  $\eta$  Distribution for top 5% Central events. Compared with the top 6% of PHOBOS data

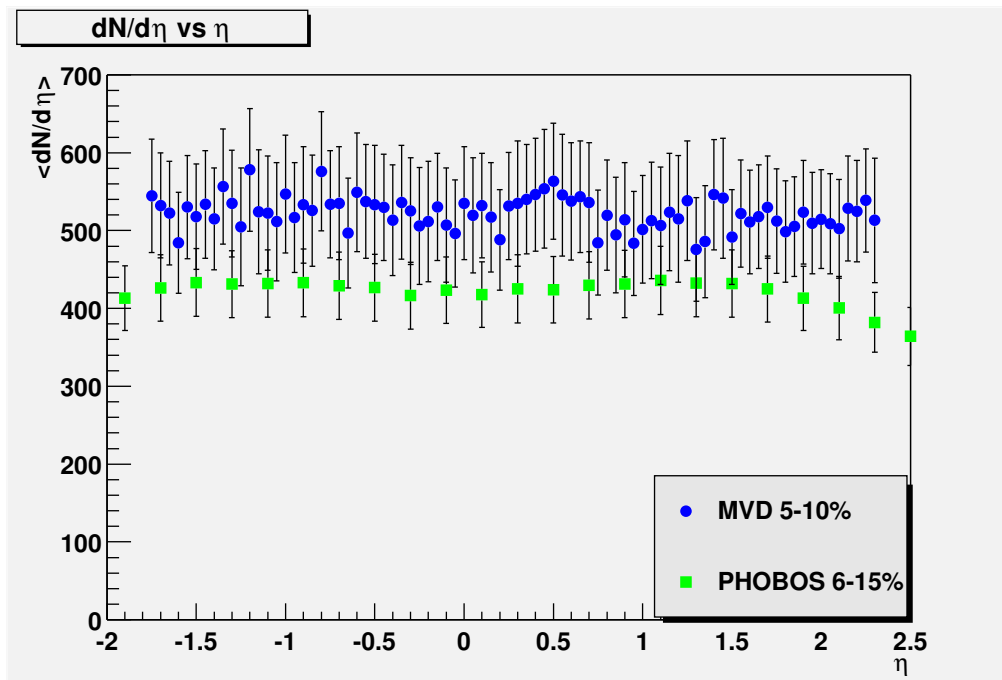


Figure 5.39:  $dN/d\eta$  vs  $\eta$  Distribution for 5% – 10% Central events.

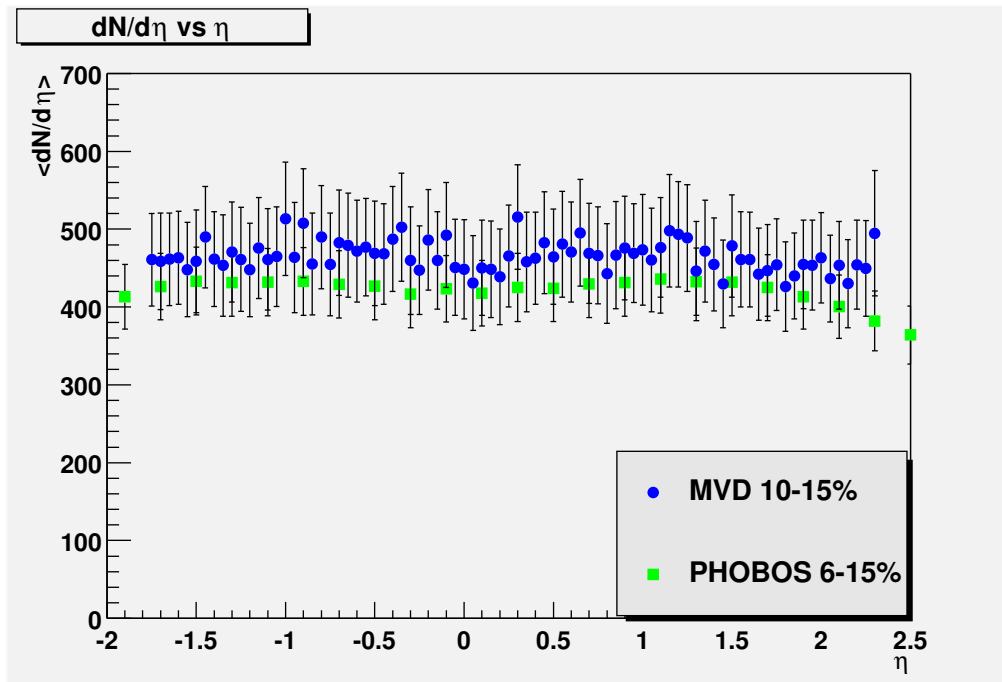


Figure 5.40:  $dN/d\eta$  vs  $\eta$  Distribution for 10% – 15% Central events.

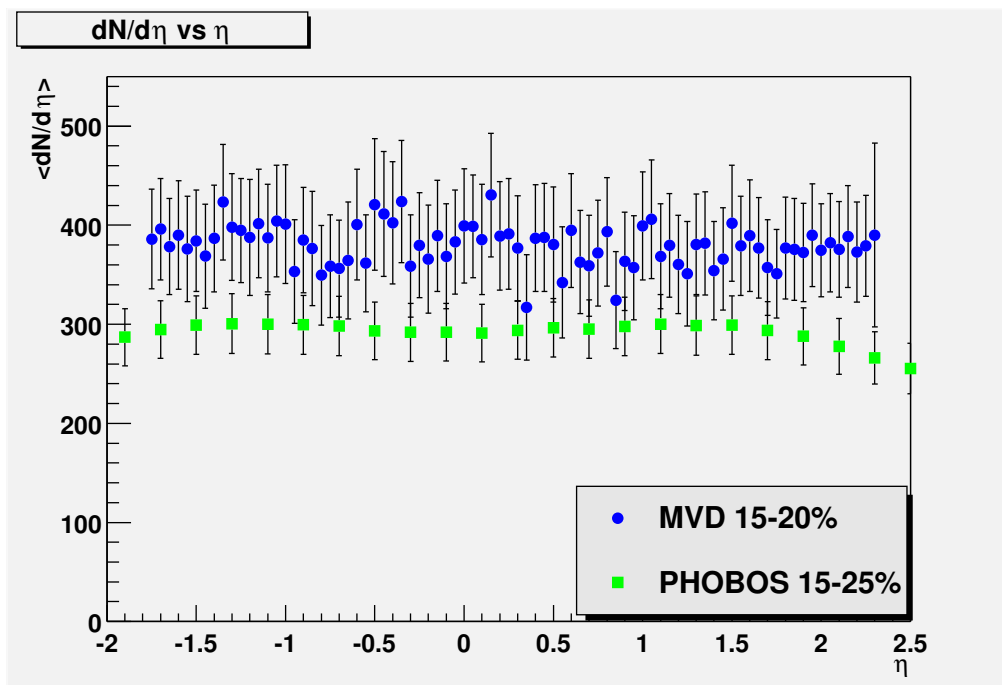


Figure 5.41:  $dN/d\eta$  vs  $\eta$  Distribution for 15% – 20% Central events.

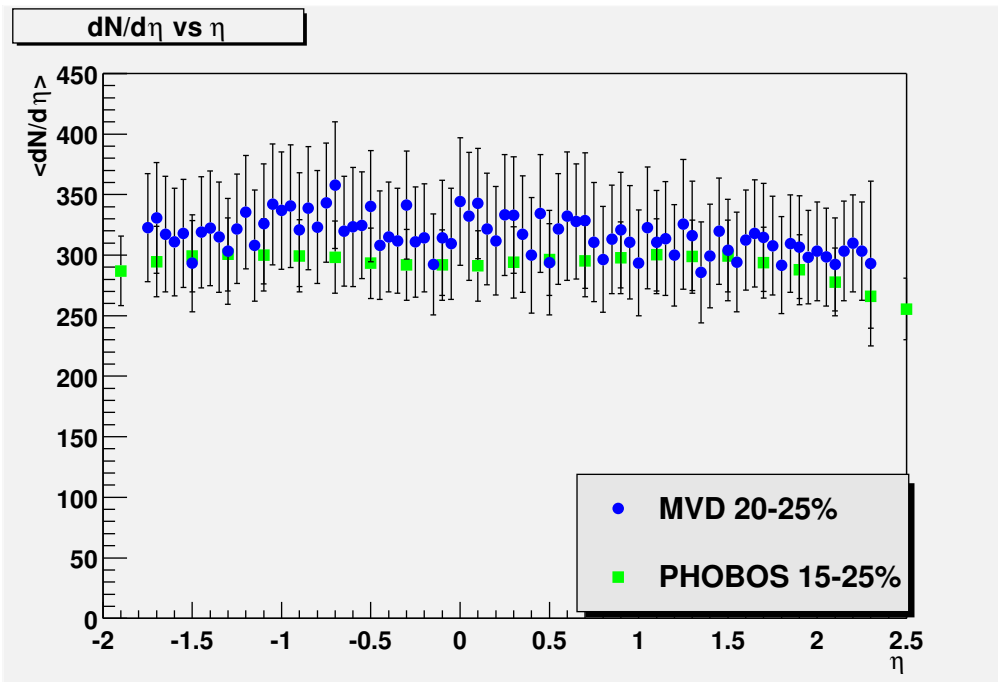


Figure 5.42:  $dN/d\eta$  vs  $\eta$  Distribution for 20% – 25% Central events.

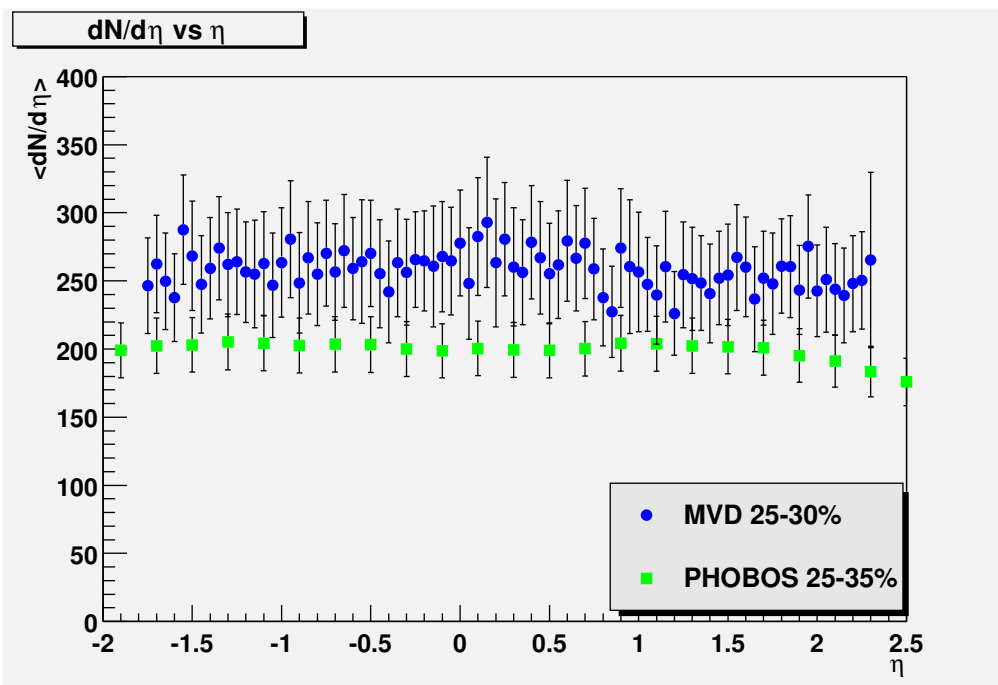


Figure 5.43:  $dN/d\eta$  vs  $\eta$  Distribution for 25% – 30% Central events.

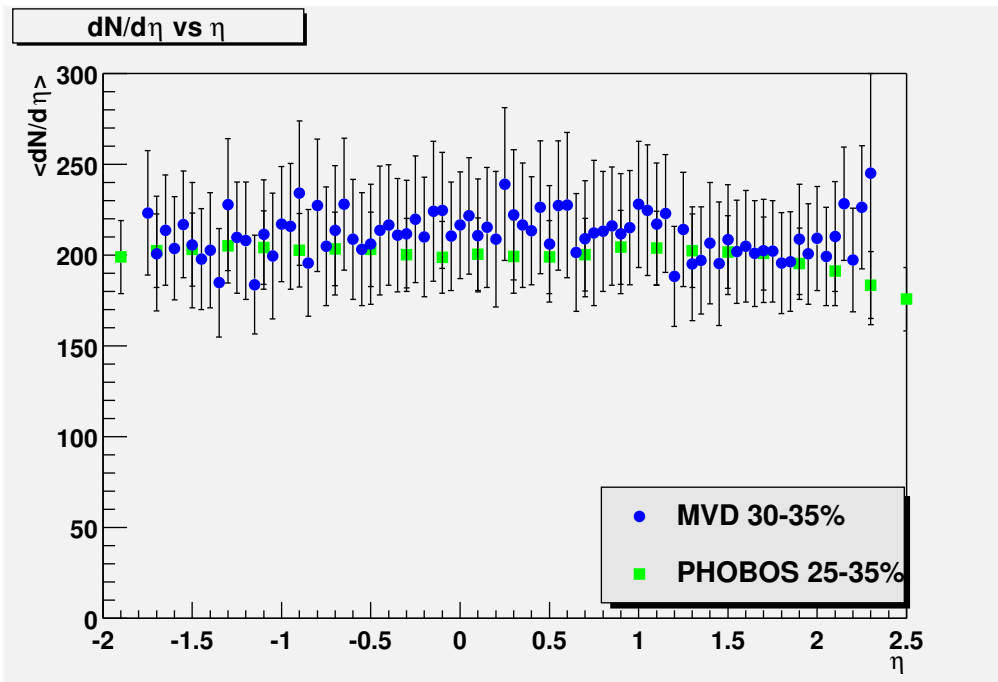


Figure 5.44:  $dN/d\eta$  vs  $\eta$  Distribution for 30% – 35% Central events.

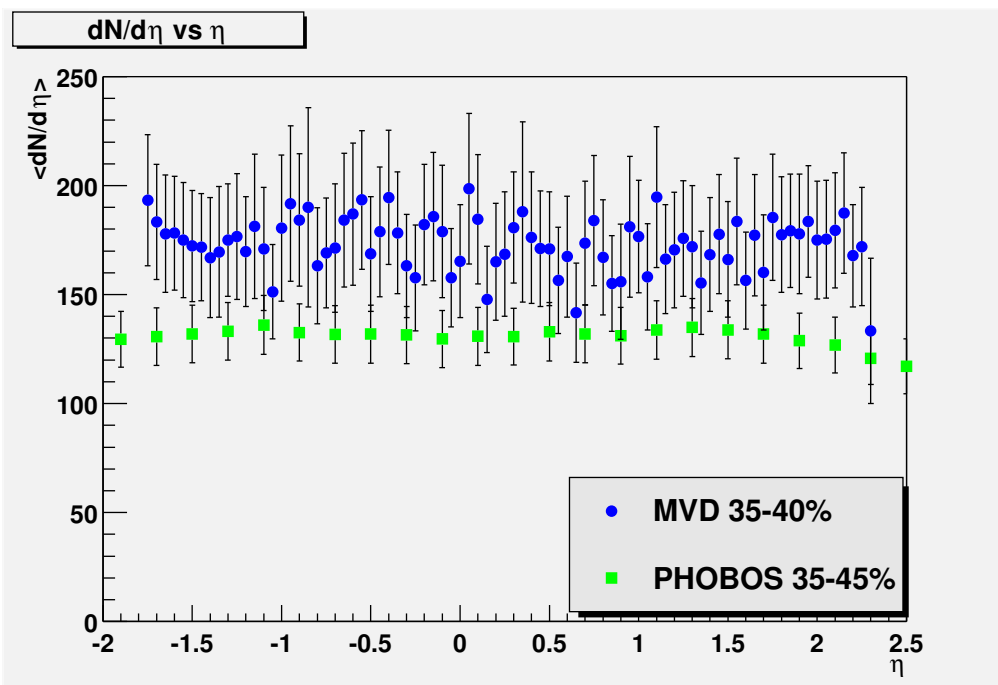


Figure 5.45:  $dN/d\eta$  vs  $\eta$  Distribution for 35% – 40% Central events.

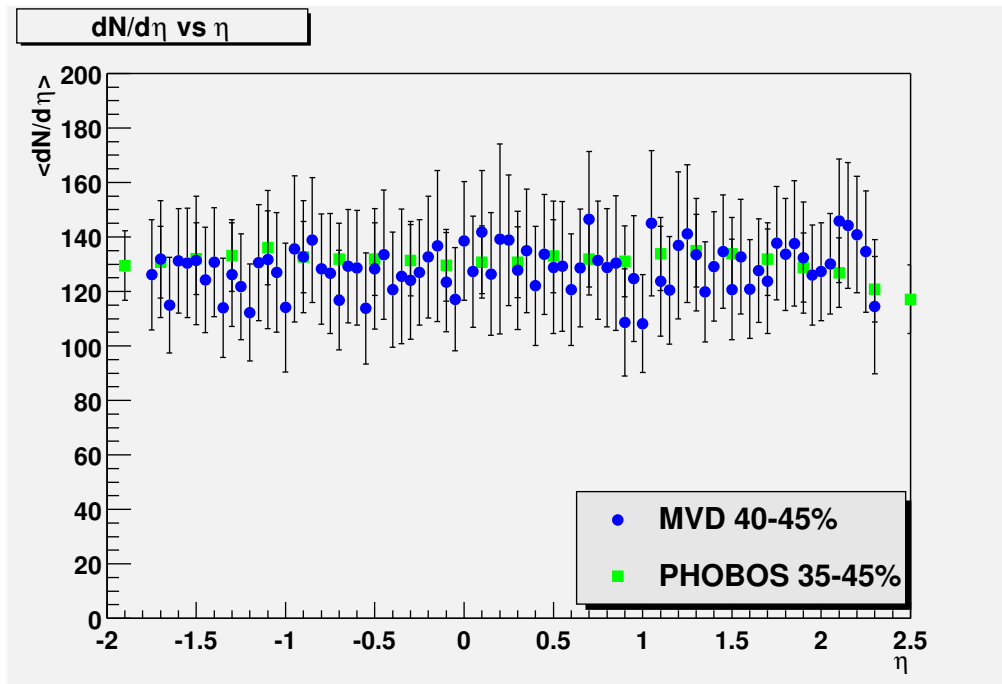


Figure 5.46:  $dN/d\eta$  vs  $\eta$  Distribution for 40% – 45% Central events.

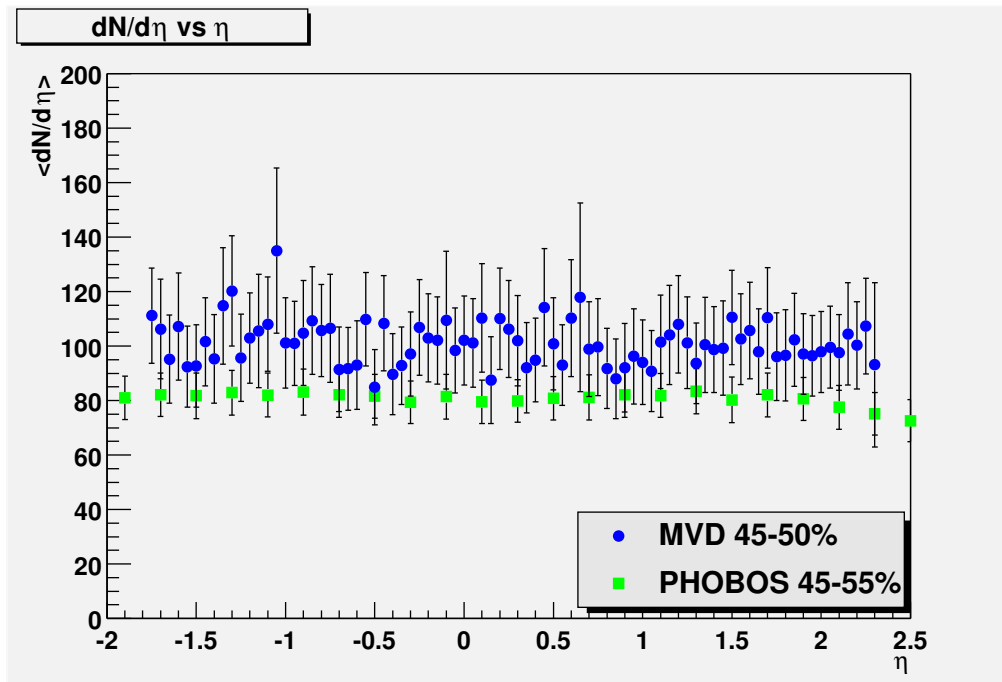


Figure 5.47:  $dN/d\eta$  vs  $\eta$  Distribution for 45% – 50% Central events.

## 5.18 Conclusion

We have measured the charged particle multiplicity with the Multiplicity and Vertex Detector at the PHENIX experiment at RHIC. After making the acceptance correction the  $dN/d\eta$  values found in our measurement agree well with the measurements made with different detectors in PHENIX[35, 36]. We also studied the centrality dependence of the charged particle multiplicity. The measurements made in three separate PHENIX detectors namely MVD, Pad Chambers and the Electromagnetic Calorimeter show similar behavior with the centrality. Although only a fraction of the total MVD coverage participated in the data taking and even there were some difficulties with electronics associated with the active part of the detector, we could correct all the problems such as fluctuation of pedestals with amu cell or event by event pedestal jumping. Our result could be improved if we had better coverage, meaning more silicon strips. This would be especially true for the central events. for central events higher numbers of tracks are produced. If we have chips near the collision for such events, we would accumulate large number of tracks in our coverage . But we may have missed substantial number of the tracks from such events for not having chips close to those events. So definitely, it hurts for not having enough chips. This is true for peripheral events too. But the number of tracks in peripheral events are definitely being less compared to the central events. So the central events are most affected due the small number of chips. But in any case, even with the two active strip detectors, MVD had the largest  $\eta$  coverage and we could measure the charged particle multiplicity over a wide rang of rapidity distribution.

# Chapter 6

## Model Comparison

### 6.1 Introduction

If a quark-gluon plasma is formed in the collision of the two RHIC beams, it will be studied through a number of potential signature. The signals are sensitive to the initial conditions of the dense matter created in the early stage of collisions. The pseudo-rapidity density of multiplicity and transverse energy provide important constraints on these initial conditions.

In the heavy ion collisions at RHIC energies the high density of energy is deposited in the form of gluons. It is proposed by Kharzeev and *et. al*[46, 47, 48, 49] that the charged particle density is determined by the initial gluon density, meaning that the number of particles in the final state corresponds to the number of partons in the initial state. Also we will investigate the model proposed by Gyulassy and Wang[50] based on the HIJING Model.

### 6.2 Energy Density

With the multiplicity value in hand we an attempt to estimate the Bjorken energy scale[23], which relates the energy density to produce a phase transition to the charged

Centrality	0%-5%	0%-10%	10%-20%	20%-30%
$\langle p_t \rangle$ (MeV/c)	523±39	523±41	523±50	523±61

Table 6.1: The Mean  $p_t$  values measured in PHENIX for  $\sqrt{s} = 130$  GeV Data

particle multiplicity:

$$\epsilon_0 = \frac{\langle p_t \rangle}{\pi R^2 \tau_0} \frac{3}{2} \frac{dN}{d\eta} \quad (6.1)$$

where  $\tau_0$  is the formation time, is usually taken as 1fm/c, and  $\pi R^2$  is the effective area of collision. With  $R \sim A^{1/3} \sim 6$  fm.

For the value of  $\langle p_t \rangle$  we look at the  $\langle p_t \rangle$  distribution in PHENIX[51] for the  $\sqrt{s} = 130$  GeV data in Fig. (6.1).

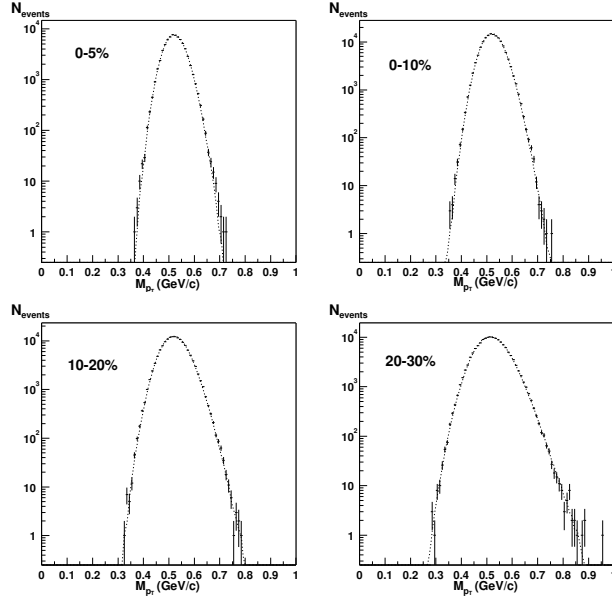


Figure 6.1: The Mean  $p_T$  Distribution for the  $\sqrt{s} = 130$  GeV Data measured in the PHENIX experiment. The plots, clockwise from the top left, are for (a) 0%-5% central events,(a) 0%-10% central events, (a) 20%-30% central events,(a) 10%-20% central events

The mean  $p_T$  for different centralities[51] are tabulated in Table 6.1

$\pi^+$	$\pi^-$	$K^+$	$K^-$	$p$	$\bar{p}$
$276 \pm 3$	$270 \pm 3$	$46.7 \pm 1.5$	$40.5 \pm 2.3$	$28.7 \pm 0.9$	$20.1 \pm 1.0$

Table 6.2: Integrated hadron ( $\pi^{+-}$ ,  $K^{+-}$ ,  $p$  and  $\bar{p}$ ) measured in PHENIX for top 5% events in the  $\sqrt{s} = 130$  GeV Data

	$< p_t > (\text{GeV}/c^2)$
$\pi^+$	$0.387 \pm 0.027$
$\pi^-$	$0.381 \pm 0.027$
$K^+$	$0.560 \pm 0.08$
$K^-$	$0.575 \pm 0.086$
$p$	$0.882 \pm 0.123$
$\bar{p}$	$0.898 \pm 0.125$

Table 6.3: Mean transverse momentum of hadrons ( $\pi^{+-}$ ,  $K^{+-}$ ,  $p$  and  $\bar{p}$ ) measured in PHENIX for top 5% events in the  $\sqrt{s} = 130$  GeV Data

Now,

$$\frac{dN}{dy} = \frac{dN}{d\eta} \frac{d\eta}{dy} \quad (6.2)$$

But

$$\frac{d\eta}{dy} = \frac{\sqrt{\frac{m^2 + p_t^2}{p_t^2} + \sinh \eta}}{\cosh \eta} \quad (6.3)$$

For the calculation of  $\frac{d\eta}{dy}$ , we use the Reference[52], where  $\pi/K/p$  ratios for the the Au-Au collisions at  $\sqrt{130}$  GeV is reported. For the top 5% events, the integrated hadrons yields are given in Table 6.2. Also in Table 6.3 we list the  $< p_t >$  values for  $\pi/K/p$  for the top 5% central events.

We can re-write Eqn.(6.3) as following:

$$\frac{dN}{dy} = \frac{dN}{d\eta} \times \left[ \frac{276 \frac{d\eta}{dy}(\pi^+) + 270 \frac{d\eta}{dy}(\pi^-) + 46.7 \frac{d\eta}{dy}(K^+) + 40.5 \frac{d\eta}{dy}(K^-) + 28.7 \frac{d\eta}{dy}(p) + 20.1 \frac{d\eta}{dy}(\bar{p})}{276 + 270 + 46.7 + 40.5 + 28.7 + 20.1} \right] \quad (6.4)$$

From Eq.(6.3) we find that

$$\begin{aligned}
\frac{d\eta}{dy}(\pi^+) &= 1.063 \\
\frac{d\eta}{dy}(\pi^-) &= 1.065 \\
\frac{d\eta}{dy}(K^+) &= 1.333 \\
\frac{d\eta}{dy}(K^-) &= 1.318 \\
\frac{d\eta}{dy}(p) &= 1.460 \\
\frac{d\eta}{dy}(\bar{p}) &= 1.446
\end{aligned} \tag{6.5}$$

Using values from Eq.(6.5) in Eq.(6.4), we find

$$\frac{dN}{dy} = 1.13 \frac{dN}{d\eta} \tag{6.6}$$

The energy density is therefore,

$$\epsilon_0 \tau_0 = 4.97 \pm 0.74 \text{ GeV/fm}^3 \tag{6.7}$$

This value is significantly above the value estimated for the production of a quark-gluon plasma[8], which is about 2 GeV/fm<sup>3</sup>.

### 6.3 Soft + Hard Process

The HIJING Model predicts that in the ultra-relativistic nuclear collisions the number of particle production have two components. One is the particle production from soft interactions which scales linearly with the number of participant nuclei  $N_p$  in the collision. The second component is from the hard processes (pQCD jets) that scales with the binary collisions  $N_c$ .

Let us assume that the fraction  $X(s)$  of the multiplicity  $n_{pp}$  measured in a  $pp$  collisions per unit pseudo-rapidity is due to hard process, with the remaining  $(1 -$

Centrality	$\langle dN/d\eta \rangle$	$\langle N_{part} \rangle$	$\langle N_{coll} \rangle$
0%-5%	639 $\pm$ 48	347 $\pm$ 10	946 $\pm$ 146
5%-10%	539 $\pm$ 48	293 $\pm$ 9	749 $\pm$ 116
10%-15%	456 $\pm$ 35	248 $\pm$ 8	596 $\pm$ 93
15%-20%	379 $\pm$ 28	211 $\pm$ 7	478 $\pm$ 75
20%-25%	314 $\pm$ 27	177 $\pm$ 7	377 $\pm$ 61
25%-30%	257 $\pm$ 27	146 $\pm$ 6	290 $\pm$ 47
30%-35%	211 $\pm$ 22	122 $\pm$ 5	226 $\pm$ 38
35%-40%	162 $\pm$ 18	99 $\pm$ 5	170 $\pm$ 30
40%-45%	129 $\pm$ 12	82 $\pm$ 5	130 $\pm$ 24
45%-50%	101 $\pm$ 14	68 $\pm$ 4	101 $\pm$ 19

Table 6.4: Charged Particle Multiplicities for different centralities and Number of participants and collisions.

$X(s)$ ) being from soft process. The charged particle multiplicity will then have the following form:

$$\frac{dN}{d\eta} = (1 - X(s))n_{pp} \frac{\langle N_p \rangle}{2} + X(s)n_{pp} \langle N_c \rangle \quad (6.8)$$

In order to compare our measurement of the charged particle multiplicity with the model, we need to determine  $X(s)$  and  $n_{pp}$ , and we will use the  $N_p$  and  $N_c$  given in Table 6.4.

In order to determine  $n_{pp}$  we use the approach of the PHOBOS collaboration, where they fit the data on the pseudo-rapidity density of charged multiplicity in non-singular diffractive  $pp$  interactions[53]

$$n_{pp} = 2.5 - 0.25 \ln(s) + 0.023 \ln^2(s), \quad (6.9)$$

with  $\sqrt{s}=130$  GeV, we find  $n_{pp} \simeq 2.25$ . The value of  $X(s)$  was determined by Kharzeev[46] to be  $0.09 \pm 0.03$ . With the values, we can write:

$$\frac{1}{N_p} \frac{dN}{d\eta} = \frac{1}{N_p} (1.02N_p + 0.20N_c) \quad (6.10)$$

The comparison of our measurement with the model is shown in Fig.(6.2). It is seen that the model can describe the data qualitatively, but not quantitatively.

## 6.4 High Density QCD and Hadron Production

The pseudo-rapidity density at RHIC energy can be described by a saturation model proposed by Kharzeev and Nardi [46]. The gold beams at RHIC are boosted to a large momentum. The nucleus is therefore Lorentz contracted. The partons thus lie on a thin sheet in the transverse plane. If the transverse momentum of a parton is  $Q_s$ , then the uncertainty principle determines the transverse area occupied by a parton, which is  $\sim 1/Q_s^2$ . The partons can be probed with a cross-section of  $\sim \alpha_s(Q_s^2)/Q_s^2$ . The entire transverse area of the nucleus is  $S_A \sim \pi R_A^2$ . Thus, if the number of partons exceeds

$$N_A \sim \frac{S_A}{\sigma} \sim \frac{1}{\alpha_s(Q_s^2)} Q_s^2 \pi R_A^2 \quad (6.11)$$

the partons will overlap in the transverse plane and starts interacting with each other. This puts a cut-off or in other words, saturates the parton densities. This is the simplest picture of saturation model, on which models are developed which tries to explain the pseudo-rapidity density of charged hadrons produced at the RHIC energies.

In terms of Bjorken  $x$ , the *saturation scale* [54], the critical value of the momentum transfer is given by

$$Q_s^2 \sim \alpha_s \frac{x G_A(x, Q_s^2)}{\pi R_A^2} \quad (6.12)$$

We now try to find the coefficient of proportionality in (6.12) following [54, 55, 56], which relates the saturation scale to the number of colors  $N_c$ , the gluon structure function  $x G_A(x, Q_s^2)$  and the density of participants  $\rho_{part}$  in the transverse plane:

$$Q_s^2 = \frac{8\pi^2 N_c}{N_c^2 - 1} \alpha_s(Q_s^2) x G(x, Q_s^2) \frac{\rho_{part}}{2}, \quad (6.13)$$

Equation (6.13) can be solved by iteration. For the Au-Au collision at  $\sqrt{s} = 130$  GeV, the saturation scale is found to be  $Q_s^2 \simeq 2$  GeV<sup>2</sup> [46] for  $xG(x, Q_s^2) \simeq 2$  [57] at  $x \simeq 2Q_s/\sqrt{s} \simeq 0.02$ , with  $\alpha_s(Q_s^2) \simeq 0.6$

The number of partons produced in the collision is given by[56]

$$\frac{d^2N}{d^2bd\eta} = c \frac{N_c^2 - 1}{4\pi^2 N_c} \frac{1}{\alpha_s} Q_s^2, \quad (6.14)$$

where  $c$  is the “parton liberation” coefficient accounting for the transformation of virtual partons in the initial state to the on-shell partons in the final state. Integration over the transverse coordinate and the use of (6.13) yield simply

$$\frac{dN}{d\eta} = c N_{part} xG(x, Q_s^2). \quad (6.15)$$

We now make an estimate of the constant  $c$ . To do so we make some assumptions following Reference[46]:

$$\begin{aligned} \frac{dN}{d\eta} &\simeq \frac{3}{2} \left( \frac{dN}{d\eta} \right)_{exp} \\ xG(x, Q_s^2) &\simeq 2 \quad \text{at } Q_s^2 \simeq 2 \text{ GeV}^2 \\ x &\simeq 2Q_s/\sqrt{s} \simeq 0.02[57] \end{aligned}$$

The  $\left( \frac{dN}{d\eta} \right)_{exp}$  for the top 5% central events were found from the MVD analysis to be  $639 \pm 48(syst) \pm 10(stat)$ , and the number of participants is  $N_{part} = 347$ . These give us the parton liberation coefficient to be:

$$c = 1.38 \pm 0.25 \quad (6.16)$$

For comparison we tabulate the values of  $c$  calculated in various approaches:

MVD Data : Saturation Model Calculation	$1.38 \pm 0.25$
PHOBOS Data : Saturation Model Calculation[46]	$1.23 \pm 0.20$
Lattice Calculation[58]	$1.29 \pm 0.09$
Analytical Calculation[59]	$2 \ln 2 \simeq 1.39$

The values are of the order of unity and agree with each other.

## 6.5 Energy Density using the Saturation Model

Using the saturation model we can make an estimate of the Bjorken energy density[23]. The energy density is related to the mean transverse momentum  $\langle k_t \rangle$ , the formation time  $\tau_0$  and the multiplicity by the relation:

$$\epsilon_0 \simeq \frac{\langle k_t \rangle}{\tau_0} \frac{d^2 N}{d^2 b d\eta} \quad (6.17)$$

where  $d^2 b$  in Eq.(6.17) is the transverse area of the collision. according to the saturation model, the formation time of the partons is  $\tau_0 \simeq 1/Q_s$  and the transverse momentum of partons are about  $\langle k_t \rangle \simeq Q_s$ . Therefore Eq.(6.17) can be re-written as:

$$\epsilon_0 \simeq Q_s^2 \frac{d^2 N}{d^2 b d\eta} \quad (6.18)$$

Now we take the saturation scale  $Q_s \simeq 2$  GeV<sup>2</sup>. From Table 6.5 we can estimate that the value of  $b$  corresponding to  $Q_s \simeq 2$  GeV<sup>2</sup> is 2.7 fm. The transverse area, when integrated over  $b$ , is therefore 91.6 fm<sup>2</sup>.  $\frac{dN}{d\eta} \simeq \frac{3}{2} \left( \frac{dN}{d\eta} \right)_{exp}$ , which is  $\frac{3}{2} \cdot 639 = 958.5$ . This gives us  $\frac{d^2 N}{d^2 b d\eta} = 10.46$ . Therefore,

$$\epsilon_0 \simeq 21 \text{ GeV/fm}^3 \quad (6.19)$$

The energy density calculated for the PHOBOS data using the saturation model is 18 GeV/fm<sup>3</sup>[46]. This value is well above the energy density needed to induce the QCD phase transition according to lattice calculations[8].

## 6.6 Centrality Dependence

In order to compute the centrality dependence of the charged particle multiplicities, we need to know how the gluon structure function evolves with the parton density. Following references[60, 61], we take

$$xG(x, Q_s^2) \sim \ln \left( \frac{Q_s^2}{\Lambda_{QCD}^2} \right). \quad (6.20)$$

$b$ (fm)	$N_{part}$	$N_{coll}$	$\rho_{part}$ (fm $^{-2}$ )	$Q_s^2$ (GeV $^2$ )
0.	378.4	1202.7	3.06	2.05
1.	372.4	1173.6	3.05	2.04
2.	354.7	1092.9	3.01	2.02
3.	327.0	975.7	2.95	1.98
4.	292.2	837.0	2.86	1.92
5.	253.2	689.6	2.75	1.84
6.	212.3	543.5	2.60	1.74
7.	171.5	406.7	2.41	1.61
8.	132.4	285.6	2.17	1.46
9.	96.5	184.8	1.89	1.26
10.	65.1	107.4	1.54	1.04
11.	39.5	54.1	1.15	0.77

Table 6.5: Saturation scale and Number of participants and collisions for different impact parameters

which enables us to write an equation on the centrality dependence charged particle multiplicity as:

$$\frac{1}{N_{part}} \frac{dn}{d\eta} \simeq 0.46 \ln \left( \frac{Q_s^2}{\Lambda_{QCD}^2} \right), \quad (6.21)$$

We take  $\Lambda_{QCD} \simeq 200$  MeV. We use the following table[46] for the number of participants and saturation scale to compute the centrality dependent multiplicity and compare with the result obtained in MVD.

The result and the model comparison is shown in Fig(6.2). We can readily see that the saturation model does the best description of the data. The Soft+Hard model does describe the data qualitatively for more central events, but it does not describe the shape of the distribution. On the other hand, the saturation model of Kharzeev and Nardi fits the data better.

Let us now try to derive a relation based on the saturation model that can describe the charged particle multiplicity density as a function of pseudo-rapidity.

Let  $\varphi_A(x, k_t^2)$  be the probability of finding a gluon with a given  $x$  and transverse

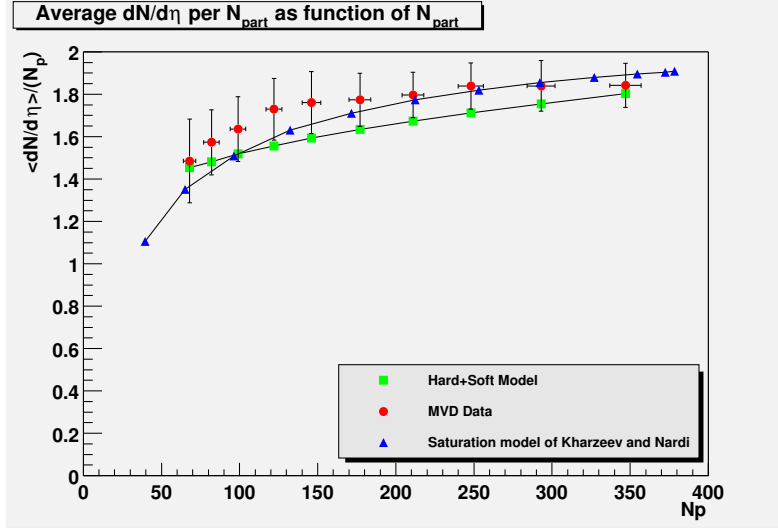


Figure 6.2: Centrality dependence of charged particle multiplicity per participant for the Au-Au collision at  $\sqrt{s}=130$  GeV. The red circles are the data points from MVD. Green triangles are the saturation model calculation[49]. Also shown in the blue squares the calculations from soft+hard model from Eqn.(6.10)[50].

momentum  $k_t$ . The structure function for gluons can be found for in the saturation from Eq.(6.12) as:

$$xG_A(x, Q_s^2) \sim \frac{\pi}{\alpha_s(Q_s^2)} Q_s^2 R_A^2, \quad (6.22)$$

the corresponding unintegrated gluon distribution is given by

$$\varphi_A(x, k_t^2) \sim \frac{S_A}{\alpha_s}; \quad k_t^2 \leq Q_s^2, \quad (6.23)$$

The differential cross-section of gluon production in an A-A collision is written as[54, 62]

$$E \frac{d\sigma}{d^3p} = \frac{4\pi N_c}{N_c^2 - 1} \frac{1}{p_t^2} \int dk_t^2 \alpha_s \varphi_A(x_1, k_t^2) \varphi_A(x_2, (p - k)_t^2), \quad (6.24)$$

where  $x_{1,2} = (p_t/\sqrt{s}) \exp(\pm\eta)$ , with  $\eta$  the (pseudo)rapidity of the produced gluon; the running coupling  $\alpha_s$  has to be evaluated at the scale  $Q^2 = \max\{k_t^2, (p - k)_t^2\}$ .

The rapidity density is then evaluated from (6.24) according to

$$\frac{dN}{dy} = \frac{1}{\sigma_{AA}} \int d^2 p_t \left( E \frac{d\sigma}{d^3p} \right), \quad (6.25)$$

where  $\sigma_{AA}$  is the inelastic cross section of nucleus–nucleus interaction. Integration over the transverse momentum gives

$$\frac{dN}{dy} = \text{const } S_A Q_{s,\min}^2 \ln\left(\frac{Q_{s,\min}^2}{\Lambda_{QCD}^2}\right) \left[ 1 + \frac{1}{2} \ln\left(\frac{Q_{s,\max}^2}{Q_{s,\min}^2}\right) \left(1 - \frac{Q_{s,\max}}{\sqrt{s}} e^{|y|}\right)^4 \right], \quad (6.26)$$

Since  $S_A Q_s^2 \sim N_{part}$ , we can re-write (6.26) in the following final form

$$\frac{dN}{dy} = c N_{part} \left(\frac{s}{s_0}\right)^{\frac{\lambda}{2}} e^{-\lambda|y|} \left[ \ln\left(\frac{Q_s^2}{\Lambda_{QCD}^2}\right) - \lambda|y| \right] \left[ 1 + \lambda|y| \left(1 - \frac{Q_s}{\sqrt{s}} e^{(1+\lambda/2)|y|}\right)^4 \right], \quad (6.27)$$

with  $Q_s^2(s) = Q_s^2(s_0) (s/s_0)^{\lambda/2}$ .

### 6.6.1 Converting Gluons into Hadrons

Equation(6.27) describes the distribution for radiated gluons. In the experiment we measure the charged hadrons. So the Equation(6.27) needs to be converted so that it describes the hadron distribution. As the system evolves, the distribution in rapidity is not preserved, but the angle of the produced gluons are remembered by the hadrons[59]. Therefore Equation(6.27) can be converted to a function of pseudorapidity, which is a function of the angle( $\eta = -\ln \tan(\theta/2)$ ). The rapidity  $y$  and the pseudorapidity  $\eta$  is related by,

$$y(\eta; p_t; m) = \frac{1}{2} \ln \left[ \frac{\sqrt{\frac{m^2 + p_t^2}{p_t^2} + \sinh^2 \eta} + \sinh \eta}{\sqrt{\frac{m^2 + p_t^2}{p_t^2} + \sinh^2 \eta} - \sinh \eta} \right]; \quad (6.28)$$

and

$$\frac{\delta y(\eta; p_t; m)}{\delta \eta} = h(\eta; p_t; m) = \frac{\cosh \eta}{\sqrt{\frac{m^2 + p_t^2}{p_t^2} + \sinh^2 \eta}}, \quad (6.29)$$

The value of  $\lambda$ , describing the growth of the gluon structure functions at small  $x$  can be determined in deep inelastic scattering; the HERA data are fitted with  $\lambda \simeq 0.25 \div 0.3$  [63]. Following reference[47] we use  $m^2 \simeq Q_s \cdot 1 \text{ GeV}$ ,  $\Lambda_{QCD} \sim 200 \text{ MeV}$ ,  $p_t = Q_s$ .

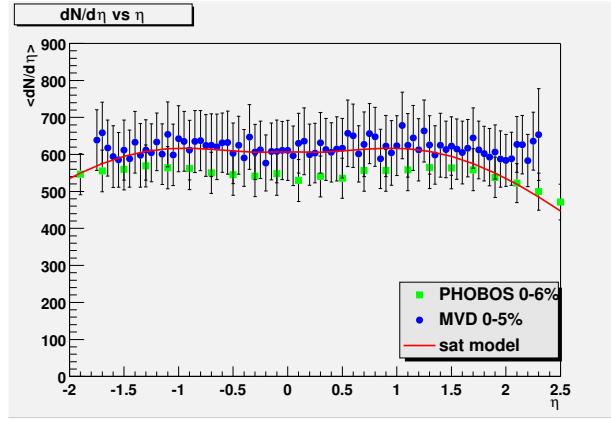


Figure 6.3:  $dN/d\eta$  vs  $\eta$  Distribution for top 5% Central events. Compared with the top 6% of PHOBOS data and Saturation Model of Kharzeev and Nardi[47]

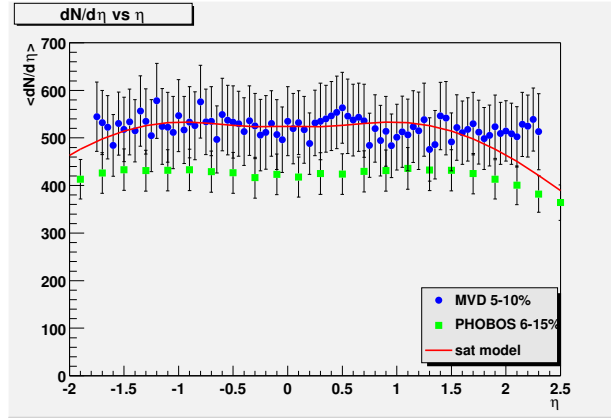


Figure 6.4:  $dN/d\eta$  vs  $\eta$  Distribution for 5% – 10% Central events.

Using the values for  $Q_s$  from Table6.5 and comparing the values of  $N_{part}$  in Table6.5 and Table6.4 to make an estimate of  $Q_s$  for different centralities.

We now show the  $dN/d\eta$  vs  $\eta$  plots for different centralities. We also show the saturation model calculation and the PHOBOS data on the same plot for comparison. In all the centralities, the saturation model fits well within the error bar of the data.

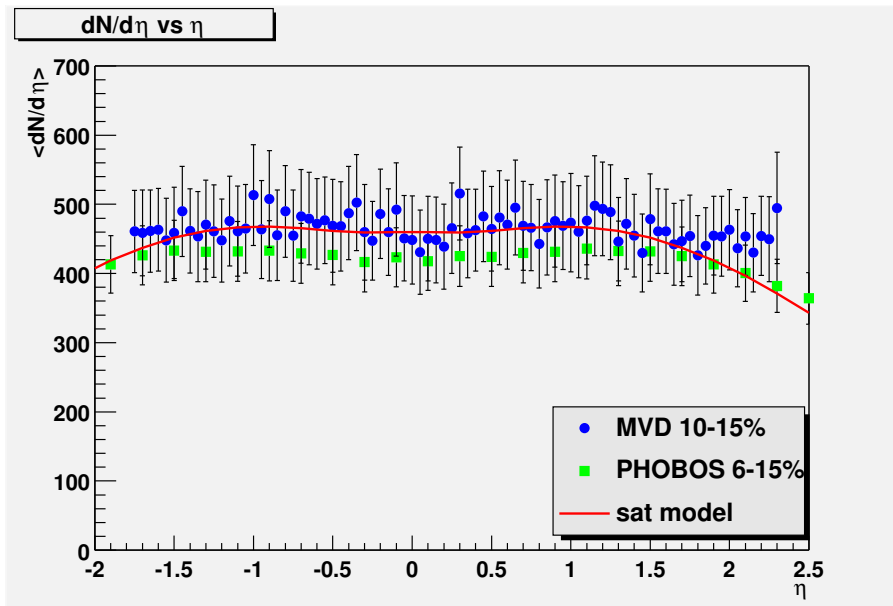


Figure 6.5:  $dN/d\eta$  vs  $\eta$  Distribution for 10% – 15% Central events.

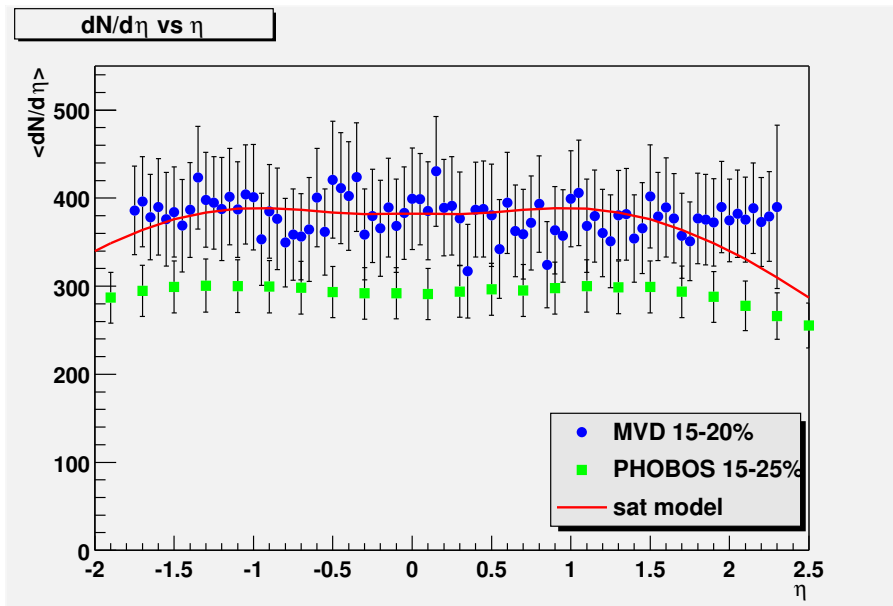


Figure 6.6:  $dN/d\eta$  vs  $\eta$  Distribution for 15% – 20% Central events.

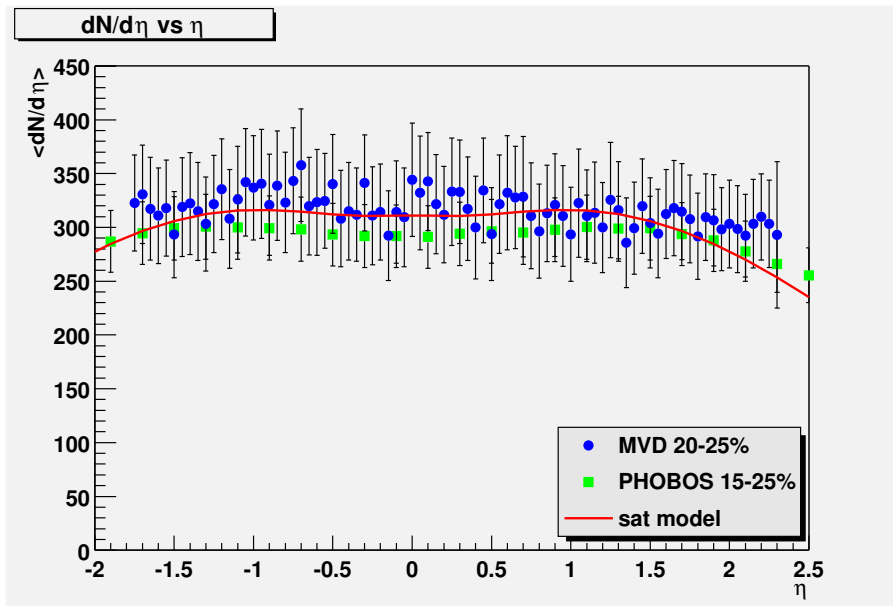


Figure 6.7:  $dN/d\eta$  vs  $\eta$  Distribution for 20% – 25% Central events.

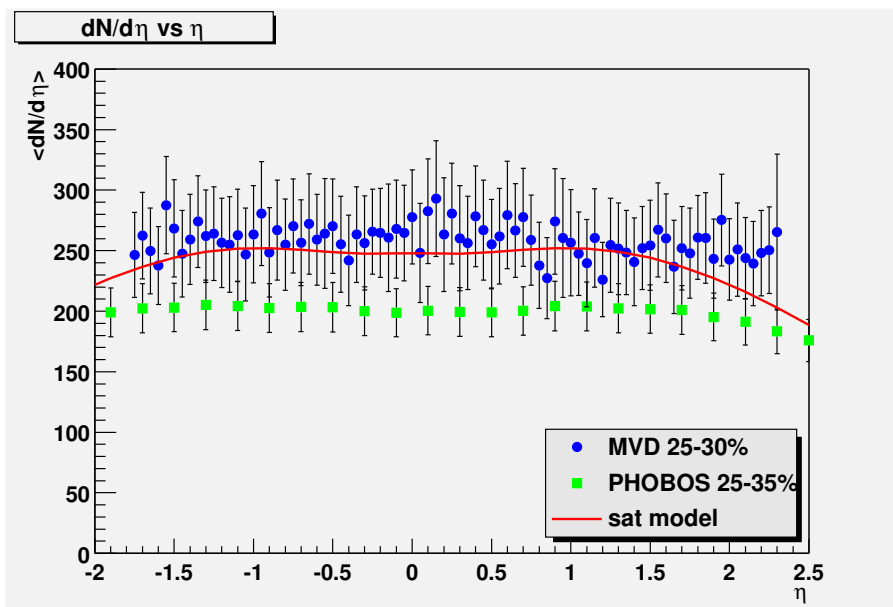


Figure 6.8:  $dN/d\eta$  vs  $\eta$  Distribution for 25% – 30% Central events.

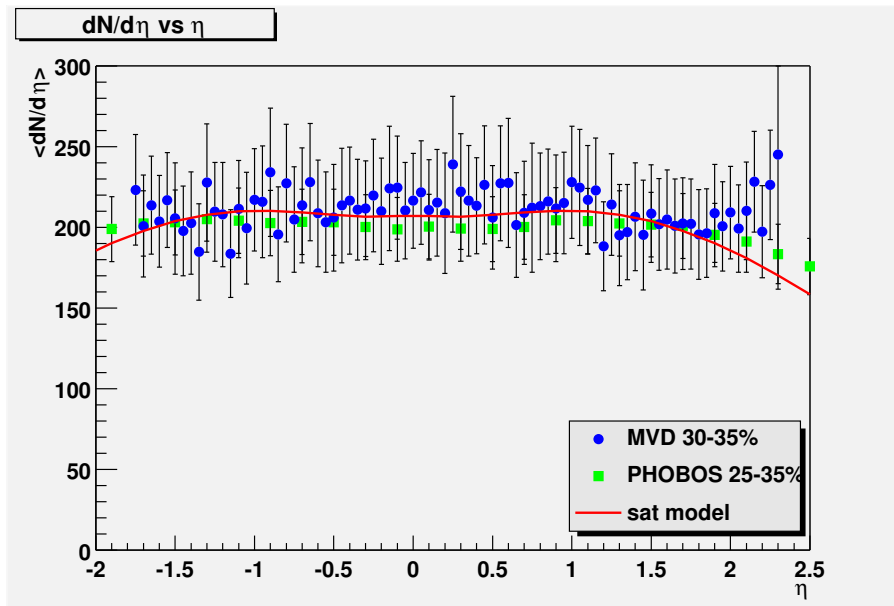


Figure 6.9:  $dN/d\eta$  vs  $\eta$  Distribution for 30% – 35% Central events.

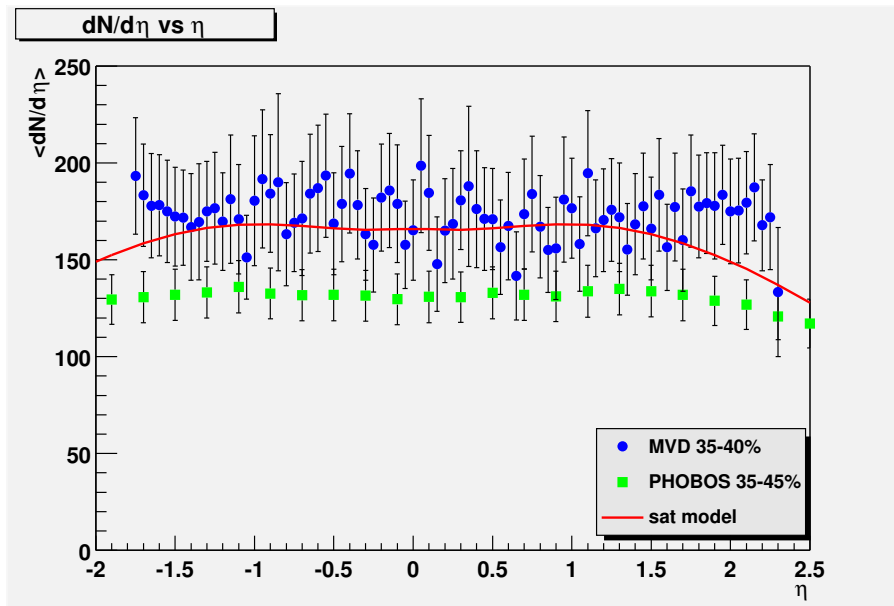


Figure 6.10:  $dN/d\eta$  vs  $\eta$  Distribution for 35% – 40% Central events.

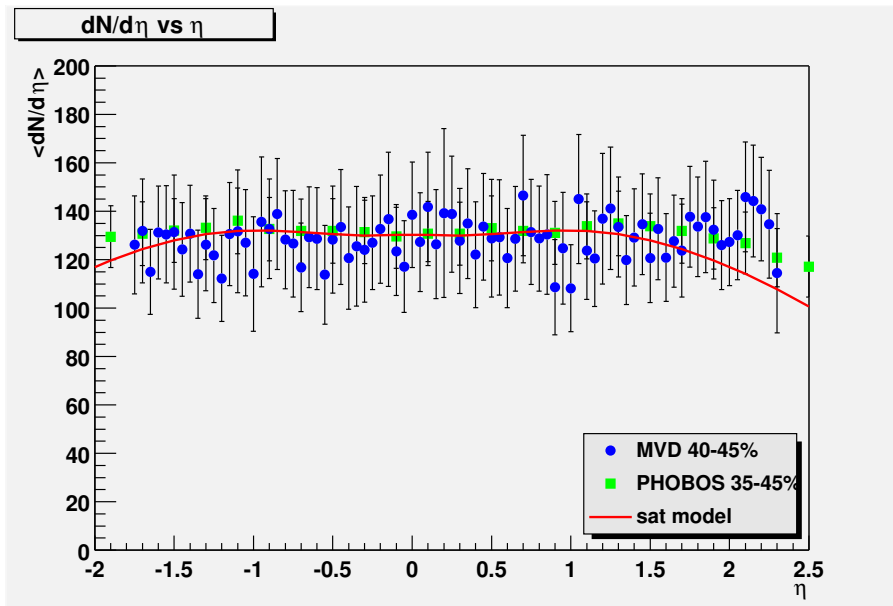


Figure 6.11:  $dN/d\eta$  vs  $\eta$  Distribution for 40% – 45% Central events.

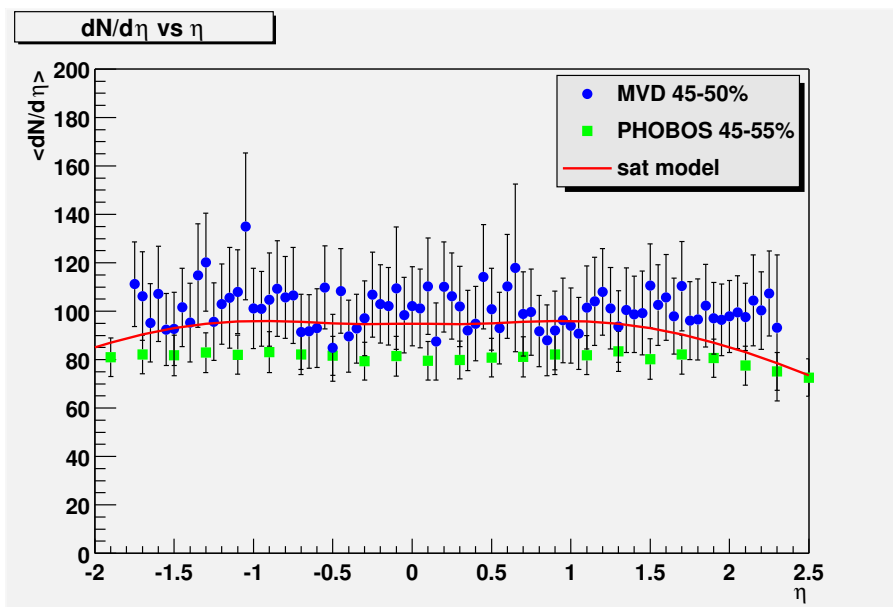


Figure 6.12:  $dN/d\eta$  vs  $\eta$  Distribution for 45% – 50% Central events.

## 6.7 Conclusion

We have made measurements on the charged particle multiplicities and their centrality dependence. In order to interpret the results we needed to compare the results with theoretical models. First we compared the data with the HIJING Soft+Hard model. The model could qualitatively describe the data for the more central events, but can not describe the shape of the distribution. We then compared the data with the saturation model. The saturation model could describe the data well. Using the saturation model we calculated the gluon liberation coefficient that agrees well with the lattice calculations. The energy density calculated using the saturation model is well above the energy needed to induce the QCD phase transition. Considering all these aspects of the saturation model, it is the best model in hand to effectively describe the data.

# Bibliography

- [1] M. Gell-Mann, Phys. Lett. **8** (1964), 214; G. Zweig, CERN Report 8182/TH.401 (1964).
- [2] Gross, D.J. and Wilczek, F., Phys. Rev. Lett. **30** (1973), 1343; Politzer, H.D., Phys. Rev. Lett. **30** (1973), 1346.
- [3] H. Satz, Ann. Rev. Nucl. Part. Sci. **35** (1985), 245.
- [4] R. Hagedorn, Cargese Lectures in Physics, Vol. 6, Gordon and Breach, 1973.
- [5] Wilson K. Phys. Rev. **D10** (1974), 2445.
- [6] Creutz M. *Quarks, Gluons and Lattices* (Cambridge University Press, Cambridge, 1983).
- [7] J. Collins and M.J. Perry Phys. Lett. **34** (1975), 1353.
- [8] For example, see *Proceedings of Quark Matter 1984*, edited by K. Kajantie (Springer, Berlin, 1985); *Proceedings of Quark Matter 1987*, edited by H. Satz, H.J. Specht and R. Stock.
- [9] J.W Harris and B. Muller, Ann.Rev.Nucl.Part.Sci. **46** (1996) p71-107.
- [10] S.A. Bass, M. Gyulassy, H. Stocker and W Greiner, J.Phys. **G25** (1999).
- [11] K. Kajantie and L. McLerran, Ann. Rev. Nucl. Sci. **37** (1987), 293.

- [12] *QGP Signatures*, edited by V. Bernard, et al. (Editions Frontières, Paris, 1990).
- [13] L. van Hove Phys. Lett. **B118** (1982), 138; Z. Phys. **C21** (1983), 93.
- [14] P.J. Siemens and S.A. Chin, Phys. Rev. Lett. **55** (1985), 1266.
- [15] D. Seibert Phys. Rev. Lett. **68** (1992), 1476; D. Seibert, V.K. Mishra and G. Fai, Phys. Rev. **C46** (1992), 330.
- [16] C. Gale and J. Kapusta, Phys. Rev. **C35** (1987), 2107.
- [17] F. Karsch , K. Redlich and L. Turko, Z. Phys. **C60** (1995), 519.
- [18] U. Heinz and K.S. Lee, Phys. Lett. **B259** (1991), 162.
- [19] J. Rafelski and B. Mueller, Phys. Rev. Lett. **48** (1982), 1066; **56** (1986), 2334E.
- [20] P. Koch, B. Mueller, and J. Rafelski, Phys. Rep. **142** (1986), 167.
- [21] C.M. Ko, *et al.*, Phys. Rev. Lett. **66** (1991), 2577.
- [22] T. Abbott, et al. [E-802 collaboration], Phys. Lett. **B197**, 285 (1987); Phys. Rev. Lett. **64**, 847 (1990); S. E. Eiseman, et al. [E-810 collaboration]. Phys. Lett. **B248**, 254 (1990); J. Bartke, et al. [NA35 collaboration], Z. Phys. **C48**, 191 (1990); H. van Hecke, et al. [HELIOS collaboration], Nucl. Phys. **A525**, 227c (1991); S. Abatzis, et al. [WA85 collaboration], Phys. Lett. **B270**, 123 (1991).
- [23] J.D. Bjorken, Phys. Rev. **D 27** (1983), 140.
- [24] PHENIX Collaboration, PHENIX Conceptual Design Report, BNL-48922 (1993).
- [25] V.G. Riabov, Nuclear Instruments and Methods in Physics Research **A 419**(1998), 363.

- [26] Julia Velkovska, *Tracking Chambers at RHIC*, Sixteenth Int'l Conf., American Institute of Physics (2001), 227.
- [27] J. Barrette *et al.*, Nuclear Physics **A 661** (1-4) (1999), 665.
- [28] A. Lebedev, S. Bhagavatula, and M. Rosati, PHENIX Analysis Note AN (2000).
- [29] D.N. Poenaru and W. Greiner, *Experimental Techniques in Nuclear Physics* , de Gruyter, New York (1997), 87-116.
- [30] B. Nilsson-Almquist and W. Stenlund, Comput. Phys. Commun. **43** (1987), 387.
- [31] J.S. Lock, E. Bertson, J. Boissevain, D.J. Clark, W. Collier, R. Hammock, B.V. Jacak, A. Morgan, P. Roybal, S. Shaheen, J. Simon-Gillo, J.P. Sullivan, NIM **A 345** (1994), 284.
- [32] C. L. Britton, Jr., *et.al.* ,*Proceedings of the First Workshop on Electronics for LHC Experiments*, Lisbon, Portugal, (1995), 84.
- [33] W.R. Leo, *Techniques for Nuclear and Particle Physics Experiments*, Springer-Verlag, Berlin (1987).
- [34] V.C Ermilova, L.P. Kotenko and G.I. Merzon, Nucl. Instr. and Meth. **145** (1977), 555.
- [35] PHENIX Collaboration, K. Adcox *et. al.*, Phys. Rev. Lett. **86** (2001), 3500.
- [36] PHENIX Collaboration, K. Adcox *et. al.*, Phys. Rev. Lett. **87** (2001), 052301.
- [37] M. Chiu, J. Nagle, S. White, A. Franz, *et. al.* (unpublished).
- [38] S. Kelly, S. Mioduszewski, D. Morrison, J. Nagle and K. Reygers, PHENIX Analysis Note AN033 (2001).
- [39] K. Reygers, PHENIX Analysis Note AN78 (2001).

- [40] Mickey Chiu, S. Mioduszewski, D. Morrison, J. Nagle and K. Reygers, PHENIX Analysis Note AN18 (2000).
- [41] N. Bohr, Phil. Mag. **25** (1913), 10.
- [42] L.D. Landau, J. Exp. Phys. (USSR) **8** (1944), 201.
- [43] R.S. Sternheimer and R.F. Peierls, Phys. Rev. **B3** (1971), 3681.
- [44] J.E. Moyal, Phil. Mag. **46** (1955), 861.
- [45] PHOBOS Collaboration, B. Beck *et. al.*, Phys. Rev. Lett. **85** (2000), 3100.
- [46] D. Kharzeev and M. Nardi, Phys. Lett. **B 507** (2001), 121.
- [47] D. Kharzeev and E. Levin, Phys. Lett. **B 523** (2001), 79.
- [48] D. Kharzeev, E. Levin and M. Nardi, hep-ph/0111315 (2001).
- [49] D. Kharzeev, hep-ph/0204014 (2001).
- [50] X.-N. Wang and M. Gyulassy, nucl-th/0008014.
- [51] K. Adcox et al., Phys. Rev. **C66**, 024901 (2002). *Proceedings of Quark Matter 1987*, edited by H. Satz, H.J. Specht and R. Stock.
- [52] PHENIX Collaboration, K. Adcox *et. al.*, Phys. Rev. Lett. **88**, 242301 (2002).
- [53] F. Abe *et. al.*, Phys. Rev. **D 41** (1990), 2330.
- [54] L.V. Gribov, E.M. Levin and M.G. Ryskin, Phys. Rept. **100** (1983), 1.
- [55] L. McLerran and R. Venugopalan, Phys. Rev. **D 49** (1994) 2233; 3352; **D 50** (1994) 2225; **D 59** (1999) 094002; Yu.V. Kovchegov, Phys. Rev. **D 54** (1996) 5463; **D60** (1999) 034008; Yu. V. Kovchegov and D.H. Rischke, Phys. Rev. **C56** (1997) 1084; M. Gyulassy and L. McLerran, Phys. Rev. **C56** (1997) 2219; J.

- Jalilian-Marian, A. Kovner, L. McLerran, H. Weigert, Phys.Rev. **D55** (1997) 5414; E. Iancu, A. Leonidov and L. McLerran, hep-ph/0011241.
- [56] A.H. Mueller, Nucl.Phys. **B 572** (2000) 227.
- [57] A.D. Martin, R.G. Roberts, W.J. Stirling, R.S. Thorne, hep-ph/0007099.
- [58] A. Krasnitz and R. Venugopalan, hep-ph/0007108.
- [59] Yu.V. Kovchegov, hep-ph/0011252.
- [60] Yu.L. Dokshitzer, *Sov. Phys. JETP* **46** (1977) 641; V.N. Gribov and L.N. Lipatov, *Sov. J. Nucl. Phys.* **15** (1972) 438; L.N. Lipatov, *Yad. Fiz.* **20** (1974) 181.
- [61] G. Altarelli and G. Parisi, *Nucl. Phys.* **B126** (1977) 298.
- [62] Gyulassy, M. and McLerran, L., Phys. Rev. **C56** (1997), 2219.
- [63] K. Golec-Biernat and M. Wüsthof, Phys. Rev. **D59** (1999) 014017;

# Appendix A

## Ntuple Production from PRDF

Although it has been described earlier, we show the complex chain from the interaction of gold-gold collision to the output results production chain in Fig. A.1.

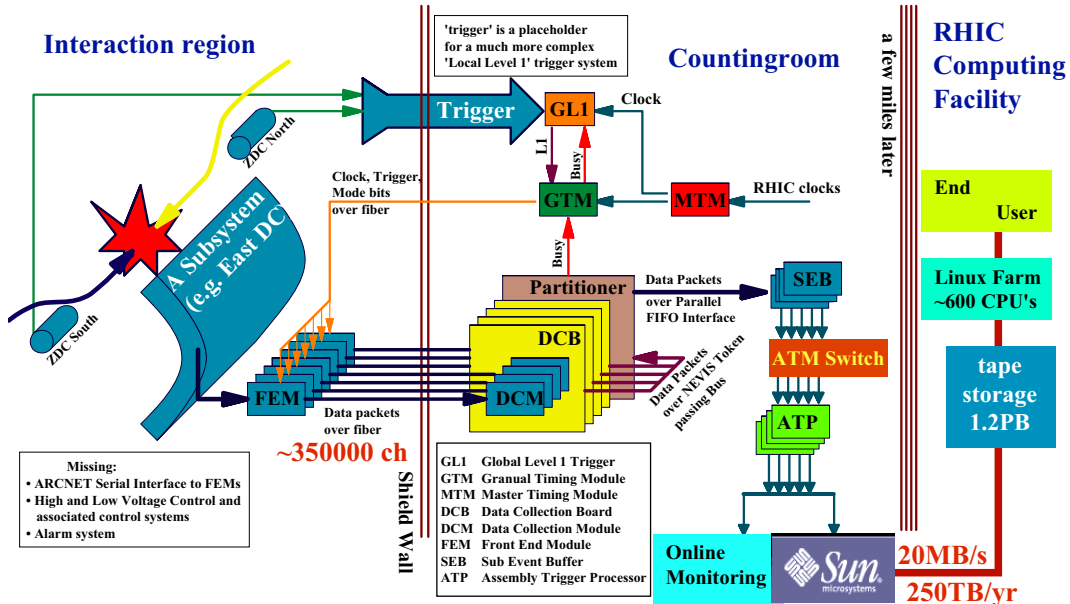


Figure A.1: PHENIX Data Production & Analysis Chain

Once the collision has occurred and the ZDC and BBC coincidence flags the data to be “good” (that mean they say that a collision has been occurred), the data from the DCM output which are called **Phenix Raw Data Format** or **PRDF** is produced

and is transferred to the RHIC Computing Facility and stored in RCF tape. Then the PHENIX Offline farm, using the standard PHENIX reconstruction chain, produces **Data Summary Tape** or DST files. Once the DSTs are produced the end user used them for analysis.

As it has been mentioned earlier that MVD could participate only for two runs in the PHENIX data taking procedure. And also only a fraction of the MVD took part in the production, MVD was not included in the official Reconstruction chain. Therefore we had to make our own library and write the reconstruction code for MVD and run the reconstruction for the PRDFs privately to produce Ntuples. Since vertex measurement could not be done with MVD for very limited electronics installation, we needed the vertex measured from the BBC. Also we needed ZDC, together with BBC, for the centrality measurement. But except from MVD all subsystem was included in the PHENIX reconstruction chain. So we could correlate MVD ntuples to the official PHENIX ntuples and get all the necessary information.

We wanted to look at the multiplicity distribution of individual strips. There were 512 strips in the “good” MVD region. To make ntuples from PRDFs we booked the following quantities:

1. Event number : This is a global pointer. This enables us to relate MVD ntuples and PHENIX dst.
2. Packet ID : This is a unique number corresponds to data from each MCM. The 512 good strips correspond to packetid=2019 and packetid=2020.
3. stripnumber.
4. ADC of each strips.
5. AMU cell number

And PHENIX DST contains, among many quantities, the followings:

1. Event number.
2.  $bbc_{cz}$  : vertex position measured by BBC.
3.  $zdc_{cz}$  : vertex position measured by ZDC.
4.  $bbc_{q0}$ ,  $bbc_{q1}$  : charges in the north and south BBC
5.  $zdc_{e0}$ ,  $zdc_{e1}$  : energies in the north and south BBC

We then combined the two ntuples to generate the ntuple we need for our analysis.

Here is the chart in Fig. 4.11 on how we combine the two ntuples.

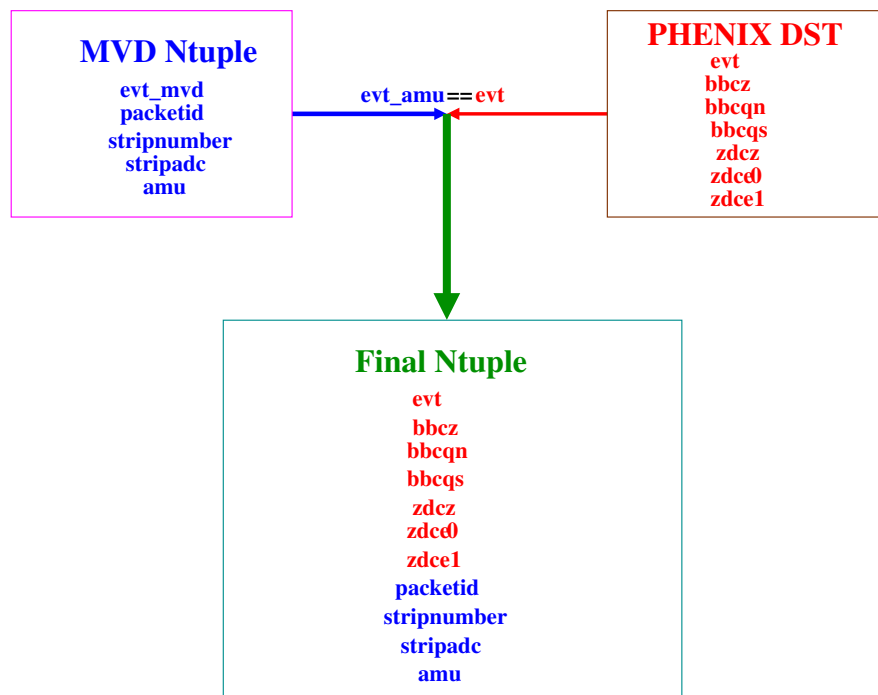


Figure A.2: Flowchart for the Ntuple production for Analysis